STUDY OF MULTI-SCALE TRANSPORT PHENOMENA IN TIGHT GAS AND SHALE GAS RESERVOIR SYSTEMS

A Dissertation

by

CRAIG MATTHEW FREEMAN

Submitted to the Office of Graduate and Professional Studies of
Texas A&M University
in partial fulfillment of the requirements for the degree of

DOCTOR OF PHILOSOPHY

Chair of Committee,	Thomas A. Blasingame
Co-Chair of Committee,	George J. Moridis
Committee Members,	Eduardo Gildin
	Simon North
Head of Department,	Dan Hill

December 2013

Major Subject: Petroleum Engineering

ABSTRACT

The hydrocarbon resources found in shale reservoirs have become an important energy source in recent years. Unconventional geological and engineering features of shale systems pose challenges to the characterization of these systems. These challenges have impeded efficient economic development of shale resources. New fundamental insights and tools are needed to improve the state of shale gas development.

Few attempts have been made to model the compositional behavior of fluids in shale gas reservoirs. The transport and storage of reservoir fluids in shale is controlled by multiple distinct micro-scale physical phenomena. These phenomena include preferential Knudsen diffusion, differential desorption, and capillary critical effects. Together, these phenomena cause significant changes in fluid composition in the subsurface and a measureable change in the composition of the produced gas over time.

In order to quantify this compositional change we developed a numerical model describing the coupled processes of desorption, diffusion, and phase behavior in heterogeneous ultra-tight rocks as a function of pore size. The model captures the various configurations of fractures induced by shale gas fracture stimulation. Through modeling of the physics at the macro-scale (e.g. reservoir-scale hydraulic fractures) and micro-scale (e.g. Knudsen diffusion in kerogen nanopores), we illustrate how and why gas composition changes spatially and temporally during production.

We compare the results of our numerical model against measured composition data obtained at regular intervals from shale gas wells. We utilize the characteristic behaviors explicated by the model results to identify features in the measured data. We present a basis for a new method of production data analysis incorporating gas composition measurements in order to develop a more complete diagnostic process.

Distinct fluctuations in the flowing gas composition are shown to uniquely identify the onset of fracture interference in horizontal wells with multiple transverse hydraulic fractures. The timescale and durations of the transitional flow regimes in shales are quantified using these measured composition data. These assessments appear to be robust even for high levels of noise in the rate and pressure data. Integration of the compositional shift analysis of this work with modern production analysis is used to infer reservoir properties.

This work extends the current understanding of flow behavior and well performance for shale gas systems to encompass the physical phenomena leading to compositional change. This new understanding may be used to aid well performance analysis, optimize fracture and completion design, and improve the accuracy of reserves estimates.

In this work we contribute a numerical model which captures multicomponent desorption, diffusion, and phase behavior in ultra-tight rocks. We also describe a workflow for incorporating measured gas composition data into modern production analysis.

DEDICATION

This thesis is dedicated to my family and friends for their help and support.

If you are equally good at explaining any outcome, you have zero knowledge.
— Eliezer Yudkowsky

It's a problem; it gets solved.
— Jeanine Pettibone, This is Spinal Tap

Decay is inherent in all compound things. Work out your salvation with diligence.
— Last words of the Buddha

ACKNOWLEDGEMENTS

The author would like to thank the following for their contributions to this work: Dr. George. J. Moridis, co-chair of my advisory committee, for challenging me to greater heights and teaching me the skills I needed to achieve them; Dr. Thomas A. Blasingame, co-chair of my advisory committee, for his support and mentorship, leading me by example to a higher standard; Dr. Eduardo Gildin, for serving on my advisory committee and for his insightful and thorough tutelage; Dr. Simon North, for serving on my advisory committee, and for precipitating more than his share of epiphanies; Eric Michael and ConocoPhillips for providing me the opportunities which expanded the scope of this research; Noel Keen and Jeff Johnson for their help with the finer points of computer science needed along the way; Dilhan Ilk for his guidance and advice in performing the research; and Femi Olorode for his collaboration on the MeshVoro code development.

I am indebted to my family and my friends for their patience with me and for their contributions to my personal growth throughout my years in College Station, TX. Particularly: My parents Den and Mary Freeman and my brother Daniel Freeman for their continuous influence and support throughout my life; Dr. Michael Grubb for his inspiring friendship and challenging discussions, without whose influence I would be an entirely different and lesser person; Katie Freeman for her support, encouragement, and influence as colleague and wife; Cassandra Oeth for her friendship and camaraderie; and Jean Freeman for giving me a good reason.

TABLE OF CONTENTS

Page

LIST OF FIGURES

FIGURE Page

LIST OF TABLES

TABLE Page

CHAPTER I
INTRODUCTION

1.1 Statement of the Problem

Unconventional hydrocarbon resources such as natural gas from shale and tight sandstone reservoirs stand to dominate the energy landscape in the coming century (Hill and Nelson 2000). Efficient and effective development of energy resources relies on a solid engineering understanding of the physical properties of the system in question. Accurate and comprehensive reservoir characterization of tight/shale gas systems continues to elude engineers. Without such an understanding, the engineering and economic uncertainties surrounding tight/shale gas resources inhibit efficient resource development (Clarkson et al. 2011).

The aim of this work is to devise a methodology by which an engineer might use flowing gas composition data to improve tight/shale gas reservoir characterization. The development of such a methodology requires an integration of geological, chemical and petroleum engineering concepts. The core contribution of this work is a numerical model incorporating all of the physics relevant to the problem of compositional change in shale. The model will then be validated against core analyses and experiments, and surface flowing gas composition data. Finally the numerical model will be used to generate a model-based analysis technique with the aim of reducing uncertainty in reservoir characteristics.

1.2 Objectives

The objectives of this work are:

- To *create* robust, efficient and flexible simulation meshes for flow through complexly fractured low permeability media.
- To *develop* a numerical reservoir simulator capable of capturing the physical mechanisms in tight/shale gas systems leading to compositional change.
- To *validate* the correctness of the numerical model by comparing its results against the results measured flowing composition data.
- To *analyze* the flow behavior exhibited by wells using the numerical model, and to thereby…
- … *characterize the effects* of various completion and reservoir properties on compositional flow behavior at the wellhead.

1.3 Organization of the Dissertation

The outline of the research dissertation is as follows:

- Chapter I — Introduction
  - — Introduction
  - — Objectives
  - — Statement of Problem

- Chapter II — Literature Review
  - Geology of Shale Gas Systems
  - Shale Gas Well Completion Practices
  - Storage Mechanisms in Shale Gas Systems
  - Transport Mechanisms in Shale Gas Systems
- Chapter III — Numerical Model Development
  - Flow Models
  - Storage Models
  - Special Considerations for Shale Liquids
  - Meshes for Fractured Shale Systems
- Chapter IV — Compositional Change in Shale Gas Wells
  - Simulation Study Description
  - Simulation Results
  - Field Data Diagnostics
- Nomenclature
- References
- Appendices
  - Validation
- Vita

CHAPTER II
LITERATURE REVIEW

In order to correctly model the shale gas reservoir system, we must ensure that we have captured the relevant physics regarding how fluids are stored within and transported through the various geological units of shale gas systems. We first describe the current understanding of shale gas systems from a geological standpoint, including the tools currently available for quantitative and qualitative analysis of these systems. Then we describe in detail the physics underlying storage in shale, including adsorption and capillary effects. We go on to describe the physics of transport through shale, including the various modes of diffusion.

2.1 Shale Gas Geology

Shale gas systems are composed primarily of shale with lesser amounts of other fine grained rocks. In recent years, the moniker "shale gas" has been applied to plays which are not technically shale, e.g. the Horn River Basin and Hayesville Shale which possess very low organic matter content, and the Barnett Shale, much of which is technically mudstone (Bustin et al. 2008). Shale gas reservoirs are often the source of the natural gas as well as the reservoir (Frantz and Jochen 2007). The high content of organic matter in typical shales (highest in so-called "black shales") permits the generation of natural gas (Passey et al. 2010). Shale, being very fine-grained and possessing pore throat dimensions on the order of nanometers, typically has very low permeability. Therefore, most shale deposits are not economically producible reservoirs of natural gas. Shale reservoirs with natural fractures may possess sufficient connectivity to permit economic flowrates. Also, the modern process of artificially hydraulically fracturing shale gas wells creates a highly conductive pathway for transport of natural gas from deep within the shale formation to the wellbore (Faraj et al. 2004).

Only 20% of the original gas in place is typically recovered from shale gas reservoirs. Compare this against a 75% recovery for conventional reservoirs (Powers 2005).

2.1.1 Shale Gas Viability

Shale gas reservoirs are composed of fine grained sediment and self-sourcing, in the sense that the hydrocarbon charge originates from the organic content within the shale. In general for petroleum systems, hydrocarbons generated from thermal maturation of kerogen induces microfracturing in the shale matrix, providing migration pathways through the system and out to the reservoir. The shale becomes a viable shale gas reservoir when the generated gas does escape from where it is generated. (Forgotson 2006).

The key parameters controlling the viability of shale gas production from a given formation are the generative potential for hydrocarbons, and the presence of adequate porosity and permeability to permit

storage and transport of the gas. The presence of fractures, whether artificially induced or natural, is another key feature of a shale gas reservoir. The low permeability of shale matrix permits very low flow rates, unless an extensive network of fractures exists throughout the matrix, providing a secondary flow system (Nelson 2001).

Shale gas reservoirs possess very low permeability and relatively low porosity, so thicker, flatter and more homogeneous shale sequences are more favorable. In such systems, individual wells may produce for several decades (Frantz and Jochen 2007).

2.1.2 Reservoir Characterization

In order to ensure that a correct and consistent model of the reservoir is generated, all available production, geophysical and geological data is integrated via the process of reservoir characterization. A variety of tools have evolved recently to better enable characterization of shale gas reservoirs. New core analysis techniques such as porosimetry studies and adsorption experiments have been developed, and novel production analysis techniques have been invented for specific application to shale gas systems (Zahid et al. 2007). Special well log analyses have been developed to characterize the proportion of free and adsorbed gas, the matrix clay content, the mechanical properties of the shale, to aid in identification of natural and drilling induced fractures, and to measure formation pressures and fracture gradients (Bartenhagen 2007).

The purpose of this work is to contribute a new tool to be incorporated in the process of reservoir characterization.

2.2 Reservoir Fluid Storage Mechanisms

In order and model the behavior of fluids in shale, we must first understand the ways in which fluids physically interact with the shale matrix. In all attempts to model flow through porous media, consideration is first given to the governing behavior of the fluid by itself, and then further assumptions are made in order to take into account the interaction of the fluid with the porous medium. First we discuss the molecular behavior of petroleum fluids. Then we discuss the manner in which these fluids interact with the shale.

2.2.1 Behavior of Fluids

An early conceptualization of gas behavior was the ideal gas model. This model treats the molecules of a gas as spheres of infinitesimal size which do not interact with each other and which undergo perfectly elastic collisions with the walls of any container.

$$pV = nRT \quad \text{.....(2.1)}$$

The ideal gas law gives reasonably accurate predictions at low pressures for small molecules. At higher pressures, the non-idealities of real gases come into play. First, gas molecules exhibit mutual electrostatic

interactions, which may be attractive or repulsive. A common expression used to approximate the electrostatic potential between gas molecules is the Lennard-Jones model,

$$V_{LJ} = 4\varepsilon\left[\left(\frac{\sigma}{r}\right)^{12} - \left(\frac{\sigma}{r}\right)^{6}\right] \quad \text{.....(2.2)}$$

The Lennard-Jones model is widely used because it is computationally compact and gives a relatively good fit to the actual system behavior (Steinfeld et al. 1998). Gas molecules will likewise have an electrostatic potential with respect to the surface of their container. At high pressures, gas molecules spend more time in close proximity to one another, and thus the density of the gas phase is influenced by the electrostatic potential which exists between the gas molecules (Ambrose et al. 2011).

When gas molecules possess a complex internal structure, such as hydrocarbon molecules, the total energy of a given molecule is distributed over its internal degrees of freedom. A nonlinear molecule possess 3N-6 possible internal vibrational modes. For example, a propane molecule contains three carbon atoms and eight hydrogen atoms, so it will exhibit 27 internal vibrations. The energy of a gas is distributed across the internal rotational, vibrational and electronic modes of the molecules and the translational motion of the molecules, leading to a Maxwell-Boltzmann distribution of velocities (Steinfeld et al. 1998).

The consequence of these complex interactions between gas molecules is a deviation from ideal behavior. The deviation is typically accommodated by the compressibility factor Z in the real gas law,

$$pV = ZnRT \quad \text{.....(2.3)}$$

The compressibility factor is computed using an equation of state, such as the Peng-Robinson (Peng and Robinson 1976) equation of state. Typically an equation of state incorporates information about the gas molecules and their proportions in the gas phase to arrive at an approximate compressibility factor.

2.2.2 Interactions with the Porous Medium

In conventional oil and gas reservoirs, essentially all of the petroleum fluids are stored within the pore space of the rock as gas, liquid, or a supercritical phase. Straightforward application of tuned equations of state is typically sufficient to accurately compute the thermophysical properties of the petroleum fluids as a function of temperature and pressure (McCain 1990).

In contrast, fluids in shale gas reservoirs interact much more significantly with the walls of the porous medium (Leahy-Dios et al. 2011). There are two reasons for this. First, the kerogen in shale possesses a high chemical affinity for hydrocarbon fluids, meaning it is “oil-wet,” and provides active sites for adsorption (Ambrose et al. 2011). Second, the pores in kerogen are on the order of nanometers in size, which creates a surface area orders of magnitude higher than the surface area of, for example, a piece of sandstone with the same volume and porosity (Passey et al. 2010; Fathi and Akkutlu 2011).

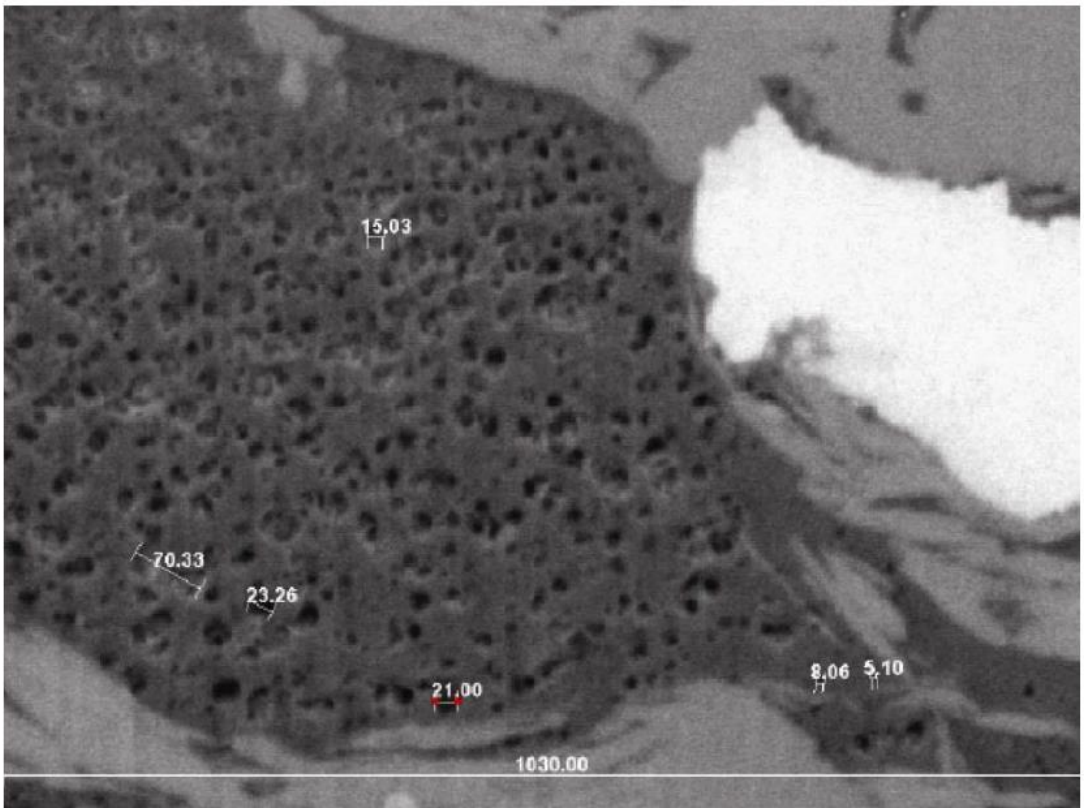

Figure 2.1 — Backscatter SEM image of porous kerogen in the Barnett shale, demonstrating the concentration of porosity in the soft kerogen. Pore throat dimensions are in nanometers and the image itself is 1030 nanometers across. Adapted from Sondergeld et al. (2010).

In general, for pores with diameter less than 0.01 μm, the sorptive storage exceeds the compressed gas storage (Bustin et al. 2008). Additionally, the clay associated with shales and mudrocks also contains its own microporosity. Illite, kaolinite and some montmorillonite possess a significant fraction of pores of effective radius less than 2 nm (Bustin et al. 2008). Scanning electron microscopic images of these nanometer-scale pores can be observed in Figure 2.1.

A substantial fraction of the hydrocarbon-bearing pore volume in tight gas and shale gas reservoirs exists in pores of very small diameter. Tight gas sands may exhibit pore throats with diameters on the order of micrometers. Shale, and particularly the kerogen content of shale, is largely composed of pores with diameters of a few nanometers (Javadpour et al. 2007). This ubiquity of very small pores leads to various physical consequences with regards to transport and storage of fluids.

2.2.2.1 Surface Adsorption

A substantial fraction of the gas stored in shale is adsorbed to the surface of the shale (Fathi and Akkutlu 2011). The theory of physical adsorption in porous media has been applied to many different fields. One

area of application of adsorption theory lies with the industrial use of synthetic clay zeolite minerals for gas separation (Xiao and Wei 1990). Another area of application is gas production from within coal deposits, known as coalbed methane. Coal and zeolite minerals are both substances with high surface area and significant electrochemical affinity for binding nonpolar gas molecules (Clarkson and Bustin 1999).

The classical view of Langmuir (1916) adsorption is as follows: The gas phase exists in equilibrium with the single layer of molecules which is adsorbed to the surface. Individual gas molecules collide with each other and with the sorptive surface, exchanging energy with every collision. The energy of a gas molecule is distributed over its kinetic energy and its internal degrees of freedom, e.g. its vibrational, rotational, and electronic energy states. Because of the constant collisions between molecules and subsequent internal redistributions of the collisional energy, there will be a statistical distribution of velocities found within a gas. In other words, in a statistical ensemble of gas molecules, some molecules will have lower velocities. The sorptive surface is viewed as having irregularities and imperfections. These imperfections serve as potential energy wells in which lower-velocity gas molecules may be trapped when these molecules collide with the surface. A surface with strong affinity for the carrier gas, with ample imperfections providing adsorption sites, may host a large fraction of gas molecules trapped in these adsorption sites (Steinfeld et al. 1998).

This basic understanding of sorption kinetics helps in understanding the more sophisticated realities of sorption in kerogen. The surface of kerogen is so irregular that sorption sites are plentiful. The pressures and densities of the natural gas in shale reservoirs are so high that sorption-like phenomena may occur almost anywhere on the surface (Akkutlu and Fathi 2011).

One of the assumptions of Langmuir adsorption is that the maximum possible thickness of the adsorbed layer is one molecule of thickness, i.e. a monolayer. However, in shales, the adsorbed layer may be two or more gas molecules thick (Ambrose et al. 2011). This suggests a view of the adsorbed layer as being similar to a condensed film. The distinction between adsorption and capillary condensation becomes somewhat *ad hoc* when pore diameters are this small. It may be helpful to think of sorption in shales as *facilitated condensation* rather than classical Langmuir adsorption (Passey et al. 2010). Many authors (Bustin et al. 2008; Brunauer et al. 1938) have proposed mathematical models for adsorption with various assumptions, including multiple adsorbed layers and sophisticated intermolecular interactions involving orientational and electrostatic factors.

Because multiple adsorbed layers exist in kerogen adsorption, Langmuir adsorption theory probably does not accurately describe the process of adsorption in kerogen. However, gas desorption from kerogen has been studied in context of coalbed methane reservoirs, where adsorption can be the primary mode of gas storage. The study of gas desorption from coalbed methane reservoirs has led to the development of many semi-analytic and analytic models, including models describing transient responses and multicomponent

interactions (Clarkson and Bustin 1999). However, the sorptive properties of shale are not analogous to those of coal (Schettler and Parmely 1991). The Langmuir model was based on the theory described above. In its application to desorption in shales and coal, it has been treated as semi-empirically, where the two values of the parameters are fit to measured data. The Langmuir (1916) isotherm is given by:

$$G = \frac{pV_L}{p + p_L} \quad \text{.....(2.4)}$$

The desorption isotherms as proposed by Langmuir contain the V_L term which expresses the total storage at infinite pressure, and the p_L term representing the pressure at which half of this volume is stored. Further, the Langmuir model assumes instantaneous equilibrium of the sorptive surface and the storage in the pore space. From a modeling perspective, this means there is no transient lag between pressure drop and desorption response. Due to the low permeability of shales, flow through the sorptive media is sufficiently slow that instantaneous equilibrium is a good assumption (Gao et al. 1994).

The Extended Langmuir model has served as an extended empirical means of modeling multicomponent sorption:

$$G_i = \frac{V_{L,i} b_i p y_i}{1 + \sum_j b_j p y_j} \quad \text{.....(2.5)}$$

Another popular model for adsorption is the Brunauer, Emmett, and Teller (BET) equation (Brunauer et al. 1938) is derived along the same theoretical lines as the Langmuir equation, but permits an arbitrary number of adsorbed layers to form.

$$\frac{\frac{p}{p_0}}{v\left(1 - \frac{p}{p_0}\right)} = \frac{1}{v_{mon} K} + \frac{\frac{p}{p_0}\left(c - \frac{p}{p_0}\right)}{v_{mon} K} \quad \text{.....(2.6)}$$

The Ideal Adsorbed Solution (IAS) sorption model (Myers and Prausnitz 1963) treats the adsorbed phase as an ideal solution, similar to Raoult's law. The IAS model is more accurate than the extended Langmuir model at predicting the multicomponent adsorption behavior of a gas mixture. However, the IAS relies on accurate Gibbs adsorption isotherms for the individual components, which are very rarely measured.

The optimal sorption model would be capable of *a priori* prediction of multicomponent sorption isotherms for a gas given information about the mineralogy of the porous medium and the gas composition and thermodynamic starting conditions. If such a model existed, it would be possible to precisely predict the contribution and composition of desorbed gas in the total produced gas. However, no such model exists at this time. We are instead limited to sorption models which rely on empirically fit parameters, such as the above models.

There are several weaknesses inherent in application of the above models. First, different core analysis laboratories may report significantly different sorption isotherm parameters for the same sample, even when adhering to the same experimental standards (Clarkson et al. 2011). This implies that the experimentally determined sorption isotherm parameters are not reliable. Secondly, core obtained from shale gas reservoirs is typically damaged in unpredictable ways by the process of retrieval, and core experiments are not always performed at reservoir conditions of stress, temperature and pressure. Additionally, the *in situ* composition of the reservoir fluid is never precisely known due to leakage during sample retrieval, and due to the practice of venting cores to a safe pressure at the surface (Clarkson et al. 2011).

2.2.2.2 Capillary Effects

When fluid molecules diffuse into sufficiently small pores or capillaries, the movement of the molecules becomes restricted. Fluids which would form a gaseous phase at bulk conditions will instead behave more like a liquid. This phenomenon is known as capillary condensation (Tovbin et al. 2005).

In general, the existence of constraining pores or capillaries has an effect on the thermophysical properties of the fluid. One mechanism which has been investigated thoroughly is critical point depression. The influence of the capillary walls pushes the bulk critical point of the fluid to an effective "capillary critical point." The consequence of this effect is that the two-phase region of the phase diagram for a given fluid shrinks to lower temperatures. Fluids in small pores are generally more prone to remain in the single-phase region of the phase envelope, either as a liquid, gas, or supercritical phase (Evans et al. 1986).

$$\frac{\left(T_c - T_{cc}\right)}{T_c} \leq \frac{d}{R_c} \quad \text{.....(2.7)}$$

The capillary effect most generally known in petroleum engineering is that of capillary pressure. Geological porous media generally possess chemical affinity either for oil or water (i.e. nonpolar or polar substances) and usually contain some amount of both an oil and water phase. Surfaces with affinity for oil are said to be "oil-wet" while surfaces with affinity for water are said to be "water-wet." If a surface is oil-wet, then oil is the "wetting phase" and water is the "non-wetting phase." The porous medium will influence the surface tension existing between the wetting phase and the non-wetting phase (Dake 1978). This distortion of the phase interface energy can be recast as an effective suction pressure on the wetting phase, the "capillary pressure."

A secondary consequence related to capillary pressure is that of relative permeability. Under a pressure gradient, according to Darcy's law, the flow velocity of a fluid should be a function of the fluid's viscosity and the matrix permeability. However, when both wetting and non-wetting phases are flowing through the same medium, the relative affinities of the fluids for the porous medium must be taken into account (Dake 1978).

Note the capillary pressure is distinct from capillary condensation and other capillary critical effects. Capillary pressure refers to an effective pressure discontinuity between a liquid and gaseous phase. At the scale of capillary condensation, a gas-liquid interface is not distinct. In shale micropores, capillary critical effects will be dominant. In the larger interstitial pores and microcracks of shale, capillary pressure may be more significant.

2.2.3 Phase Change

Three phases are generally present in shale gas reservoirs: gas, liquid water, and liquid hydrocarbon (Passey et al. 2010). Even relatively "dry" reservoirs such as the Barnett Shale, of which the produced gas may be composed of greater than 90% methane, contain a higher fraction of heavier hydrocarbon compounds *in situ*. However, these heavier compounds are left behind in the reservoir as the methane depletes, due to the various modes of compositional change discussed here, primarily selective desorption of lighter compounds (Passey et al. 2010).

In the previous section we discuss how fluids in very small pores will tend behave as a single phase regardless of what bulk properties the fluid might be expected exhibit. However, even within shale, not all of the reservoir fluid will exist in these small pores. Some quantity of the reservoir fluid will be present in sufficiently large pores that phase segregation can occur (Javadpour et al. 2007; Passey et al. 2010). Where a phase interface is present, thermodynamic and kinetic equilibration between the fluid phases will occur. In these cases, the composition of the liquid and vapor phases will change as pressure declines. Because the vapor phase is more mobile, the lighter components will flow out of the pore more readily. Consequently, phase change accompanying pressure decline leads to compositional change in the flowing gas phase (McCain 1990).

Equations of state and equilibrium constants are typically used to characterize the compositional equilibrium of phases during phase change.

2.3 Transport of Fluids in Shale

Transport of fluids through conventional subsurface reservoirs typically occurs via convection, which is flow in response to a pressure gradient. The constitutive equation for this type of flow is Darcy's law (Dake 1978).

$$v = \frac{k}{\mu} \nabla p \quad \text{.....(2.8)}$$

Transport of fluids through shale occurs in pores possessing a range of pore sizes and pore throat diameters. Some of the kerogen pores may be below one nanometer in diameter, while some microcracks may be micrometers in width, and macroscale fractures will also exist (Javadpour et al. 2007). Different transport mechanisms will be dominant at different length scales. The potential transport modes in shale are

- Convection
- Knudsen diffusion
- Ordinary diffusion
- Surface diffusion
- Configurational diffusion
- Liquid diffusion

2.3.1 Convective Flow

Convection dominates net fluid flux in large pores. The regime of convective flow occurring in porous media is typically Darcy flow, which is within the Reynolds regime of laminar flow. This implies that the continuum assumption of fluid mechanics is valid, and that viscous forces dominate over inertial forces within this continuum (Bird et al. 2002).

The fundamental assumption of continuum mechanics is that the behavior of the individual atoms and molecules which make up a fluid can be aggregated into a continuum, such that the fluid properties no longer explicitly reflect the discrete (molecular) nature of matter (Slattery 1999).

2.3.2 Knudsen Diffusion

According to the ideal gas assumption, the molecules of a gas are infinitesimally small and undergo perfectly elastic collisions with the walls of their container. In reality gas molecules are not infinitesimal and will undergo collisions with other gas molecules. Gas molecules will also experience electrostatic attraction and repulsion to other gas molecules, which will influence the molecules' trajectories. The mean free path for a gas is the average distance that a molecule of that gas will travel before colliding with another gas molecule (Steinfeld et al. 1998).

For Knudsen numbers less than 0.01 in a porous medium, the continuum assumption of fluid mechanics remains valid and Darcy's law applies without adjustment. As the Knudsen numbers grows greater than 0.01, the interactions of the gas molecules with the pore walls become more and more significant. A Knudsen number greater than 10 indicates fully developed Knudsen flow, or *free molecular flow*. In free molecular flow, the dynamics of the gas resembles discrete objects bouncing through tubes and only rarely interacting with one another (Javadpour et al. 2007).

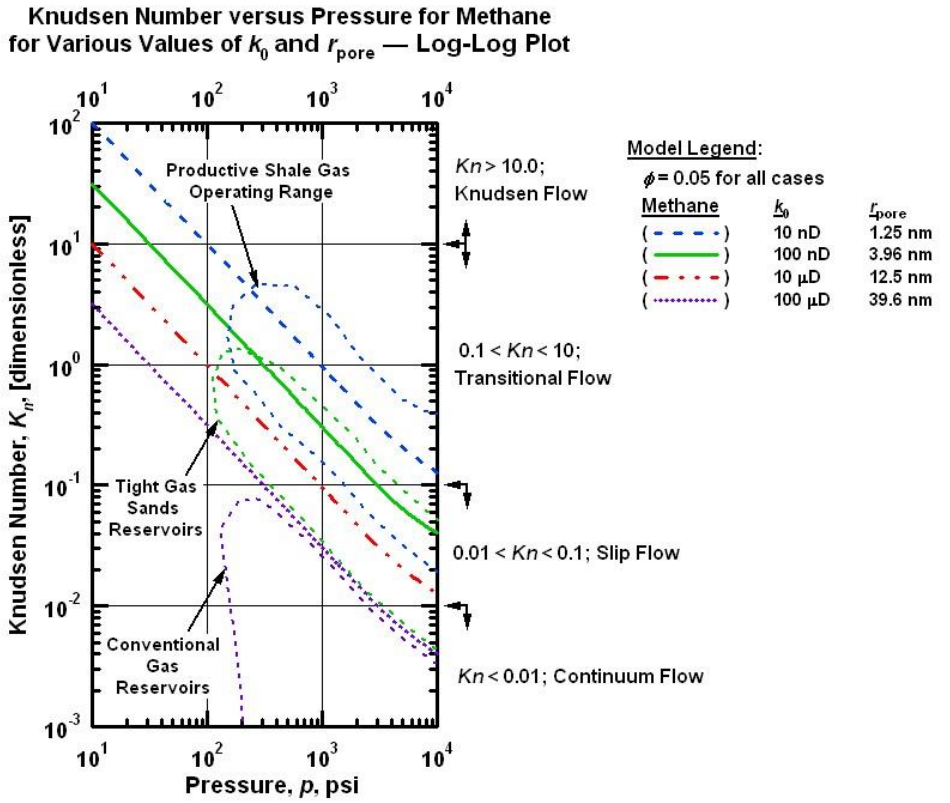

Figure 2.2 — Regimes of Knudsen flow, flow domain of methane with respect to pressure in various reservoir types (Freeman et al. 2011).

The Knudsen number is the ratio of the mean free path to the equivalent hydraulic radius of the pores in the porous medium,

$$Kn = \frac{\lambda}{r_p} \quad \text{.....(2.9)}$$

The region situated between Knudsen numbers 0.01 and 10, as depicted in Fig. 2.2, is known as the slip or transitional region. Flow within this region can sometimes be correctly modeled using minor corrections to Darcy's law. Within petroleum engineering literature, the term Klinkenberg flow is used to refer to the slip flow regime. The Klinkenberg correction (Klinkenberg 1941) arrives at a single empirical parameter which characterizes the deviation from Darcy permeability as a function of pressure.

A more theoretical, less phenomenological approach to modeling Knudsen diffusion is to use the Knudsen diffusivity parameter (Civan 2008),

$$D_i^K = \frac{4k}{r_p}\sqrt{\frac{\pi RT}{2M_i^w}} \quad \text{.....(2.10)}$$

There have been multiple proposed methods for deriving the Knudsen diffusivity from a variety of starting points. For example, it is also possible to express the Knudsen diffusivity in terms of the Klinkenberg constant (Civan 2008),

$$D_i^K = \frac{kb_i}{\mu_i} \quad \text{.....(2.11)}$$

If the Knudsen diffusion coefficient for one component is known, the coefficient for each other species can be inferred using the relative molecular weights (Webb et al. 2003):

$$D_j^K = D_i^K \left(\frac{m_i}{m_j} \right)^{1/2} \quad \text{.....(2.12)}$$

Webb (2001) assumes that measured Knudsen diffusion coefficients are provided at 25° C, on the basis that the Heid et al. (1950) correlation assumes this. Therefore, the Knudsen diffusion coefficients must be corrected to the temperature of the system by

$$D_{i,T}^K = D_i^K \left(\frac{T + 273.15}{298.15} \right)^{1/2} \quad \text{.....(2.13)}$$

Knudsen diffusion coefficients are measured using porous media of interest, so modifying the coefficient to account for the tortuosity of the porous media is redundant; the Knudsen diffusion coefficient already reflects the tortuosity. However, saturation-dependent tortuosity may still be significant:

$$D_i^{K*} = D_{i,T}^K \tau_\beta \quad \text{.....(2.14)}$$

Accounting for Knudsen diffusion by itself will yield correct fluxes only for a single-component gas. For multiple gas species, the situation found in all natural gas reservoirs, ordinary diffusion must also be taken into account.

2.3.3 Ordinary Diffusion

Diffusion is the random thermal motion of fluid particles. Diffusion occurs constantly in all liquids and gases. Where the concentration of a molecular species is not in spatial equilibrium, this thermal diffusion will cause the concentration to equilibrate over time. Once a fluid is at thermodynamic equilibrium, random motion of the fluid molecules continues, but does not result in any statistically significant spatial fluctuation in composition (Bird et al. 2002).

Shale gas reservoirs in pristine condition are at thermodynamic equilibrium. As soon as downhole operations begin, pressure and composition gradients are introduced. First, drilling fluid and stimulation fluids are injected, and then reservoir fluids are produced. The concentration gradient of a species within the fluid determines the diffusion rate of the species, according to Fick's law (Bird et al. 2002),

$$J_i = D_i \nabla x_i \quad \text{.....(2.15)}$$

In a bulk fluid, diffusion is considered relative to the fluid, not relative to stationary coordinates. Consider the diffusion of a droplet entrained in a bulk laminar flow inside a pipe. The absolute velocity of the

droplet is equal to the flow velocity of the bulk fluid, but the relative flow velocity describing diffusion of the droplet into the bulk phase is slow.

At low pressures, the binary diffusion coefficient or diffusivity coefficient for two species *a* and *b* can be estimated by

$$D_{ab}^{LoP} = \frac{1.43\times10^{-7}\left(T^{1.75}\right)}{1.0\times10^{-5}\,p\left(\dfrac{2}{1/MW_a + 1/MW_b}\right)^{1/2}\left(D_{V,a}^{1/3} + D_{V,b}^{1/3}\right)^2} \quad \text{.....(2.16)}$$

where D_V represents the diffusion volume (Fuller et al. 1969). Note that in this expression the diffusion coefficient does not depend on the composition of the species. At high gas pressure, the diffusion coefficient is dependent on gas composition due to the relative increase in intermolecular interactions, and can be estimated by the method of Riazi and Whitson (1993) which modifies the low-pressure diffusion coefficient with an extra term accounting for nonidealities,

$$D_{ab}^{HiP} = \left(1.07\left(\frac{\rho_L}{\rho_H}\right)\left(\frac{\mu_H}{\mu_L}\right)^{\left(b_R + c_R\frac{p}{\bar{p}_c}\right)}\right) D_{ab}^{LoP} \quad \text{.....(2.17)}$$

where

$$\omega_c = y_a\omega_a + y_b\omega_b \quad \text{.....(2.18)}$$

$$\bar{p}_c = y_a p_{c,a} + y_b p_{c,b} \quad \text{.....(2.19)}$$

$$c_R = -0.05 + 0.1\omega_c \quad \text{.....(2.20)}$$

and

$$b_R = -0.27 + 0.38\omega_c \quad \text{.....(2.21)}$$

In the method of Riazi and Whitson (1993) the low-pressure density and viscosity are taken at a reference point (for example 10.13 kPa) and the high-pressure density and viscosity correspond to those properties at the desired pressure condition. In other words, this method relies on having some other method for computing density and viscosity at high pressures. Fortunately, numerous such methods exist.

Summing the Fickian diffusion flux with the Darcy convection flux results in approximately correct net flux in high-permeability media, but this method of segregating diffusion from convection does not apply in Knudsen flow conditions. In these conditions, the mechanism of ordinary diffusion must be coupled both to the porous medium and to the streaming molecular fluid. This coupling is accomplished using the dusty-gas model,

$$\sum_{j\neq i}^{n}\frac{x_i N_j^D - x_j N_i^D}{D_{ij}^e} - \frac{N_i^D}{D_i^K} = \frac{p_i\nabla x_i}{ZRT} + \left(1 + \frac{kp}{\mu D_i^K}\right)\frac{x_i\nabla p_i}{ZRT} \quad \text{.....(2.22)}$$

The dusty-gas model is a system of linear equations that must be solved for the fluxes of each species. The dusty-gas model was derived by treating the porous medium as an extra gas component comprised of large, heavy particles. In this way, the interaction of the porous medium with the flowing gas is correctly captured. Adding together Fickian and convective flow terms is known to yield incorrect fluxes, and the dusty-gas model is the correct alternative (Webb, et al. 2003; Veldsink et al. 1995; Doronin et al. 2004).

2.3.4 Configurational Diffusion

Configurational diffusion occurs within the smallest pores, where the molecule is similar in size to the pores. Configurational diffusion is important in transport in biological systems and zeolites (Watanabe et al. 2008). Movement of a non-spherical molecule through pores may depend on the orientation of that molecule relative to the pore, or even the orientation of chemically affine loci on the molecule (Do 1998).

Even very large hydrocarbon molecules such as asphaltenes are rarely larger than 10 nm in length. Kerogen pores smaller than 20 nm are uncommon. In this work, we disregard the impact of configurational diffusion.

2.3.5 Surface Diffusion

Surface diffusion is thermal diffusion on an adsorptive surface. Molecules adsorbed to a surface still experience thermal vibration and may gain enough thermal energy to jump between adjacent adsorption sites on the surface (Do 1998).

Due to the large surface area of kerogen and the corresponding high volume of adsorbed gas, surface diffusion may contribution significantly to total flux in shale. Surface diffusion may in fact be the *dominant* diffusion mechanism in coal (Fathi and Akkutlu 2009).

Fathi and Akkutlu (2009) illustrate how pore-scale heterogeneity leads to enhanced surface diffusion. Using perturbation theory they derive an upscaled effective diffusivity which takes into account the fact that pore-scale heterogeneity amplifies diffusivity.

$$D_{s,eff} = \overline{D}_s - \frac{\sigma_\phi^2}{\overline{\Phi}} \left\{ \begin{array}{l} \dfrac{2D' D_s' \overline{\Phi} + \left(\overline{\Phi} D_s' - D_s'\right)\left(\beta g' + \dfrac{\overline{D} + \beta g}{\overline{\phi}}\right)}{\overline{D} + 2\beta g + \upsilon_1 \overline{\Phi}\, \overline{D}_s \overline{K}} + \\ \dfrac{\overline{K}\upsilon_1 \left[\left(D_s' - \dfrac{D_s'}{\overline{\phi}}\right)\left(\overline{\Phi} D_s' - D_s'\right) + \left(\overline{\Phi} D_s' - D_s'\right)^2\right]}{\overline{D} + 2\beta g + \upsilon_1 \overline{\Phi}\, \overline{D}_s \overline{K}} \end{array} \right\} \quad \text{.....(2.23)}$$

Fathi (2011) goes on to describe other upscaled transport parameters (and defines these variables) and also describes how the Langmuir isotherm equation can be modified by adding a term which directly accounts for heterogeneity.

Fathi (2011) begins with a nonlinear transient desorption kinetics model,

$$\frac{\partial C_\mu}{\partial t} = k_f \left(C_{\mu s} - C_\mu\right) C - k_r C_\mu \quad \text{.....(2.24)}$$

At thermodynamic equilibrium this equation simplifies to the Langmuir isotherm where

$$C_\mu = \frac{C_{\mu s} \frac{k_f}{k_r} C}{1 + \frac{k_f}{k_r} C} = \frac{C_{\mu s} K C}{1 + K C} \quad \text{.....(2.25)}$$

Eq. 2.25 is then incorporated into the overall mass balance equation,

$$\phi \frac{\partial C}{\partial t} + (1-\phi) \frac{\partial C_\mu}{\partial t} = \nabla \bullet (\phi D \nabla C) + \nabla \left(\phi C \frac{k}{\mu} \nabla p \right) + \nabla \left[(1-\phi) D_s \frac{\partial C_\mu}{\partial t} \right] \quad \text{.....(2.26)}$$

Fathi and Akkutlu (2011) show that effective surface diffusion rates are enhanced by accounting for this effect significantly beyond what would be naively expected.

2.3.6 Liquid Diffusion

Thermal diffusion occurs within liquids as well as gases. In liquids, the diffusion rate is orders of magnitude slower than in gas, due to the closely packed molecular nature of liquids (Bird et al. 2007). Diffusion in liquids is governed by Fick's law.

2.4 Macro-Scale Flow Regimes

Economically productive wells producing from shale gas reservoirs tend to be long horizontal wells with multi-stage hydraulic fracture treatments. Large volumes of water and proppant are pumped through perforated intervals in sequential stages at pressures sufficiently high to fracture the formation. The stimulation fluid and proppant flows into the induced fracture system and provides a permeable pathway connecting the distant formation to the wellbore (Mattar et al. 2008).

Over time the view of what this created fracture system looks like has evolved. Early models depict the fractures as essentially planar features intersecting the wellbore orthogonally. A more recent popular model of the fracture system is the "stimulated reservoir volume" (SRV). The SRV model assumes that a large volume of rock surrounding the wellbore has been fractured in a complex way generating a local "fractured reservoir" or dual porosity region (Mayerhofer et al. 2008). Warren and Root (1963) first modeled the concept of dual porosity flow, which approximates flow through the SRV. It is generally accepted that the reality is somewhere between these two ideals. Dominant, long planar fractures may exist, but a secondary fracture network may also overlay the reservoir volume near these primary fractures (Mattar et al. 2008; Clarkson et al. 2011). This spectrum of fracture configurations is partially represented in Figure 2.3.

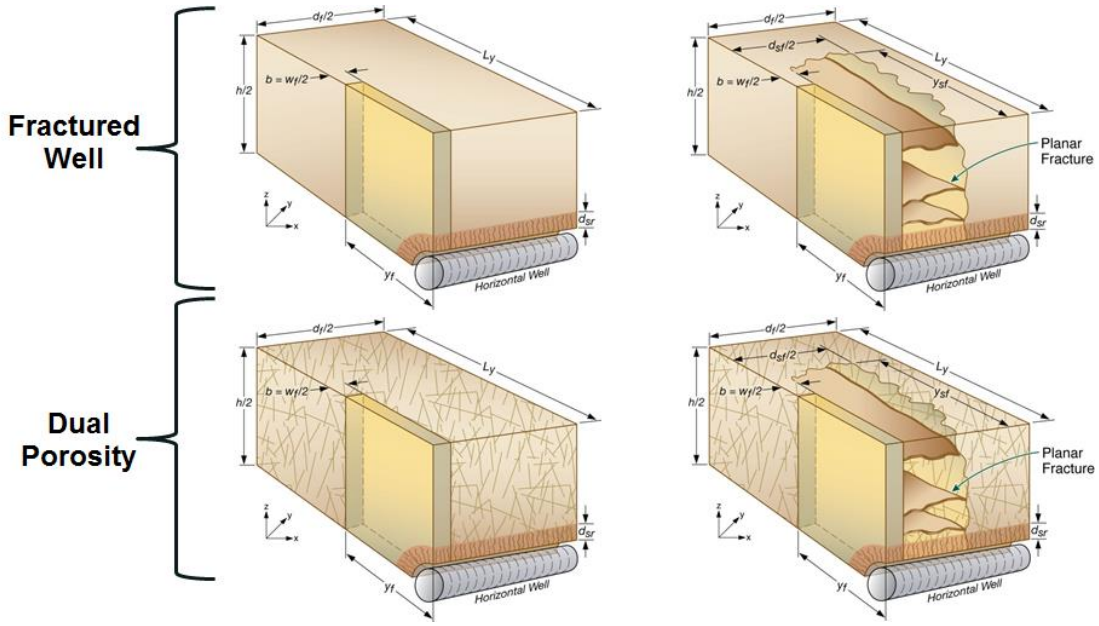

Figure 2.3 — Hypothetical induced and natural fracture configurations near shale gas wells (Moridis et al. 2011).

The field of production data analysis concerns itself with discovering diagnostically useful signatures within the flowing rate and pressure data obtained from wells. The flow regime under which a well is producing can be identified in the well's production data. The signature of linear flow into a single vertical fracture, for example, is identifiable as a negative one-half slope on a logarithmic plot of rate versus time (Ilk et al. 2011).

van Kruysdijk and Dullaert (1989) first discussed the flow regimes and associated production data signatures which occur in horizontal wells with multiple transverse hydraulic fractures. In this case, reservoir flow undergoes an early linear flow period as the flow field surrounding each of the individual transverse fractures resembles linear flow. This linear flow period is followed by a period known as "compound linear flow." In the compound linear flow period, the pressure transients of the individual fractures interfere and merge into a compound transient encompassing the entire well-fracture system. This compound transient then propagates out parallel to (away from) the horizontal wellbore and into the formation. These van Kruysdijk and Dullaert flow regimes explain why it is that the region between the fractures experiences far greater drawdown than the region beyond the fracture tips.

Flow inside the fractures may be non-Darcy or turbulent, requiring more complex models to correctly capture the flow rate as a function of pressure drop (Frederick and Graves 1994; Forchheimer 1901; Kutasov 1993).

In field applications, the production data measured from shale gas wells is often noisy and interrupted by shut-ins and other surface operations. Consequently, the hypothesized production data signatures are difficult to identify (Clarkson et al. 2011).

CHAPTER III
NUMERICAL MODEL DESIGN

3.1 Introduction to the TOUGH+ Code

The code base from which the numerical model of this work was developed is the TOUGH+ (TOUGH+ 2009) fluid flow code. The TOUGH family of simulation tools for multiphase flow and transport processes in permeable media was developed at and is maintained by researchers in the Earth Sciences division of Lawrence Berkeley National Laboratory. The specific branch of code which served as the starting point for this work is TOUGH+, which is an object-oriented version of TOUGH written in Fortran 95.

Fortran is a programming language particularly suited for numeric computation and scientific applications. The language was specifically developed for fast and efficient mathematical computations. The mathematical operators in Fortran (such as addition, multiplication, etc.) are intrinsic precompiled binaries rather than invoked classes, making Fortran faster than other popular languages such as C++ (Chapman 2008).

Fortran is thus particularly well-suited to reservoir simulation. Fortran is a popular language for scientific computing in general due to its speed at arithmetic, and due to the availability of highly optimized linear solver libraries written in that language.

Once again, our primary objective is to capture the relevant physical mechanisms of transport and storage in tight/shale gas reservoir systems. To this end, a number of distinct physical mechanisms had to be modeled. Some of these features ("conventional" features) have been thoroughly described in the literature, and may be found in other numerical simulation software. However, the incorporation of all of the conventional features in this work together in a single unified model represents a novel contribution. Other of these features ("unconventional" features) have rarely or never been considered in the petroleum engineering literature and so represent new considerations in the discipline.

3.2 Code Modifications

The fundamentals of petroleum engineering reservoir simulation are well-established in the literature. In lieu of a detailed discourse on reservoir simulation basics, we will here describe the specific implementations included in our model.

As received, the TOUGH+ (TOUGH+ 2009) code was capable of isothermal black-oil flow. The code used in this work has been extended to include the features relevant to flow in shale gas/tight gas reservoir systems. Two-phase flow of aqueous and gas phases is modeled. Both phases are treated compositionally, where the properties of methane, ethane, water, carbon dioxide, etc. are treated independently, as opposed to the simplified "black oil" model.

The finite volume form of the mass balance equation is:

$$\frac{d}{dt}\int_{V_n} M^{\kappa} dV = \int_{\Gamma_n} \mathbf{F}^{\kappa} \bullet \mathbf{n} d\widetilde{A} + \int_{V_n} q^{\kappa} dV \quad \text{.....(3.1)}$$

The mass accumulation term is expressed as

$$M^{\kappa} = R_L^{\kappa} + \sum_{\beta=A,G,O} \phi S_{\beta} \rho_{\beta} X_{\beta}^{\kappa} \quad \text{.....(3.2)}$$

with

$$\kappa = \mathrm{H_2O}, \mathrm{C_1 - C_6}, \mathrm{CO_2};\ R = \text{sorbed} \quad \text{.....(3.3)}$$

and using the Langmuir isotherm (or some other sorption model),

$$R_L^{\kappa} = \frac{V_L^{\kappa} b_L^{\kappa} p y^{\kappa}}{1 + \sum_j b_L^j p y^j} \quad \text{.....(3.4)}$$

Models exist which account for gas pore volume restriction with adsorption. This will manifest as a modification of the phase saturations.

The heat accumulation is expressed as

$$M^{\theta} = (1-\phi)\rho_R C_R T + \sum_{\beta=A,G,O} \phi S_{\beta} \rho_{\beta} U_{\beta} + U_R \quad \text{.....(3.5)}$$

The internal energy of the gas phase is

$$U_G = \sum_{\beta=A,G,O} X_G^{\kappa} u_G^{\kappa} + U_{dep}\left(= H_G - \frac{p}{\rho_G} \right) \quad \text{.....(3.6)}$$

The internal energy of the aqueous phase is dependent on the dissolved gas and solute,

$$U_A = X_A^{\mathrm{H_2O}} + X_A^{\mathrm{C_n}} \left(u_A^{\mathrm{C_n}} + U_{sol}^{\mathrm{C_n}} \right) + X_A^{\mathrm{s}} \left(u_A^{\mathrm{s}} + U_{sol}^{\mathrm{s}} \right) \quad \text{.....(3.7)}$$

The specific internal energies of each species at the prevailing conditions are expressed as

$$u_A^{\kappa} = h_A^{\kappa} - \frac{p}{\rho_{\kappa}} = \int_{T_0}^{T} C_{\kappa} dT - \frac{p}{\rho_{\kappa}} \quad \text{.....(3.8)}$$

The description of mass-energy balance for the organic phase is analogous in its development.

The fluxes are expressed by

$$\mathbf{F}^{\kappa} = \sum_{\beta=A,G,O} \mathbf{F}_{\beta}^{\kappa} \quad \text{.....(3.9)}$$

With $\kappa = \mathrm{H_2O}, \mathrm{C_1 - C_6}, \mathrm{CO_2}$

For the aqueous phase,

$$\mathbf{F}_A = -k \frac{k_{rA} \rho_A}{\mu_A} \left(\nabla p_A - \rho_A \mathbf{g} \right) \quad \text{.....(3.10)}$$

In this implementation, the pressure of the water phase is related to the pressure in the other phases by a capillary pressure relationship. For example,

$$p_A = p_G + p_{cGW} \quad \text{.....(3.11)}$$

where

$$p_G = p_G^{C_n} + p_G^{H_2O} \quad \text{.....(3.12)}$$

where p_{cGW} is the gas-water capillary pressure. The gas solubility in the aqueous phase is determined through Henry's law.

When the pore throats of the porous media are sufficiently small, i.e. when flow is dominated by the Knudsen flow regime, the gas phase flux is computed in a significantly different manner. The dusty gas model is required for accurate computation of multicomponent gas flow through very low permeability porous media where diffusion may be important. The dusty gas model in its ideal form is a system of equations expressed by

$$\sum_{j\neq i}^{n} \frac{x_i N_j^D - x_j N_i^D}{D_{ij}^e} - \frac{N_i^D}{D_i^K} = \frac{\left(\nabla p_i - \rho_g g\right)}{RT} \quad \text{.....(3.13)}$$

Where N^D is the molar diffusive flux and x is the mole fraction. Ignoring gravity, it is more straightforward to write

$$\sum_{j\neq i}^{n} \frac{x_i N_j^D - x_j N_i^D}{D_{ij}^e} - \frac{N_i^D}{D_i^K} = \frac{x_i \nabla p}{RT} + \frac{p \nabla x_i}{RT} \quad \text{.....(3.14)}$$

Clearly the molar flux is a function of composition gradient and pressure. The single component form of the dusty gas model is

$$N_1^D = -D_i^K \frac{\nabla p}{RT} \quad \text{.....(3.15)}$$

The dusty gas model should be modified as follows for a real gas:

$$\sum_{j\neq i}^{n} \frac{x_i N_j^D - x_j N_i^D}{D_{ij}^e} - \frac{N_i^D}{D_i^K} = \frac{p_i \nabla x_i}{ZRT} + \left(1 + \frac{k_G p}{\mu D_i^K}\right) \frac{x_i \nabla p_i}{ZRT} \quad \text{.....(3.16)}$$

where the gas compressibility factor is taken at prevailing conditions. The dusty gas model is used to compute fluxes in the gas phase and Darcy's law is used to compute fluxes in the liquid phase. The relative permeability of the gas phase is a function of the phase saturation.

Discretization of the time and space solution domains is performed using dynamic time-step adjustment and extremely fine spatial gridding in three dimensions. In the course of this work, a tool capable of generating Voronoi grids for TOUGH+ was developed based on the Voro++ library (Rycroft 2009). Voronoi grids are unstructured, meaning irregular objects such as crooked wells and nonplanar fractures can be accurately captured. Previous work (Freeman et al. 2009; Freeman et al. 2010; Freeman et al.

2011; Freeman 2010a; Freeman 2010b) involved the creation of accurate representative simulation grids for the case of horizontal wells with multiple transverse artificially induced fractures. These grids exhibit refinement where necessary to capture specific features of large-scale flow behavior – namely, the evolution of flow regimes over time, and how these flow regimes relate to well performance.

The equations describing mass flux between grid blocks and mass accumulation within grid blocks are solved simultaneously to within a specified numerical tolerance. The solution is obtained using Newton's method, linearized via the Jacobian matrix. We are now able to discuss the manner in which the terms of these equations are computed in a given internal iteration.

The model has been extended to offer increased flexibility in how the thermophysical properties are computed. This flexibility is required when coupling disparate models of transport and storage. The primary mode of computing gas density is the Peng-Robinson (Peng and Robinson 1976) equation of state as a function of the pressure, composition, and temperature value of the grid element. The primary method used to calculate the gas phase viscosity is the Chung et al. (1988) model. The saturated dissolution concentration of the gas species in the aqueous phase is computed by use of Henry's parameter. Multiple options are included for the modeling of two-phase flow dependent properties. Primarily, the van Genuchten (1980) model is used for capillary pressure determination, and the Corey (1957) model is used for relative permeability determination.

In the case of two-phase water-gas flow and single-phase gas flow, the primary variables of simulation are pressure and mole fractions of the individual gas species in the gaseous phase. Where only one gas component is present (typically a pure methane simulation) then the only primary variable is pressure. In cases where thermal considerations are considered to be important, there is the potential for temperature to be included as the final primary variable.

3.3 Mesh Generation

A substantial portion of the overall code development effort was devoted to improving the mesh generation capabilities of the TOUGH family of codes culminating in the development of an independent set of software tools, MeshVoro (Freeman et al. 2013), which leverages the Voro++ code library (Rycroft 2009) for Voronoi (1908) mesh generation. This was undertaken in order to provide a means to efficiently generating meshes representing shale gas well systems. Shale gas wells typically involve horizontal wells with transverse fractures. From a meshing perspective, wells are long, thin cylindrical objects, sometimes with multiple concentric regions of interest (e.g. tubing, annulus, casing, cement) while fractures are typically treated as thin elliptical or rectangular regions. Creating a mesh which correctly respects the intersection of these geometries in a flexible fashion is a difficult problem.

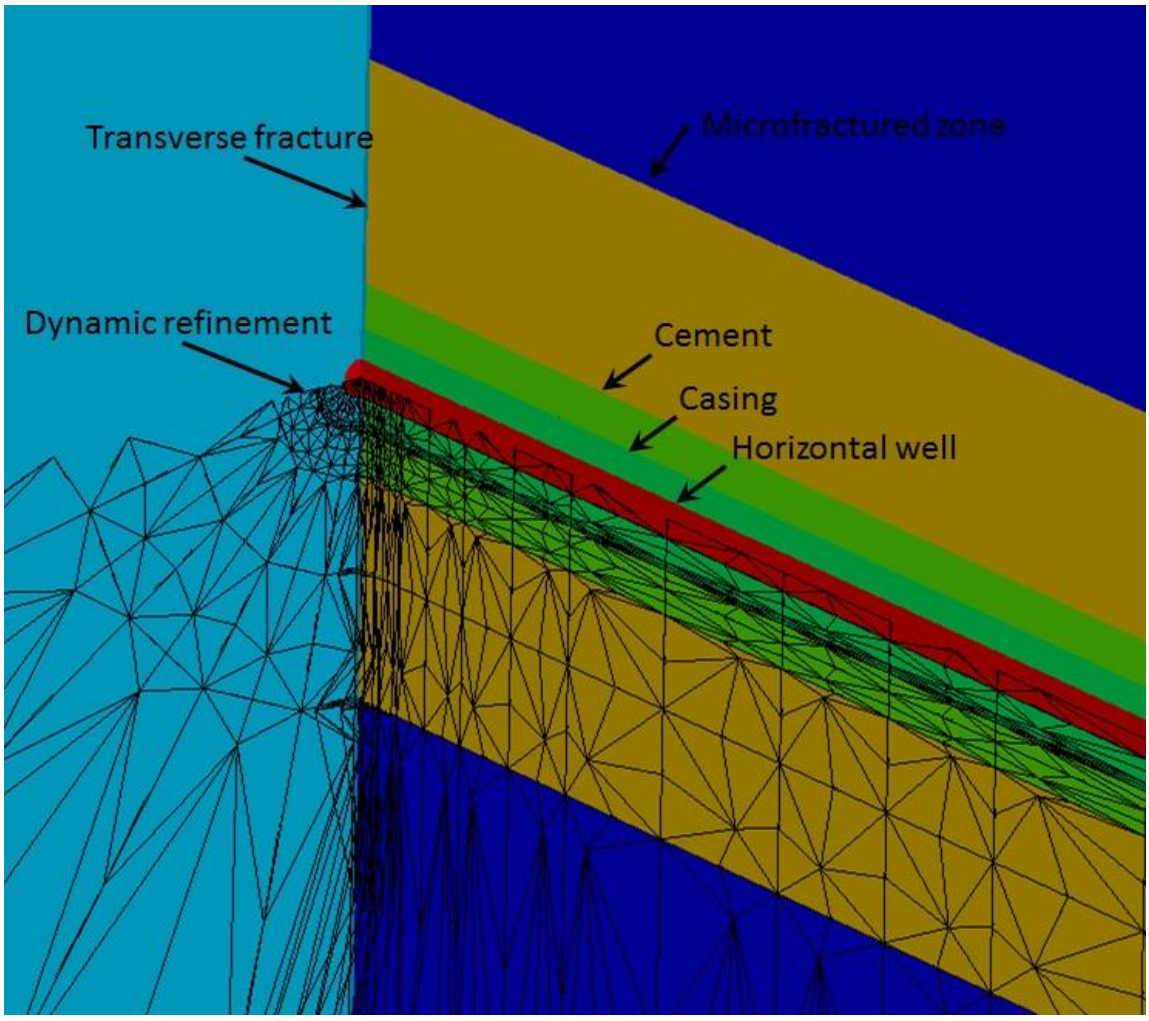

Figure 3.1 — Annotated figure generated by MeshVoro (Freeman et al. 2013) depicting the intersection of a thin transverse fracture (pale blue) with a horizontal well comprised of multiple regions of interest. The lower half of the figure shows the refinement of the grid elements, which is pseudo-radial moving outward from the well and rectilinear moving along the well's axis.

The MeshVoro mesh generation tool permits precise and efficient creation of meshes refined in three dimensions allowing for all of these factors, as depicted in Figure 3.1. A complete description of the improvements may be found in Freeman et al. (2013).

CHAPTER IV
FIELD DATA DIAGNOSTICS

4.1 Rationale for Compositional Diagnostics

Chapter I described the problem being addressed in this work and the intermediate objectives required to solve it. In summary, the goal is to use measured flowing gas composition data from shale gas wells to improve reservoir characterization. In Chapter II we discuss the various mechanisms of transport and storage in shale that lead to compositional change, and the available models for characterizing these mechanisms. We also discuss the complex evolving flow regimes which may exist in shale gas well systems, and how these flow regimes can be identified in production data. Understanding flow regimes leads to an improved reservoir characterization and consequently more precise reserves estimates and more efficient reservoir development. Chapter III outlines how the relevant physical features were implemented into the numerical model, TOUGH+.

The goal behind creating this model is to provide the basis for a new method of production data analysis built upon analysis of flowing composition data in addition to flowing rate and pressure data. Using this model it is possible to generate large numbers of synthetic cases – hypothetical reservoir states and the flowing composition, rate and pressure data that these hypothetical reservoirs would produce. In doing so, the underlying characteristic behaviors in production data can be tied to the initial reservoir states which generated them. Then these characteristic behaviors can be identified in real production data, enabling a more precise reservoir characterization. The transition to compound-linear and then boundary dominated flow is apparent (although subtle) in the dimensionless rate data, but the transitional regimes are starkly apparent in the compositional deviation data. This suggests that compositional shift in produced gas may be a viable production analysis technique.

4.2 Discussion of Field Data Cases

We will examine production data from five wells in a North American shale gas play. Well A, Well B and Well C are located physically near one another. Well D and Well E are located near one another, but distant from Wells A through C. As we will observe, the wells which are physically proximal exhibit similar characteristics.

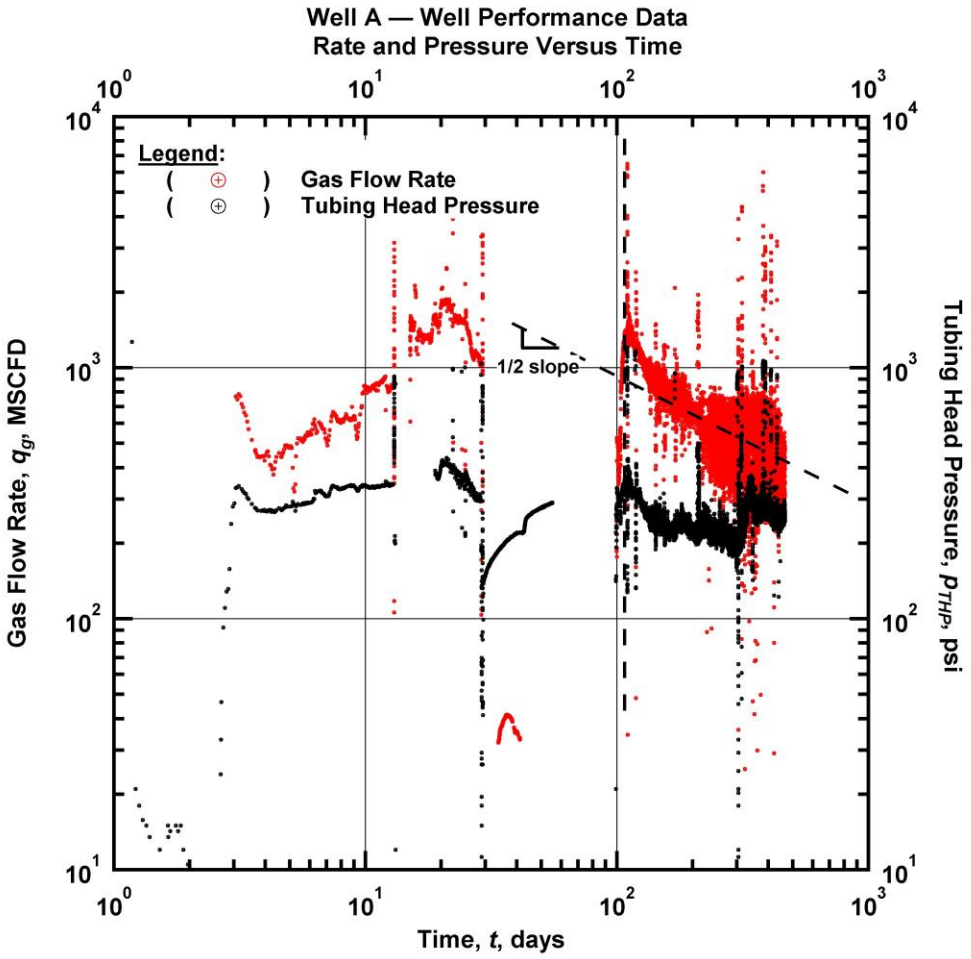

Figure 4.1 — (Log-log Plot): q and p versus t. Well A production data — production unstable for first hundred days.

High frequency rate and pressure data were obtained for these five wells. The rate and pressure data for Wells A, B, C, D and E are shown in Figures 4.1, 4.4, 4.7, 4.10, and 4.13, respectively. Additionally, fluid samples were obtained from the surface separators of these wells at semi-regular intervals. The chemical and stable carbon isotopic compositions of these samples were then measured. This provides a timeseries of surface flowing composition and isotope ratio for each of the wells, in addition to the traditional rate and pressure data. Taking fluid composition and stable carbon isotopic composition measurements on a repeated basis is atypical for oil and gas wells; these measurements were performed with the goal of providing data for the trend analysis performed in this work.

Trends in compositional change can be subtle and are difficult to visualize in absolute terms. For example, for Well B, the absolute measured methane composition goes from 79.7% methane and 0.5% n-pentane at the first measurement to 83.2% methane and 0.3% n-pentane at the last measurement. A shift

of 0.2% for n-pentane seems inconsequential compared to a 3.5% shift in methane concentration. However, if the compositions are normalized by their initial measured value, then general trends emerge clearly. Primarily, in each of the five wells (e.g. Figure 4.5) we observe that the relative composition of methane increases and the compositions of each of the heavier components decrease. Generally speaking, the relative compositional decline of heavier molecular species is greater than that of lighter species. Moreover, minor fluctuations in composition of only one component can be treated as noise, but compositional deviation of all of the molecular species at the same time in the same direction provides a clear signal that can be interpreted above sampling variability or analytical error.

The series labeled Compositional Deviation displayed in Figure 4.2 is simply the ratio of the composition for each gas component at time *t* divided by its initial composition at the first measurement.

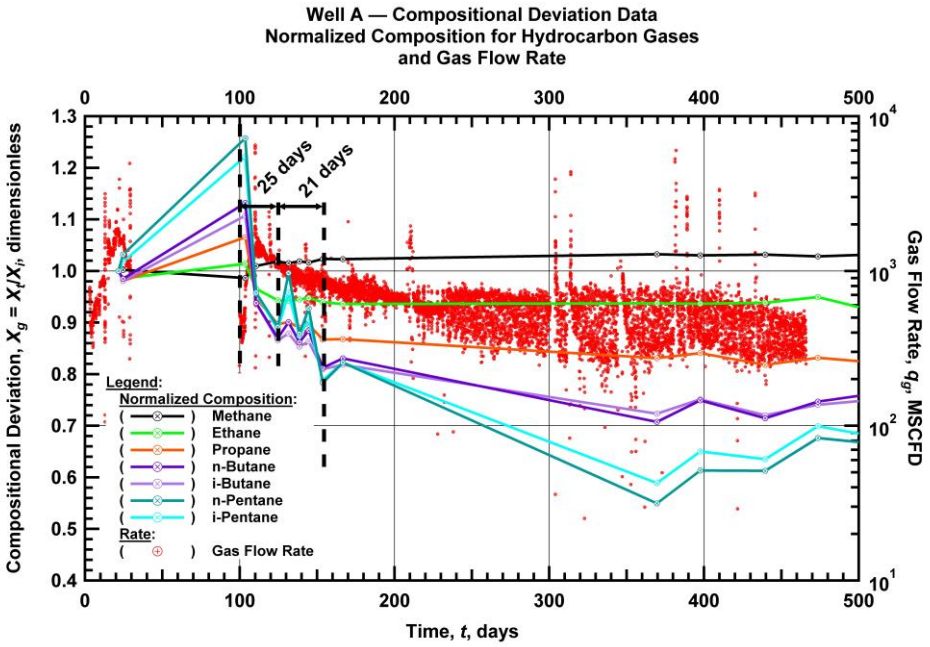

Figure 4.2 — (Semi-log Plot): q and X_g for all components versus t. Well A production data — concentrations of heavier species fall for first 25 days, followed by a bump which lasts 21 days.

At first glance the data for each of the five wells may appear somewhat erratic. For example, in Figure 4.2 Well A appears to exhibit a pronounced spike in composition of heavy components after 100 days of producing time. However, we note first that the appearance of certain peaks in the data may be an artifact of the sampling frequency. In this case, as is apparent from the corresponding rate and pressure data in Figure 4.1, Well A underwent a lengthy period of no production after its initial completion and an early

flow period. Therefore, this data point at 100 days simply indicates that the reservoir condition had progressed toward a new equilibrium during the shut-in time after the initial flow period. We see similar spikes in the composition and isotopic deviation data following interruptions, shut-ins and increases in flow rate for the other wells. Specifically, in Figure 4.5 for Well B at 340 days, potentially several times for Figure 4.11 Well D, and more subtly in Figure 4.14 for Well E after 300 days, there is a marked composition shift immediately following an operational change observable in the rate and pressure data.

These operationally induced compositional shift periods may provide useful diagnostic information, but we are more interested in the characteristic behavior of the reservoir system. We are concerned with the operationally induced fluctuations insofar as we wish to identify them and then isolate their influence from the underlying reservoir signature, which is of primary interest. This is an extension of the traditional production analyst's approach of using all available sources of data to clarify the reservoir characterization.

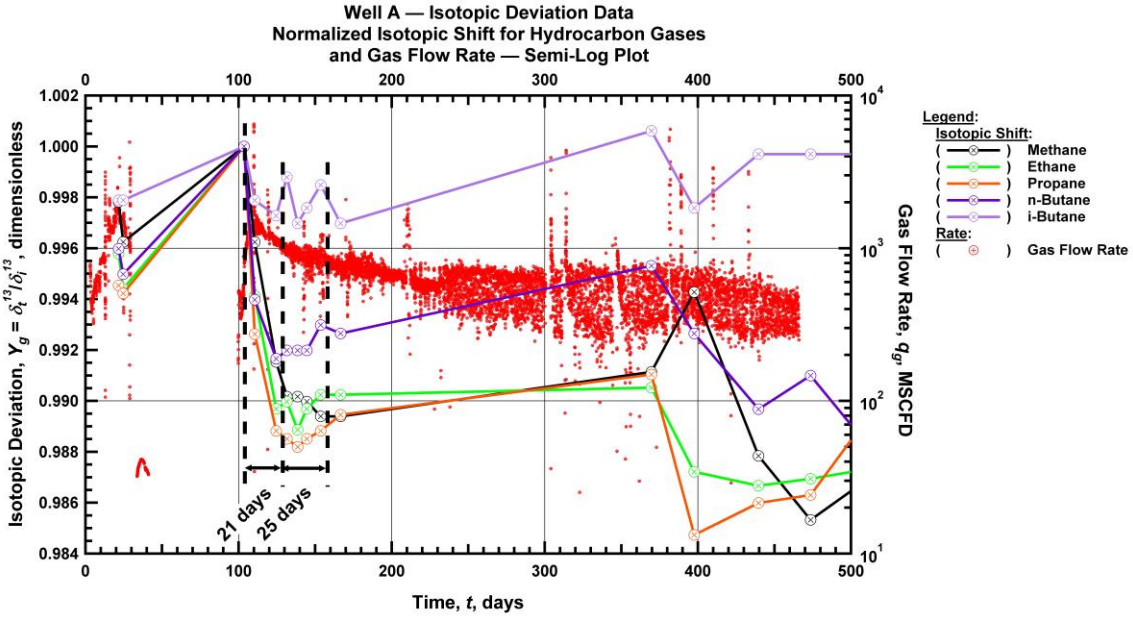

Figure 4.3 — (Semi-log Plot): q and Y_g for all isotopes versus t. Well A production data — isotopic shift for all components becomes gradually more negative for the first ~21 days, then begins to climb.

We observe similar operationally induced shifts in the flowing isotope composition data, as shown in Figure 4.3, as compared to Figure 4.2. We will discuss this issue in more detail in Section 4.3.

4.3 Analysis of Field Data

First we will examine Wells A, B and C. We tentatively expect that the underlying reservoir behavior for these three wells will be similar because the wells are located near one another and completed and stimulated with very similar fracture spacings and pumped volumes per stage.

For Well A we will ignore the initial flow period occurring within the first 30 days, as shown in Figure 4.2 and assume that the reservoir state is relatively stable starting at 100 days, when a lengthy, relatively constant period of production starts. Therefore we designate the effective start of production to begin at 100 days after initial flowback. We observe a general trend of declining composition of the heavier components, interrupted by a local peak which appears to begin 25 days after the effective start of production and returns to a flatter declining trend 21 days later.

The isotopic shift for Well A in Figure 4.3 indicates the stable carbon isotope value is actually becoming more heavy, less negative in the first 21 days and then starts to become more negative over time. A shift to more positive isotopic gas values is consistent with the fractionation affect associated with desorption of gas from kerogen (Strapoc et al. 2008). The shift to more negative values over time is more consistent with isotope fractionation associated with diffusion where the C^{12} travels faster than the C^{13} isotope. The isotope signature reflects a potential change from strong desorption influence early in the production to more diffusion influenced as production pressure is more stable or increases from 25+ days.

For Well B, in Figure 4.5 we again observe a general decline in the composition of the heavier components with time. However, the compositions of all of the heavier components appear to undergo a temporary increase in the form of a "bump" similar to the one observed in Well A. This local peak lasts about 25 days. The significant increase in composition at late time is due to the fact that the well rate and pressure change significantly at late time. This is an example of an operational change which we wish to extricate from the underlying reservoir behavior.

The isotopic deviation data for Well B in Figure 4.6 also exhibits a declining general trend with a more pronounced dip and then a peak. The lowest point occurs at about 20 days into production, coinciding with the dip in composition. The peak in the isotopic data occurs 25 days after this dip. Thus, both the compositional and isotopic shifts exhibit similar characteristics, particularly a shared local minimum.

Like Well A and Well B, Well C exhibits a generally declining compositional deviation trend in Figure 4.8, interrupted by a local peak. This lowest point before the bump occurs approximately 20 days into production and the peak occurs approximately 25 days after this.

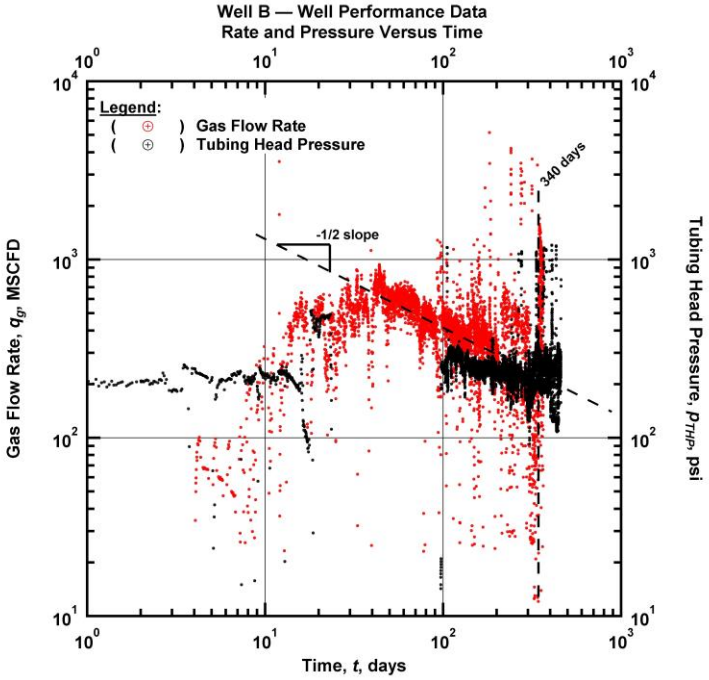

Figure 4.4 — (Log-log Plot): q and p versus t. Well B production data — rate data falls on a roughly -1/2 slope indicating linear flow.

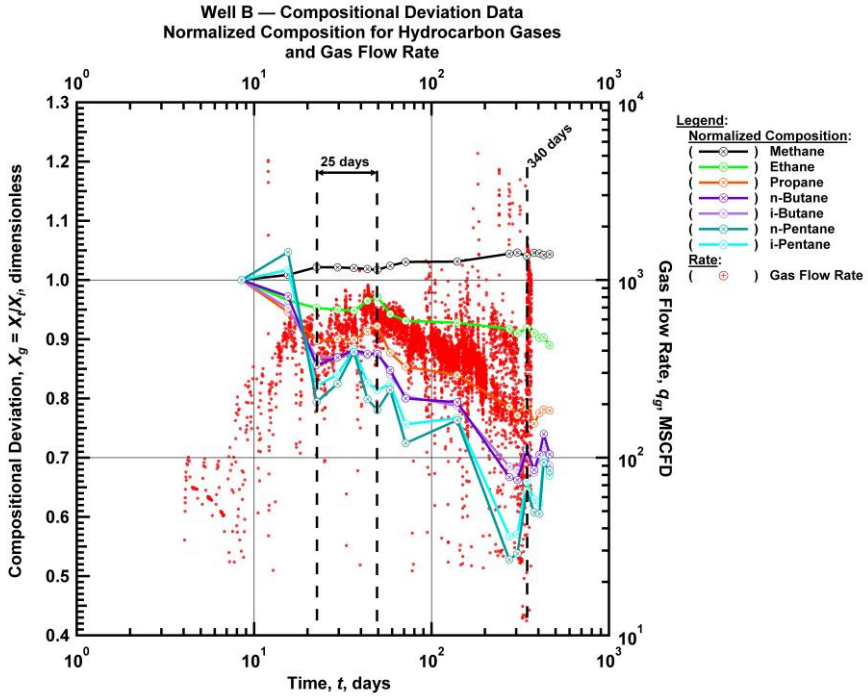

Figure 4.5 — (Log-log Plot): q and X_g for all components versus t. Well B production data — compositions of heavier components exhibit a bump lasting ~25 days.

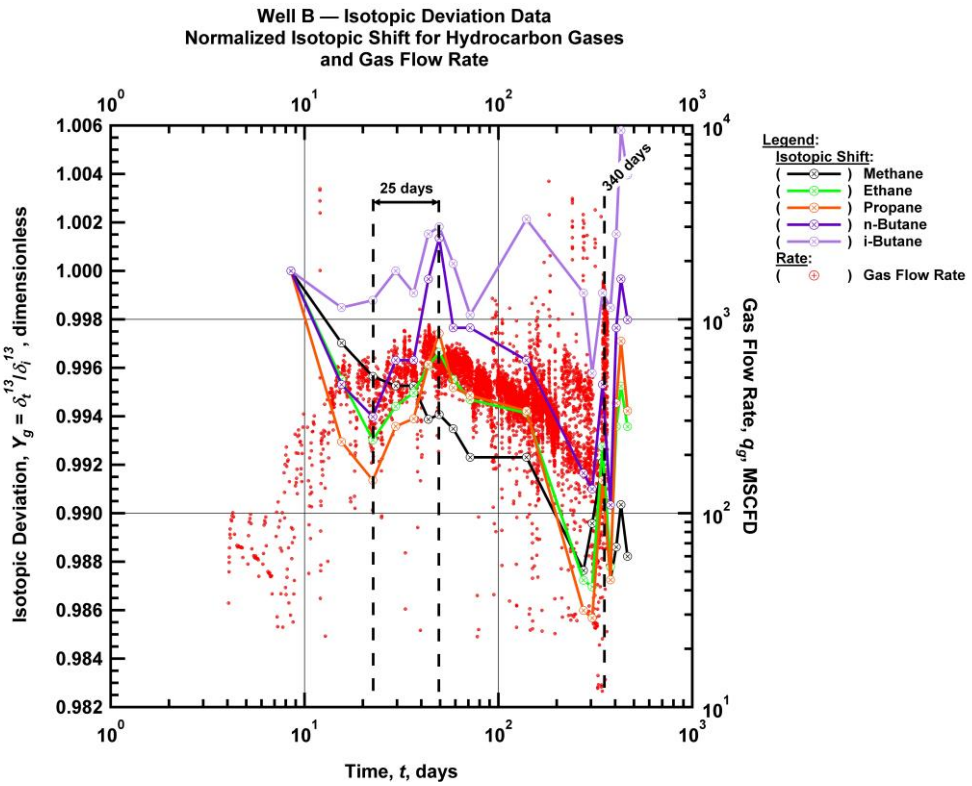

Figure 4.6 — (Log-log Plot): q and Y_g for all isotopes versus t. Well B production data — isotopic shift becomes more negative until prolonged "bump" starts. The start of this bump in the isotopic coincides with the start of the bump in the composition data.

The isotopic deviation trend for Well C in Figure.4.9 likewise possesses a spike which starts about 20 days into production and peaks 25 days into production. However, it is somewhat likely that this peak represents some form of error, possibly due to contamination, because it is significantly off the main trend.

These three wells (Well A, Well B and Well C) exhibit qualitatively similar compositional and isotopic behavior. In the case of Well B and Well C, the signatures in the isotopic behavior reflect the signatures in the compositional behavior. In all three cases there is a period of decline in the compositional deviation which lasts approximately 20 days, followed by a local spike in the composition of the heavier compounds which lasts on the order of 25 days, followed by a length period of slow decline in compositional deviation. These time periods are subject to uncertainty. First, the sampling frequency in some cases is not high enough to positively distinguish a particular peak as being real, as opposed to a temporary fluctuation or isolated measurement error. Indeed, the level of noise introduced by factors such as surface temperature and the presence of water in the separator is difficult to assess.

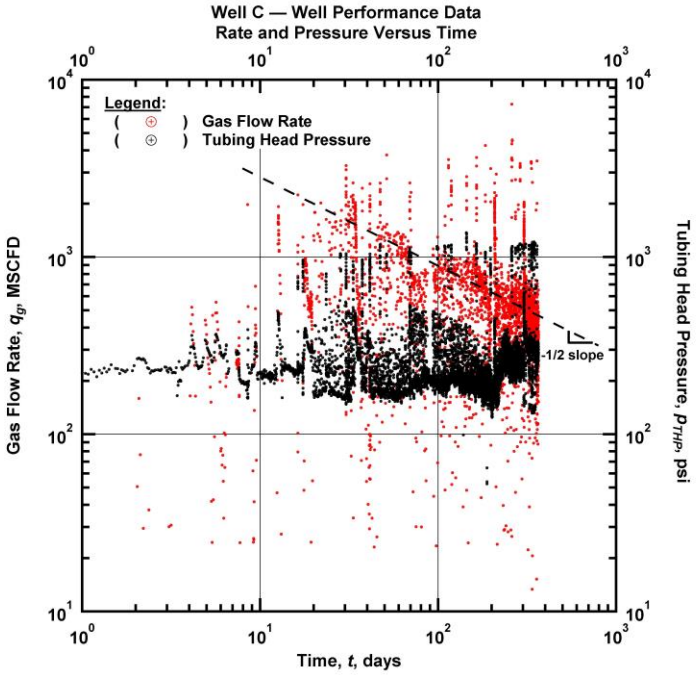

Figure 4.7 — (Log-log Plot): q and p versus t. Well C production data — -1/2 slope trend is apparent in later data indicating evolution of linear flow.

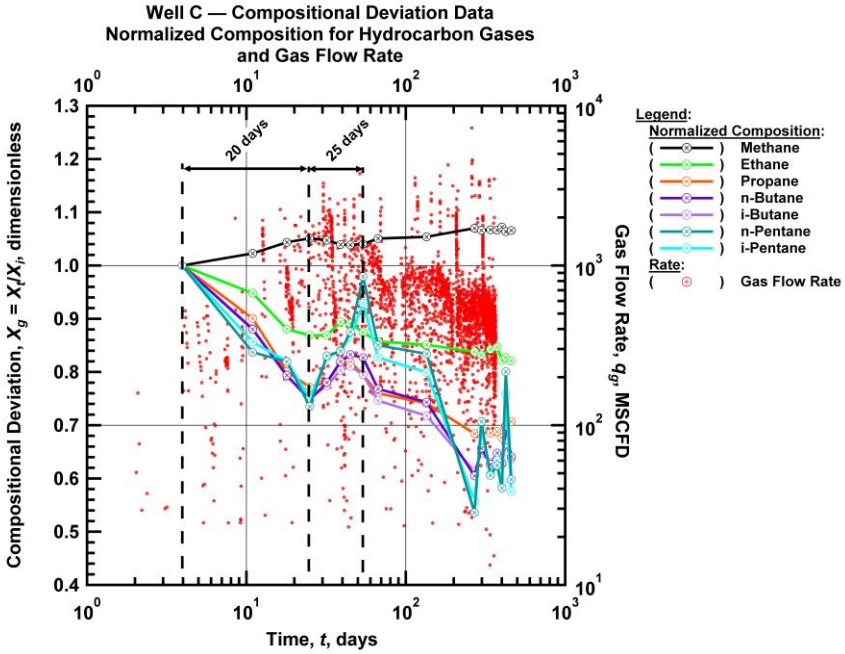

Figure 4.8 — (Log-log Plot): q and X_g for all components versus t. Well C production data — steady decline in composition of heavier components until 20 days, at which point a 25 day richening period begins.

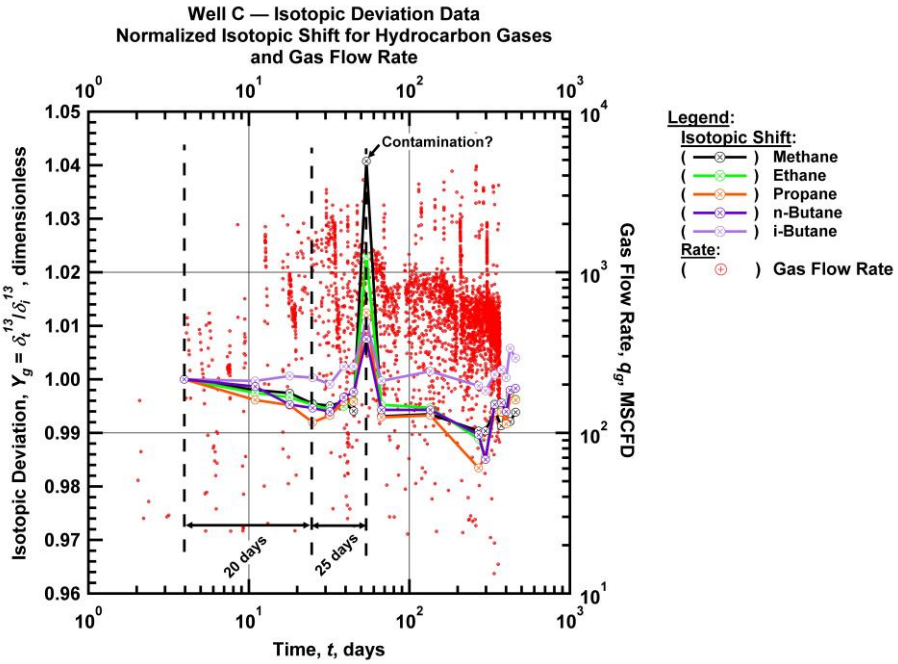

Figure 4.9 — (Log-log Plot): q and Y_g for all isotopes versus t. Well C production data — significant outlier may be the result of sample contamination.

Well D and Well E are located near one another, relatively distant from Wells A, B and C. The compositional and isotopic signatures for these wells appear more erratic. This may be because the rate and pressure data shown in Figure 4.10 and in Figure 4.13 indicate far less stable, less constant rate histories for these wells.

For example, the compositional deviation data for Well D in Figure 4.11 possesses multiple local peaks and minima. These local minima tend to coincide with operational interruptions. In particular, this well underwent a lengthy shut-in, as shown in Figure 4.10. This shut-in is of such duration (on the order of 50 days) that the reservoir and well system may have had time to reach a new equilibrium before production begins again. We attempt to identify three distinct local increases in isotopic deviation for the heavier components, each having approximately 10 day duration. The first of these local peaks begins 10 days into production. The second local peak begins shortly after a production interruption. The third local peak appears shortly after production resumes following the lengthy 50 day shut-in. We propose that each of these three local increases represents a transient response. Each time the well is shut in, the system begins to return to equilibrium. When flow is restarted, the system experiences a new transient perturbation. This 10-day long perturbation may indicate the time required for the pressure transient to fully investigate the fractured region and, following this, to return to pseudosteady-state flow.

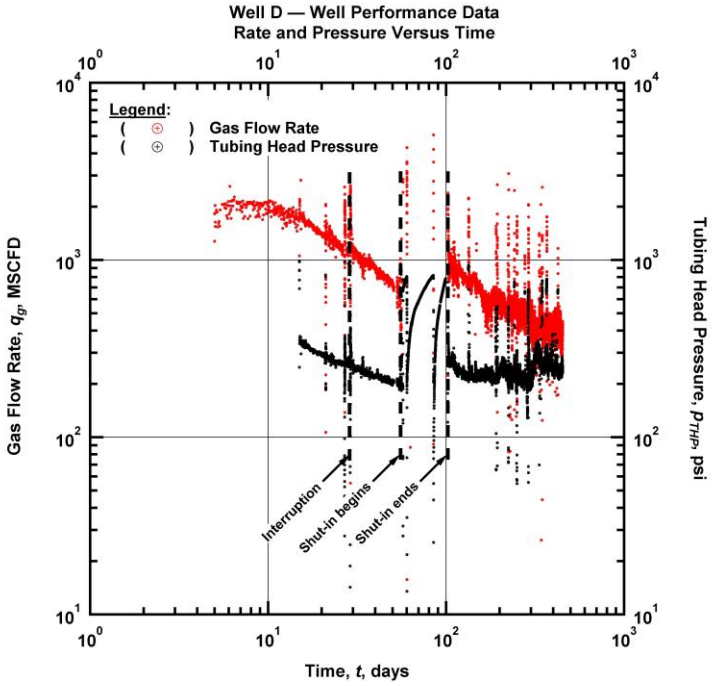

Figure 4.10 — (Log-log Plot): q and p versus t. Well D production data — two distinct producing trends are apparent, prior to and after a distinct shut-in. Both trends appear to be linear flow.

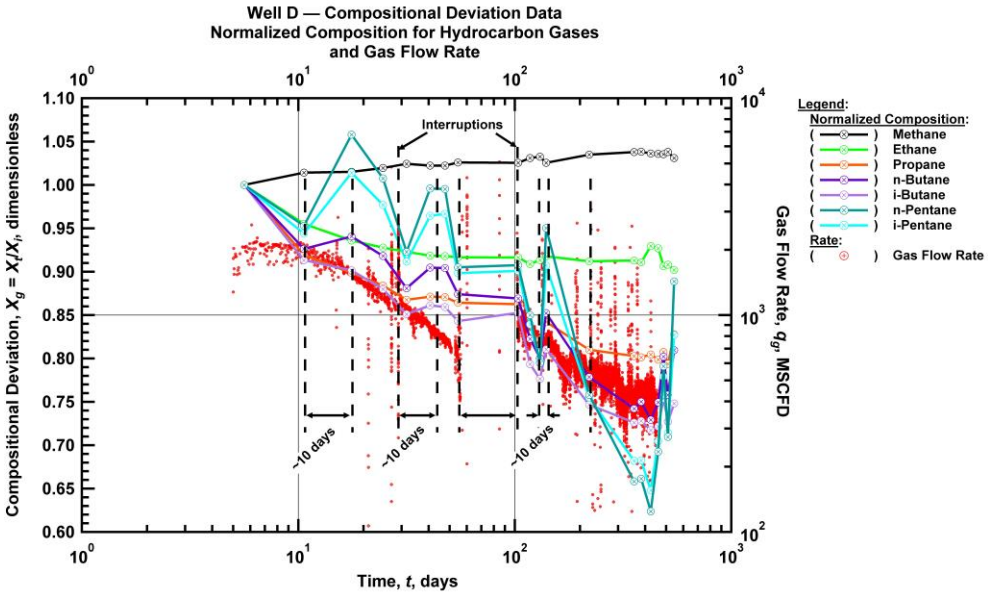

Figure 4.11 — (Log-log Plot): q and X_g for all components versus t. Well D production data — relatively noisy data, trends unclear, but after both the start of production and the resumption of flow after the shut-in, there is a ~10 day richening period.

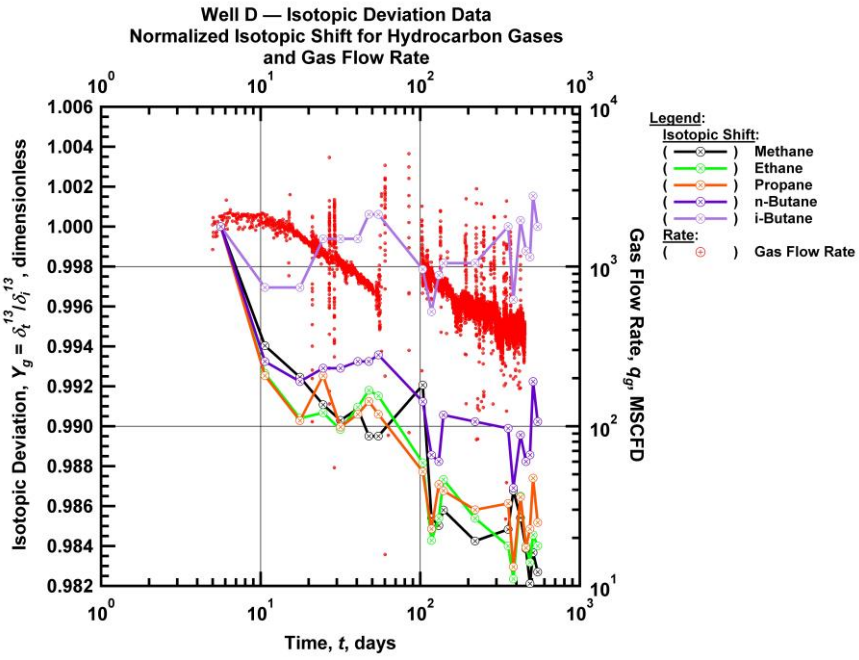

Figure 4.12 — (Log-log Plot): q and Y_g for all isotopes versus t. Well D production data — relatively noisy data, no distinct trends.

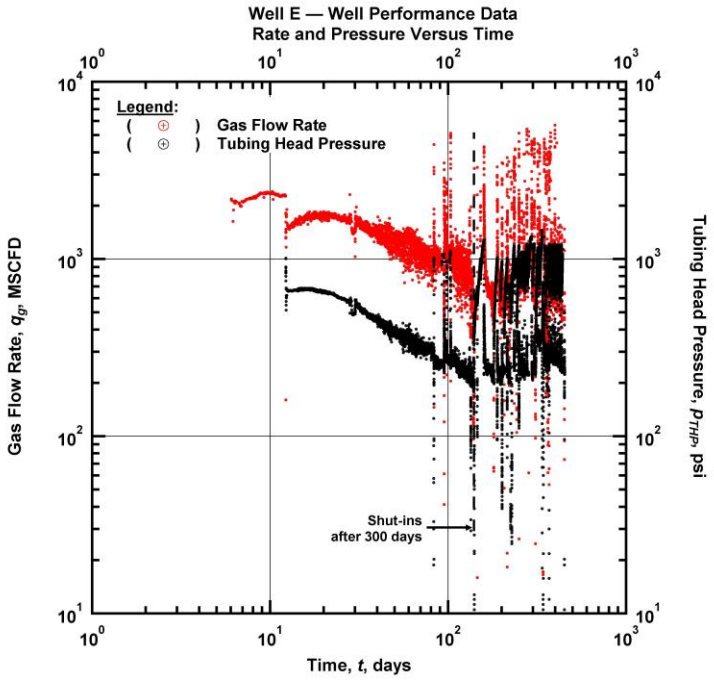

Figure 4.13 — (Log-log Plot): q and p versus t. Well E production data — clear -1/2 slope linear flow trend for the first ~100 days, followed by irregular production.

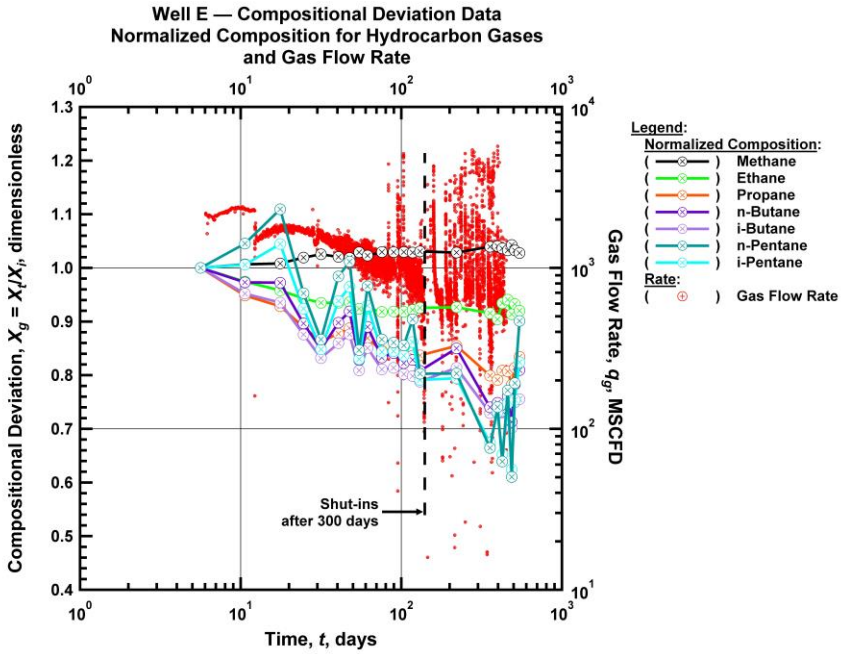

Figure 4.14 — (Log-log Plot): q and X_g for all components versus t. Well E production data — general leaning trend throughout most of well life with several fluctuations.

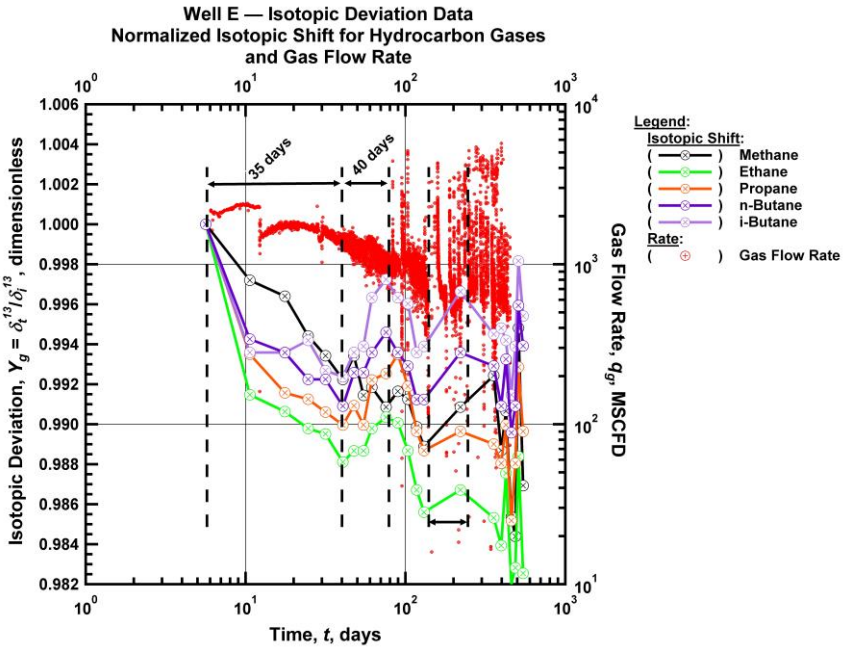

Figure 4.15 — (Log-log Plot): q and Y_g for all isotopes versus t. Well E production data — negative isotopic shift for first 35 days following by 40 day isotopic richening period.

The isotopic deviation data for Well D in Figure 4.12 appears relatively erratic and does not correlate well with the compositional deviation data.

The compositional deviation data for Well E in Figure 4.14 is also relatively erratic, possessing multiple local peaks over a gradual period of decline for the heavier components.

Well E is particularly interesting because it is the only case out of the five wells where the isotopic deviation data (Figure 4.15) provide an apparently more nuanced and detailed signature than the compositional deviation data. Using only the isotopic deviation data, we observe an initial 35 day period of decline in the relative composition of C^{13} followed by temporary increase which lasts 40 days. If this signature also illustrates the progress of the pressure transient through the near-well fractured system, then it may be the case that the fracture network for Well E is either larger or less transmissible than the fracture systems of Wells A, B and C, which exhibited much shorter apparent flow periods.

In some cases the trend in isotopic deviation fails to correspond to the trend in compositional deviation, while in other cases the two trends exhibit corresponding behavior. The reason for this could be as simple as a systematic source of measurement error for some of the wells but not others. It could also indicate different geology between wells. For example, a well with a significant contribution from desorption and other chromatographic processes would be expected to possess a clearer isotopic shift.

4.4 Numerical Model Results

We developed a numerical model derived from the TOUGH+ (2008) code for transport of fluid and heat through porous media, described in more detail in Chapter III. This code incorporates grids specifically tailored for shale gas systems (Freeman et al. 2009, Freeman et al. 2010) and a multicomponent Langmuir desorption model described in Eq. 2.5. The purpose of the numerical modeling is to simulate hypothetical physical scenarios which might explain the observed behavior in the North American shale gas wells described in the previous section.

4.4.1 Parameter Match to North American Shale Gas Field

We begin by generating a numerical model which approximates the estimated reservoir parameters of a typical well in the North American shale gas play examined in the field data analysis. The pertinent reservoir and completion parameters are contained in Table 4.4.

We note that parameters such as fracture half-length, matrix permeability, and *in situ* fluid composition are generally not known accurately. A method for accurate permeability characterization for shale gas reservoirs has not been established, as discussed in Section 2.3.1 on convective transport through shale. We therefore choose a permeability that we believe is supported by production data analysis for North American shale gas play from which the data originated.

Table 4.1 — Reservoir and well system parameters for North American shale gas play used in numerical simulations.

Parameters	SI Unit	Field Unit
Fracture half-length, x_f	152.4 m	500 ft
Fracture conductivity, C_{fD}	1310 -	1310 -
Fracture spacing, d_f	15.24 m	50 ft
Reservoir thickness, h	30.48 m	100 ft
Permeability, k_{shale}	1.0×10^{-19} m^2	1.0×10^{-4} md
Matrix porosity, ϕ	2.76 percent	2.76
Temperature, T	86.4 ^{0}C	187.52 ^{0}F
Well radius, r_w	0.1 m	0.32 ft
Reservoir pressure, p_i	3.15×10^7 Pa	4568 psia
Well pressure, p_{wf}	2.5×10^7 Pa	3626 psia

Fracture half-length can be roughly estimated by production analysis and by microseisemic monitoring. The degree to which the primary fracture induces secondary fracturing is also unknown and we provide various scenarios. The *in situ* fluid composition is impossible to determine because even samples retrieved from downhole are vented down to 300 psi at the surface for safety reasons. While the produced flowing composition of methane may be nearly 90%, the downhole composition of methane is much lower. We consider the downhole composition to be another unknown, and, related to this, we take some liberties in our determination of appropriate multicomponent Langmuir parameters. The experimental conditions at which Langmuir parameters for cores from these wells were obtained cannot be considered analogous to the reservoir conditions. Consequently, we treat the multicomponent Langmuir isotherm parameters as another unknown.

Table 4.2 — Langmuir and initial composition parameters used in Case 1.

Component	Y_i,	b_i, 1/psi	V_{Li}, scf/ton
Methane	0.80	2.08×10^{-6}	3.45×10^4
Ethane	0.07	2.11×10^{-4}	3.88×10^2
Propane	0.05	7.02×10^{-4}	1.9×10^2
Butane	0.05	3.84×10^{-4}	2.5×10^2
Pentane	0.02	8.10×10^{-5}	3.1×10^2
Hexane	0.01	1.21×10^{-5}	3.71×10^2

We first examine Case 1. In this case we have used the reservoir parameters from Table 4.4 and applied multicomponent Langmuir parameters from Table 4.2. The curves resulting from these parameters are visualized for the single-component Langmuir isotherm in Figure 4.16 and for the multicomponent

Langmuir isotherm in Figure 4.17. Originally we attempted to use Langmuir parameters obtained from core experimentation. However, the Langmuir desorption analyses available to us were performed using individual gases. In the cases where gas mixtures were used, the composition of the desorbing gas was not measured over time. Therefore, accurate multicomponent Langmuir parameters were unavailable, and we were forced to invent a set of parameters which result in the correct functional behavior within the required range of reservoir pressures. The primary requirement of the multicomponent Langmuir isotherm is that lighter components exhibit flatter sorption behavior through the reservoir pressure interval.

Plots of absolute composition versus time for shale gas wells usually do not show any interesting behavior because the trends tend to be relatively subtle. Plotting the compositional *deviation* instead of the absolute composition, defined as the composition at time *t* divided by the *in situ* composition, yields much more informative trends.

$$X = \frac{x_t}{x_i} \quad \text{.....(4.1)}$$

All compositional deviation trends tend to start at a value of 1.0 because the first gas that is produced is relatively unaffected by desorption.

For Case 1, as shown in Figure 4.18, first note that the rate-time behavior exhibits a clear signature showing distinctly the linear, transitional, and compound-linear flow periods for the multiply-fractured horizontal well. Because this is simulated data, we know exactly what flow effects are causing the fluctuations in produced gas composition. In this case, we observe the following relationships: during transient linear flow, the normalized composition of the heavier components is decreasing and flattening. At the onset of the transition period, at the instant the fracture transient reaches the adjacent transient, the normalized compositions of the heavier components begin to decline once again. During the transition to the second linear flow period, the compound-linear flow period, the normalized compositions of the heavier compounds begin to swing upward. At the end of the transition period and the onset of fully-developed compound-linear flow the compositions of the heavier compounds have reached a new local maximum point and begin to decline again.

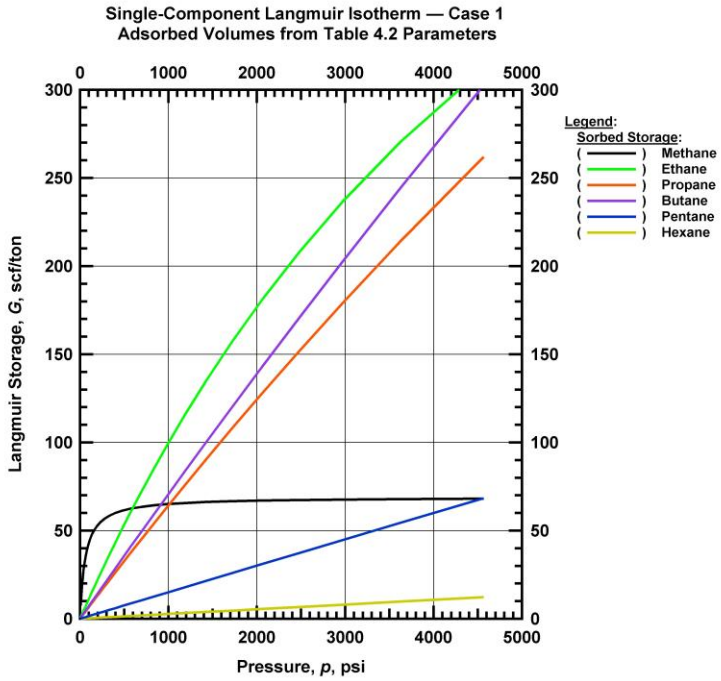

Figure 4.16 — Single-component Langmuir storage for methane through hexane versus *p*. Plot of Langmuir isotherm parameters used in Case 1 using Eq. 2.5.

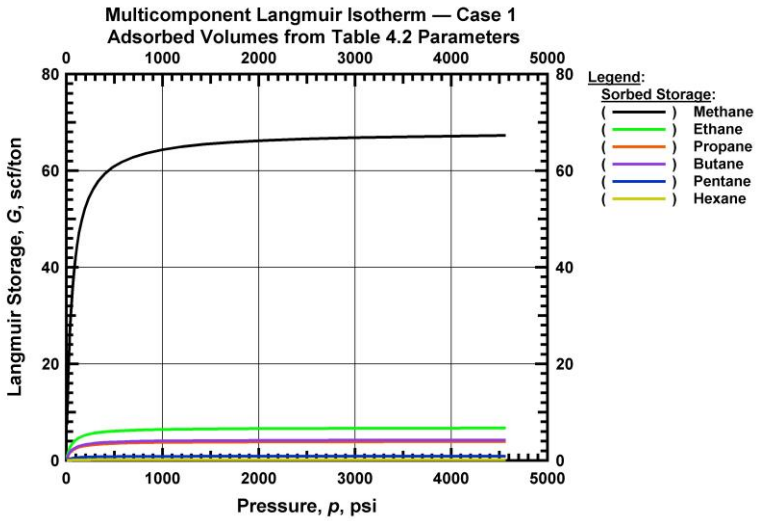

Figure 4.17 — Multi-component Langmuir storage for methane through hexane versus *p*. Plot of Langmuir isotherm parameters used in Case 1 using Eq. 2.5.

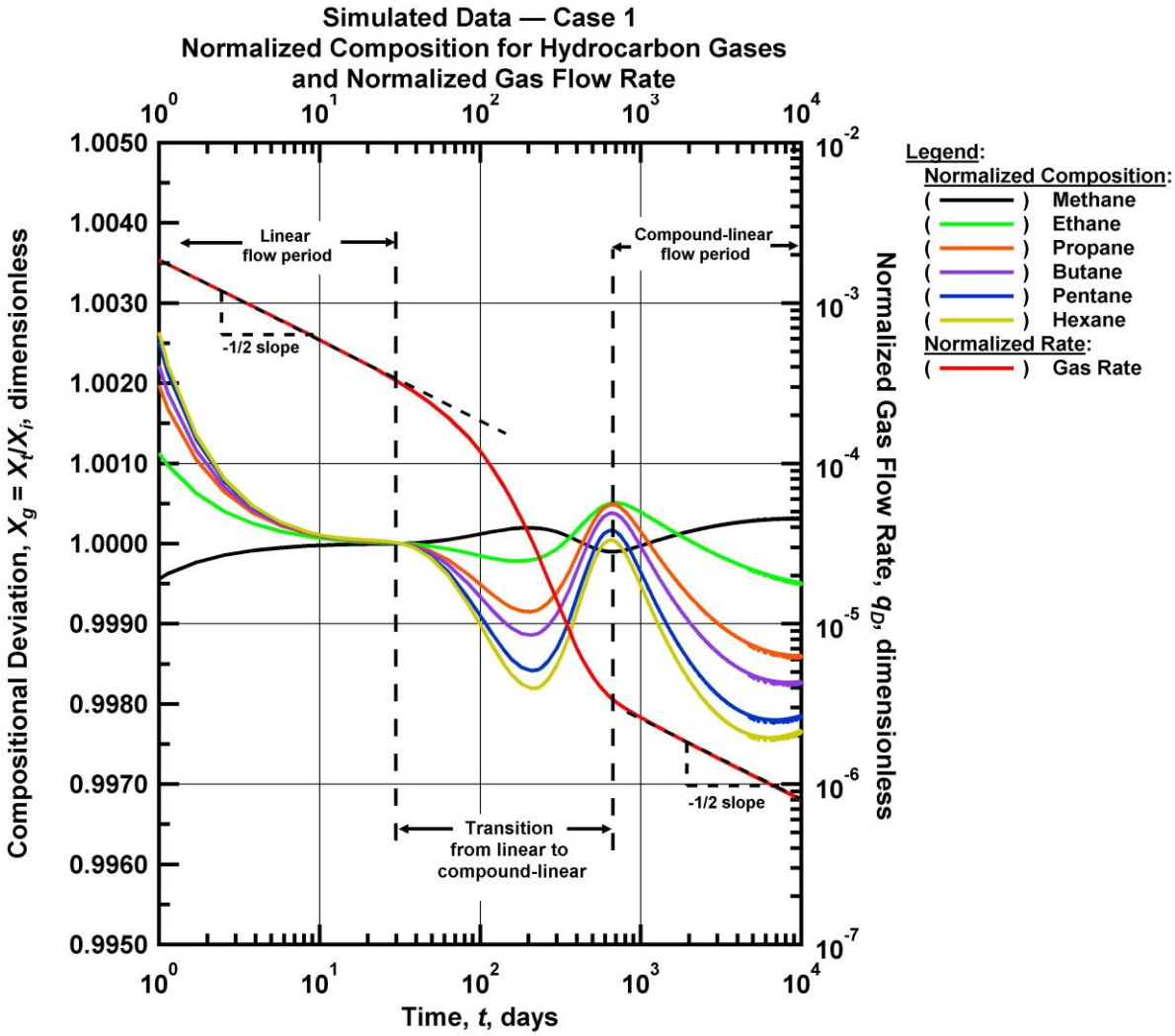

Figure 4.18 — Results of numerical simulation Case 1. Normalized compositions and normalized gas flow rate versus time. Figure demonstrates that compositional fluctuation peaks and troughs coincide with the transforming flow regimes.

Plots of absolute composition versus time for shale gas wells usually do not show any interesting behavior because the trends tend to be relatively subtle. Plotting the compositional *deviation* instead of the absolute composition, defined as the composition at time t divided by the *in situ* composition, yields much more informative trends.

$$X = \frac{x_t}{x_i} \quad \text{.....(4.1)}$$

All compositional deviation trends tend to start at a value of 1.0 because the first gas that is produced is relatively unaffected by desorption.

For Case 1, as shown in Figure 4.18, first note that the rate-time behavior exhibits a clear signature showing distinctly the linear, transitional, and compound-linear flow periods for the multiply-fractured horizontal well. Because this is simulated data, we know exactly what flow effects are causing the fluctuations in produced gas composition. In this case, we observe the following relationships: during transient linear flow, the normalized composition of the heavier components is decreasing and flattening. At the onset of the transition period, at the instant the fracture transient reaches the adjacent transient, the normalized compositions of the heavier components begin to decline once again. During the transition to the second linear flow period, the compound-linear flow period, the normalized compositions of the heavier compounds begin to swing upward. At the end of the transition period and the onset of fully-developed compound-linear flow the compositions of the heavier compounds have reached a new local maximum point and begin to decline again.

Thus, for Case 1, Figure 4.18 indicates that for the given flow geometry for the Langmuir isotherm parameters listed in Table 4.2, the compositional shift behavior of the heavier compounds exhibits a general signature of decreasing, then a temporarily increasing period, followed by a long declining tail. The start of the sharper decline at t=30 days coincides with the onset of fracture interference. The local peak in composition at t=600 days coincides with the end of the transition flow period. The compositional signature thus serves as a qualitative corroboration of the flow regime signature present in the rate-time data.

Table 4.3 — Langmuir and initial composition parameters used in Case 2.

Component	Y_i,	b_i, 1/psi	V_{Li}, scf/ton
Methane	0.80	$2.08\text{x}10^{-5}$	$6.9\text{x}10^{1}$
Ethane	0.07	$2.11\text{x}10^{-4}$	$2.59\text{x}10^{2}$
Propane	0.05	$7.02\text{x}10^{-4}$	$5.69\text{x}10^{2}$
Butane	0.05	$3.84\text{x}10^{-3}$	$2.00\text{x}10^{2}$
Pentane	0.02	$8.10\text{x}10^{-3}$	$4.03\text{x}10^{2}$
Hexane	0.01	$1.21\text{x}10^{-2}$	$7.41\text{x}10^{2}$

The Langmuir parameters in Table 4.3 correspond more closely with experimental data from the core samples obtained from these wells. The curves resulting from these parameters are visualized for the single-component Langmuir isotherm in Figure 4.19 and for the multicomponent Langmuir isotherm in Figure 4.20. Directly applying Langmuir parameters obtained from core experiments is problematic, as mentioned in the discussion of Case 1. The reason for this is that desorption experiments are typically primarily concerned with the absolute sorptivity of the individual gas species in isolation. In the reservoir, the factor which controls differential desorption is the relative sorptivity of each of the species as a

function of the composition of the other species. Therefore, the Langmuir parameters obtained from experiment should not be naively applied within the multicomponent Langmuir model.

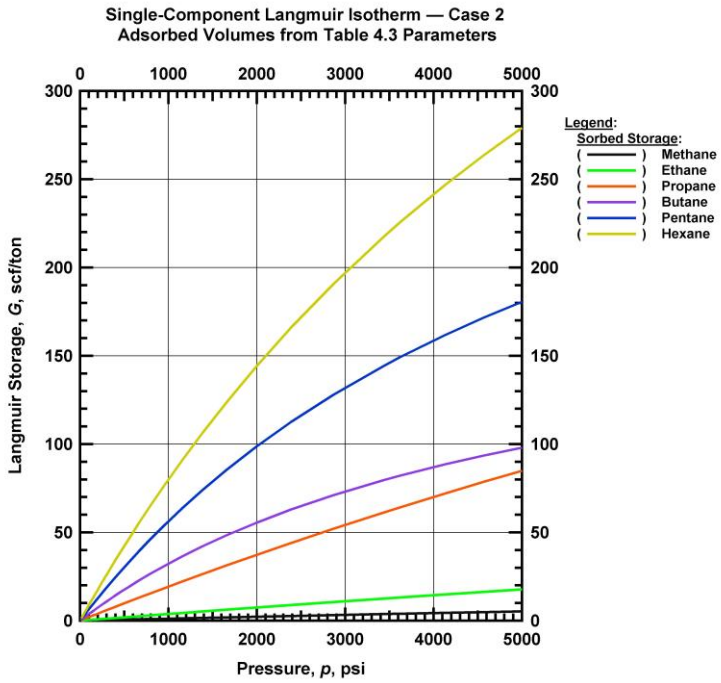

Figure 4.19 — Single-component Langmuir storage for methane through hexane versus p. Plot of Langmuir isotherm parameters used in Case 2 using Eq. 2.5.

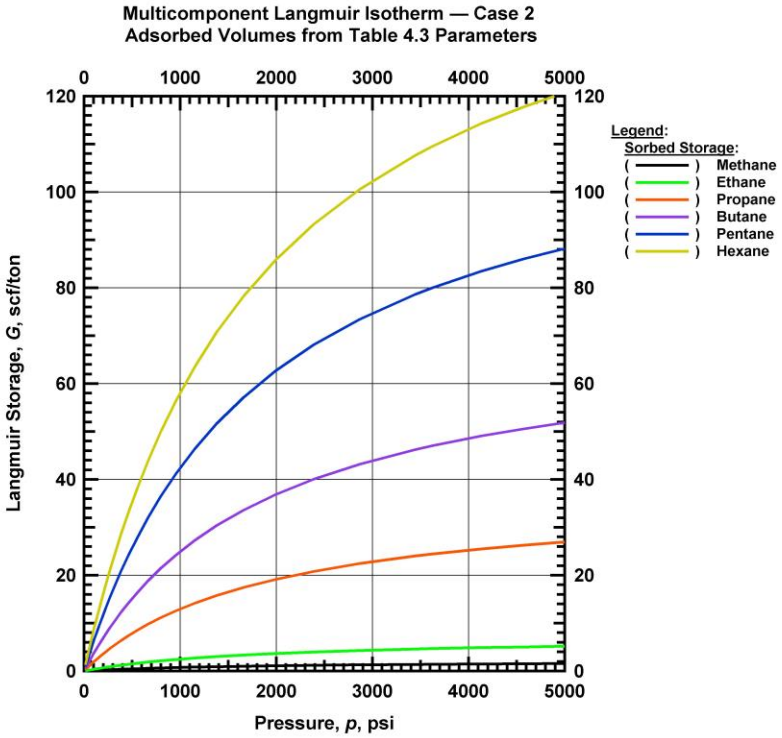

Figure 4.20 — Multi-component Langmuir storage for methane through hexane versus p. Plot of Langmuir isotherm parameters used in Case 2 using Eq. 2.5.

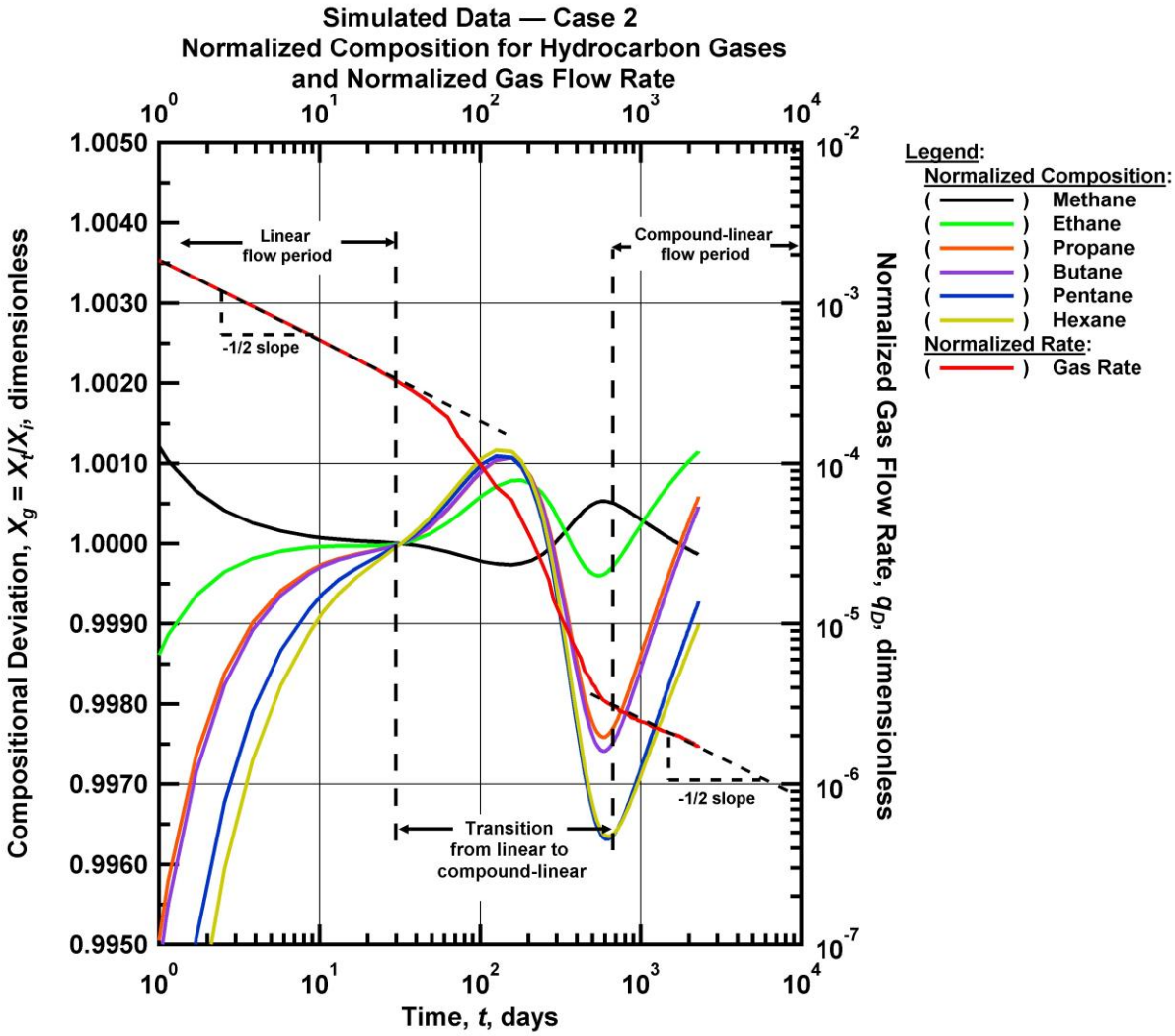

Figure 4.21 — Results of numerical simulation Case 2. Normalized compositions and normalized gas flow rate versus time. Using more typical Langmuir parameters, inflections in composition still coincide with changes in the flow regime, but the trend is inverted compared to Figure 4.18.

For the sake of completeness, we show in Figure 4.21 the consequences of using the parameters from Table 4.3 in the numerical model described in Table 4.4. Note that the compositional deviation trends are generally similar to those in Figure 4.18 except inverted, mirrored across the compositional deviation value $X = 1$.

4.4.2 Exploration of the Space of Sorption Parameters

In the previous section we took the approach of attempting to approximately match the performance of real North American shale gas wells by our selection of sorption model parameters. Here we take a

different approach; we seek to explore the variety of compositional trends versus time which can be realized by making a broad range of assumptions for the initial extended Langmuir parameters. In so doing, we hope to describe a range of hypothetical behaviors which may ultimately be witnessed in the field.

This approach of characterizing the parameter space through a thorough sensitivity study follows from the strategy used in our previous work regarding shale gas and tight gas completions and reservoir parameters.

We begin by generating a numerical model which approximates the estimated reservoir parameters of a typical well in the North American shale gas play examined in the field data analysis. The pertinent reservoir and completion parameters are contained in Table 4.4.

Table 4.4 — Reservoir and well system parameters used in numerical simulations.

Parameters	SI Unit	Field Unit
Fracture half-length, x_f	100 m	328.1 ft
Fracture conductivity, Fc_D	6.0×10^{-14} m^3	200 md-ft
Fracture spacing, d_f	20 m	65.6 ft
Reservoir thickness, h	100 m	328.1 ft
Matrix porosity, ϕ	10.0 percent	10.0
Temperature, T	200.0 ^{0}C	392 ^{0}F
Well radius, r_w	0.1 m	0.32 ft
Reservoir pressure, p_i	1.0×10^7 Pa	1450 psia
Well pressure, p_{wf}	5.0×10^6 Pa	725 psia

The *in situ* gas compositions used in all cases are shown in Table 4.6. Langmuir parameters computed from core analysis were not consistent because the available Langmuir desorption analyses were performed using individual gases.

In the cases where gas mixtures were used, the composition of the desorbing gas was not measured over time. Therefore, accurate multicomponent Langmuir parameters were unavailable, and we were forced to invent a set of parameters which result in the correct functional behavior within the required range of reservoir pressures. Furthermore, while in Section 4.4 we model the desorption of six components, we observe that the relative behavior of the heaviest component compared to the lightest component is of more relevant interest than the absolute behavior of several components. Therefore, we constrain our analysis to the three lightest alkanes.

Table 4.5 — Langmuir parameters and matrix permeability values used in all sensitivity runs.

Case	Matrix Permeability, m^2	Component	b_i, 1/Pa	V_{Li}, kg/kg rock
1	$3.0x10^{-19}$	Methane	$3.0x10^{-2}$	$12.0x10^{-9}$
		Ethane	$3.0x10^{-2}$	$15.0x10^{-9}$
		Propane	$3.0x10^{-2}$	$19.0x10^{-9}$
2	$3.0x10^{-19}$	Methane	$3.0x10^{-2}$	$20.0x10^{-9}$
		Ethane	$3.0x10^{-2}$	$30.0x10^{-9}$
		Propane	$3.0x10^{-2}$	$40.0x10^{-9}$
3	$3.0x10^{-19}$	Methane	$3.0x10^{-2}$	$20.0x10^{-9}$
		Ethane	$3.0x10^{-2}$	$16.0x10^{-9}$
		Propane	$3.0x10^{-2}$	$10.0x10^{-9}$
4	$3.0x10^{-19}$	Methane	$1.5x10^{-2}$	$12.0x10^{-8}$
		Ethane	$1.5x10^{-2}$	$15.0x10^{-8}$
		Propane	$1.5x10^{-2}$	$19.0x10^{-8}$
5	$3.0x10^{-19}$	Methane	$4.5x10^{-2}$	$12.0x10^{-10}$
		Ethane	$4.5x10^{-2}$	$15.0x10^{-10}$
		Propane	$4.5x10^{-2}$	$19.0x10^{-10}$
6	$3.0x10^{-19}$	Methane	$3.0x10^{-2}$	$8.0x10^{-9}$
		Ethane	$3.0x10^{-2}$	$10.0x10^{-9}$
		Propane	$3.0x10^{-2}$	$16.0x10^{-9}$
7	$3.0x10^{-18}$	Methane	$3.0x10^{-2}$	$12.0x10^{-9}$
		Ethane	$3.0x10^{-2}$	$15.0x10^{-9}$
		Propane	$3.0x10^{-2}$	$19.0x10^{-9}$
8	$3.0x10^{-18}$	Methane	$3.0x10^{-2}$	$20.0x10^{-9}$
		Ethane	$3.0x10^{-2}$	$30.0x10^{-9}$
		Propane	$3.0x10^{-2}$	$40.0x10^{-9}$
9	$3.0x10^{-18}$	Methane	$3.0x10^{-2}$	$20.0x10^{-9}$
		Ethane	$3.0x10^{-2}$	$16.0x10^{-9}$
		Propane	$3.0x10^{-2}$	$10.0x10^{-9}$
10	$3.0x10^{-18}$	Methane	$1.5x10^{-2}$	$12.0x10^{-8}$
		Ethane	$1.5x10^{-2}$	$15.0x10^{-8}$
		Propane	$1.5x10^{-2}$	$19.0x10^{-8}$
11	$3.0x10^{-18}$	Methane	$4.5x10^{-2}$	$12.0x10^{-10}$
		Ethane	$4.5x10^{-2}$	$15.0x10^{-10}$
		Propane	$4.5x10^{-2}$	$19.0x10^{-10}$
12	$3.0x10^{-18}$	Methane	$3.0x10^{-2}$	$8.0x10^{-9}$
		Ethane	$3.0x10^{-2}$	$10.0x10^{-9}$
		Propane	$3.0x10^{-2}$	$16.0x10^{-9}$

Table 4.6 — Initial composition parameters used in all cases.

Component	Y_i,
Methane	0.70
Ethane	0.20
Propane	0.10

The intent of the sorption parameters selected for Case 1 described in Table 4.5 was to generate behavior consistent with that observed in Section 4.3 in North American shale gas wells. The key criterion in selecting these particular b and V_L parameters was to cause the slope of the Langmuir isotherm curve to be relatively steep through the pressure interval of the reservoir system. This choice is consistent with the reports by some investigators that the sorptive behavior of shale can be accurately modeled with a Freundlich isotherm, because the steep region of the extended Langmuir model behaves very similarly to the Freundlich model.

Note that Case 1 and Case 7 are identical in properties except that the permeability in Case 7 is ten times higher. As shown in Figure 4.22, the flowing gas in Case 1 is undergoing a richening trend, as the relative composition of propane increases over time and the relative composition of methane diminishes. The compositions fluctuate over the course of the flowing time, with the composition of the heavier components reaching a local maximum at around 20 days. The maximum compositional deviation of propane for this case is roughly 5% greater than the *in situ* composition.

Having established the rationale for choosing the parameters used in Case 1, the parameters in Cases 2 are designed to merely show the effect of changing the sorptive storage (V_L) parameters to higher values. The overall character of the compositional trends in Case 2 as shown in Figure 4.23 is very similar to that of Case 1, except the maximum compositional deviation of propane in Case 2 is approximately 9%.

However, the compositional trend in Case 3, depicted in Figure 4.24 is significantly different from Case 1. In fact the compositional deviation trend is inverted, depicting a gradual gas leaning trend as the relative composition of methane increases rather than a richening trend. This is because, for Case 3, the V_L the parameter is largest for methane and smallest for propane, inverting the trend of the previous two cases. While theory suggests that the most significantly condensing alkanes should be the heavier ones, the purpose of Case 3 is to examine the consequences where the lighter compounds sorb more strongly than the heavier ones. We observe that these results most accurately reflect the observed flowing compositional behavior observed in actual North American shale gas wells discussed in Section 4.3. In other words, the assumption which most closely represents is the case in which the Langmuir volume for methane is highest.

The parameters in Case 4 are identical to those in Case 1 except the b term for each gas is lower (half the value of that in Case 1.) The overall compositional deviation trend in Case 4, as shown in Figure 4.25, is

very similar to that in Case 1, with the maximum relative deviation of the propane composition being approximately 4%, greater than the *in situ* composition, which is less pronounced than in Case 1.

Again the parameters in Case 5 are identical to those in Case 1 and Case 4 except the *b* term for each gas is higher, 50% higher than the value in Case 1. Here we note that the compositional fluctuation behavior, shown in Figure 4.26, is actually significantly different from the other two cases. First, the local maximum of the relative composition of propane occurs at an earlier point in time (around 10 days, compared with a peak at around 20 days in Case 1) and second, the later-time inflection of propane composition is sharper. Also, after 200 days, the maximum deviation of propane composition is only around 2% above the *in situ* composition.

The V_L parameters in Case 6 are selected to be lower than those in Case 1, such that comparing Case 1, Case 2 and Case 6 (Figures 4.22, 4.23, and 4.27, respectively) shows the impact of increasing the sorptive storage for each component. The maximum relative compositional deviation for propane in this case is roughly 8% above the *in situ* composition.

The trends in Cases 7 through 12 (shown in Figures 4.28 through 4.33) are significantly different from those in Cases 1 through 6, which is remarkable because the only parameter which distinguishes Case 1 from Case 7, or Case 2 from Case 8 (etc.) is the matrix permeability. The matrix permeability of Cases 7 through 12 is 3.0×10^{-18} m^2. The fluctuations in composition are much less nuanced in the latter six cases. None of these cases possess a local peak in composition; instead they depict gradual, nearly monotonic trends.

In Case 7, depicted in Figure 4.28, the maximum relative compositional deviation for propane is approximately 8%, greater than the maximum deviation of 5% observed in Case 1.

For Case 8, shown in Figure 4.29, the maximum relative compositional deviation for propane is approximately 11%, greater than the maximum of 9% observed in Case 2.

In Case 9 (Figure 4.30), as in Case 3, the trend is inverted, with the compositional deviation of methane increasing over time, depicting a gas leaning trend. In this case the maximum deviation for propane is 10% below the *in situ* composition.

For Case 10, shown in Figure 4.31, the maximum relative compositional deviation for propane is approximately 5%, greater than the observed deviation of 4% for Case 4.

For Case 11, the results of which are shown in Figure 4.32, the maximum relative compositional deviation for propane is approximately 3%, with the composition of each component appearing to flatten out at the end of the simulated time. This is slightly higher than the 2% deviation observed in Case 5.

For Case 12 (Figure 4.33), the maximum relative compositional deviation for propane is approximately 12%, significantly greater than the 8% observed in Case 6.

In comparing the results of these twelve cases against the field data presented in we find that the cases which most closely match the field data in a qualitative sense are Cases 3 and 9. These are the two Cases for which the Langmuir storage parameter for methane is the highest and the parameter for propane the lowest. Case 3 (Figure 4.24) in particular exhibited the characteristic unstable fluctuation in composition present in the field data analyzed in Section 4.3. Since the results of this work are simulated cases, we know exactly how far the flow has progressed in these cases, and can verify that these fluctuations in composition occur too early to be the result of interference between adjacent fractures. The flow period of approximately 20 days required for the propane composition deviation to reach a local minimum and then begin to rise closely matches the similar 20 day local minimum observed in the Well C data.

However, the propane compositional deviation in the Case 3 data reaches its next local peak at about 30-40 days of flowing time, while the analogous peak observed in the Well C field data occurs after approximately 25 days of flowing time. It is very difficult to say concretely what this means, because of the many unknowns involved in the reservoir parameters for Well C. A broader set of data for measured flowing gas composition in shale gas wells may improve our ability to meaningfully compare field data to model results.

Local peaks and deviations from the general composition trend in these wells may indicate a transient effect such as the full pressure investigation of the hydraulic fracture or the near-well region. In the cases examined in this work, the transient compositional signatures appear to pass relatively rapidly, typically in less than twenty days, much faster than the time needed for the pressure transients of adjacent fractures to interfere. In other words, the fluctuations in composition do not appear to indicate the transition to the compound-linear flow regime. Therefore, it is likely that the transient represented in these wells is a fracture-system transient, not a reservoir-scale transient.

Broad and consistent collection of flowing gas composition data may yield more precise, quantitative reservoir performance diagnostics when combined with traditional production data analysis.

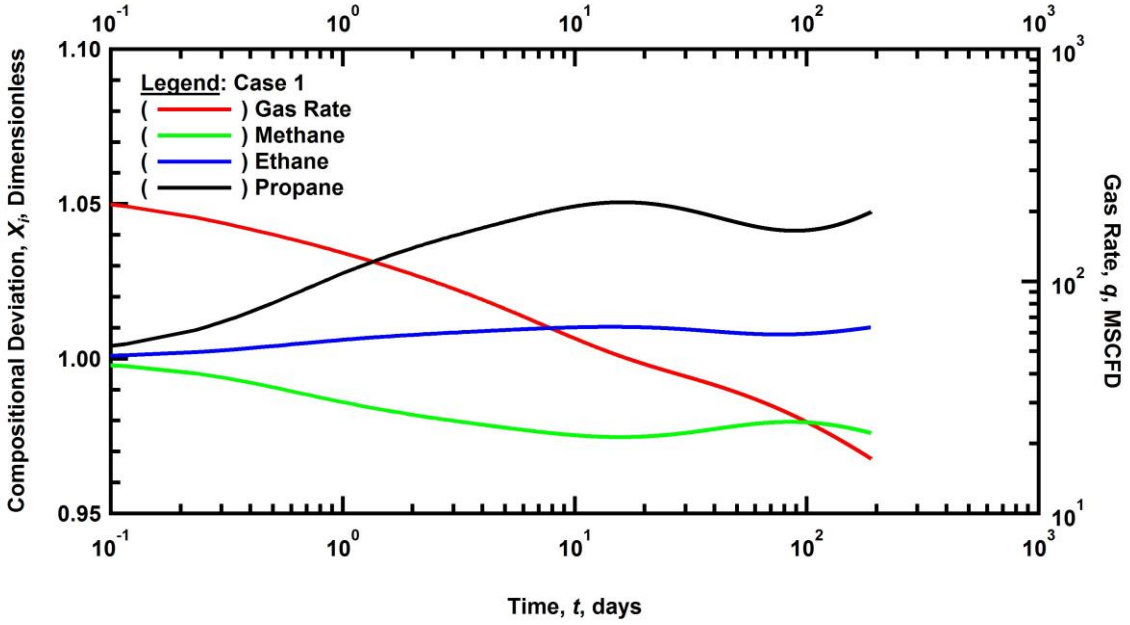

Figure 4.22 — Rate and compositional deviation versus time for simulation case 1.

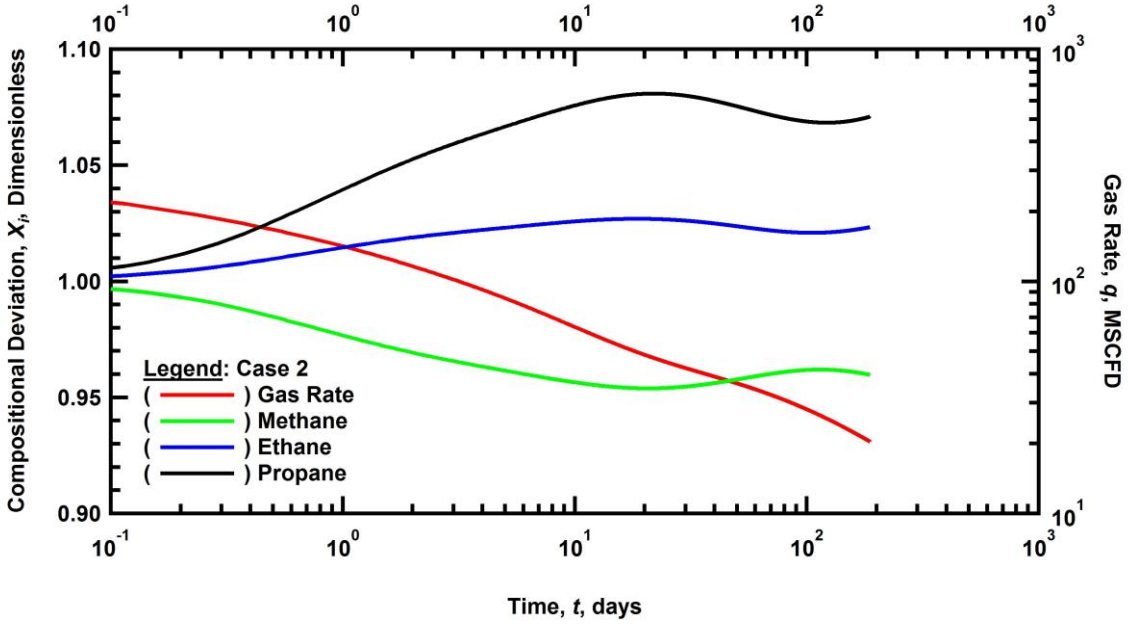

Figure 4.23 — Rate and compositional deviation versus time for simulation case 2.

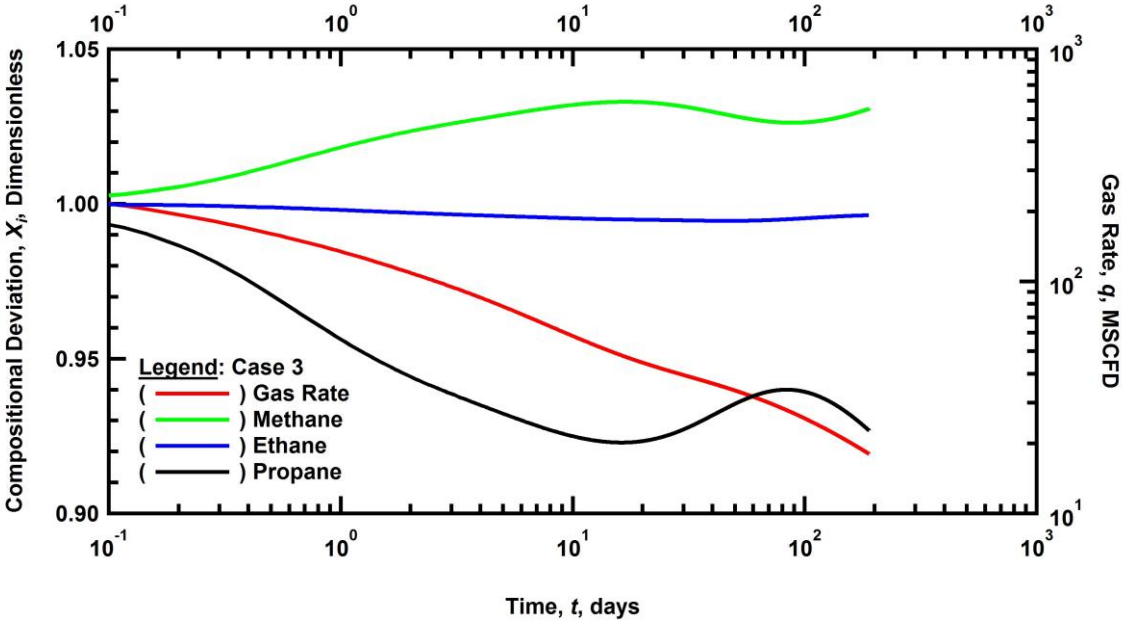

Figure 4.24 — Rate and compositional deviation versus time for simulation case 3.

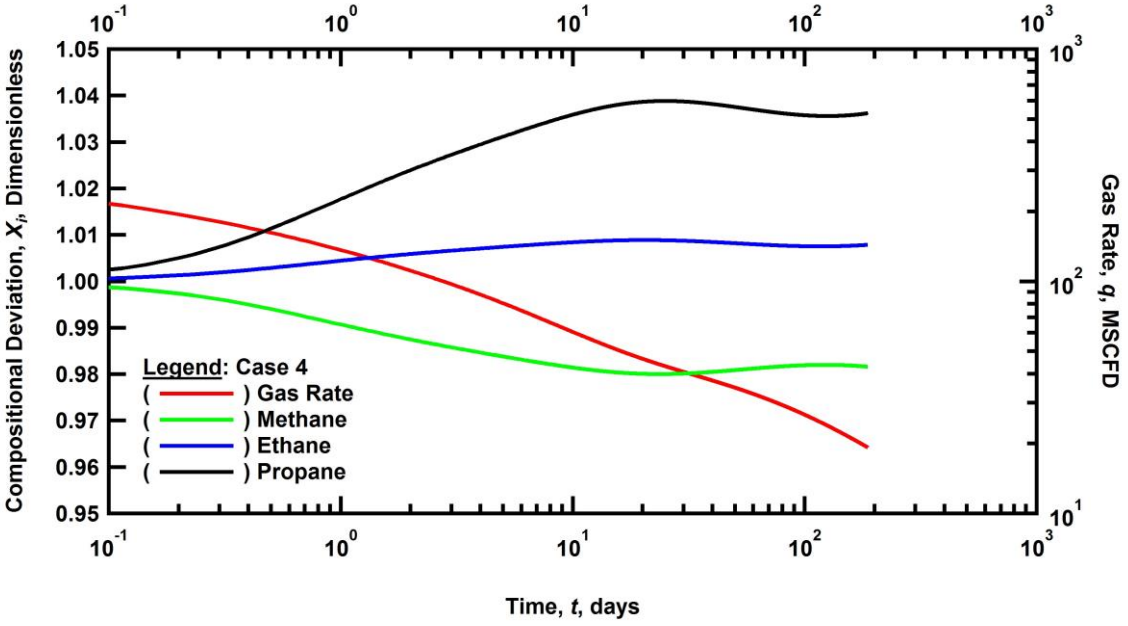

Figure 4.25 — Rate and compositional deviation versus time for simulation case 4.

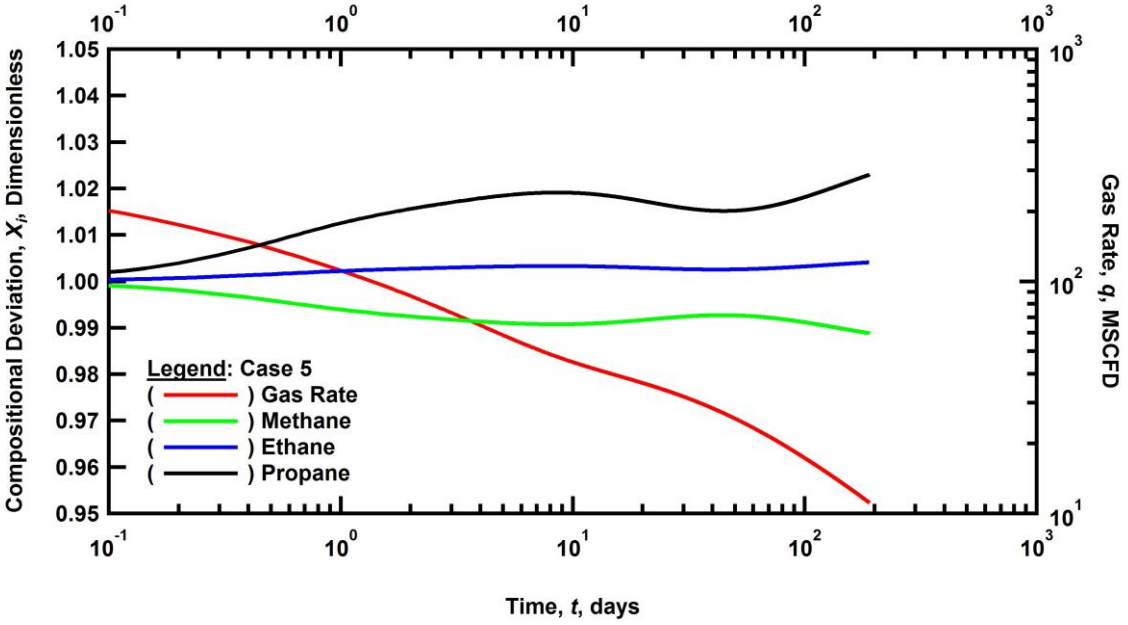

Figure 4.26 — Rate and compositional deviation versus time for simulation case 5.

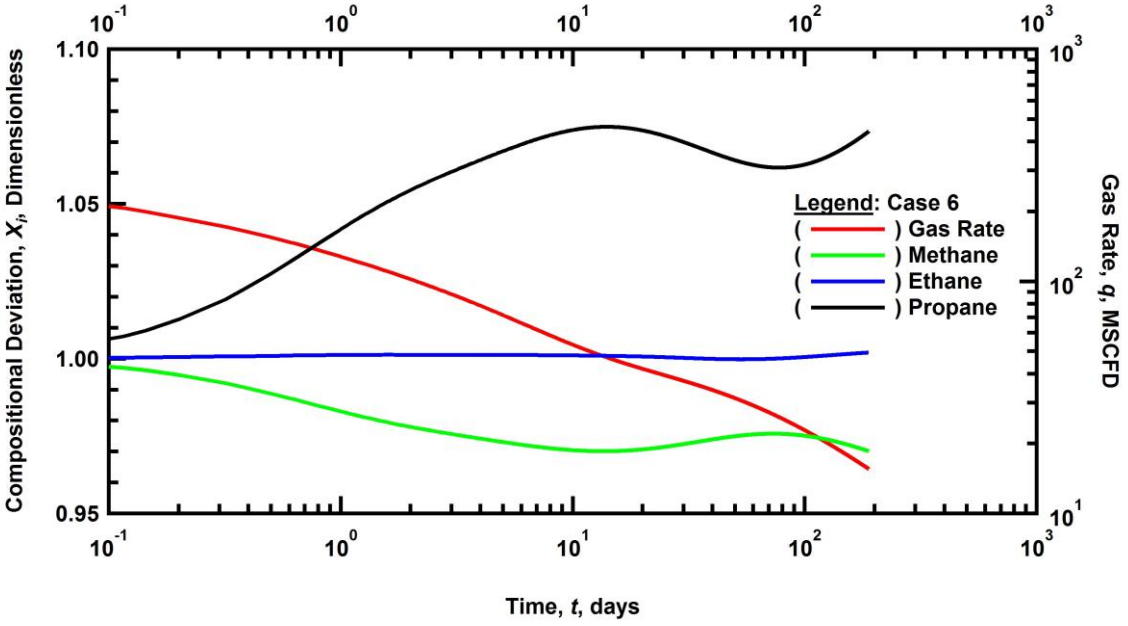

Figure 4.27 — Rate and compositional deviation versus time for simulation case 6.

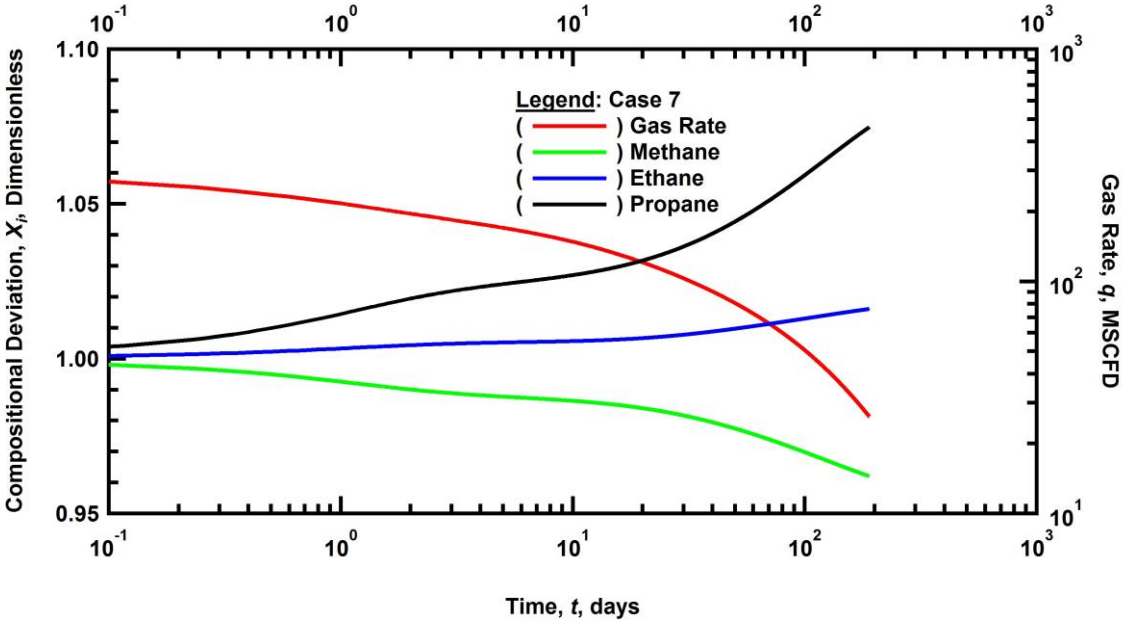

Figure 4.28 — Rate and compositional deviation versus time for simulation case 7.

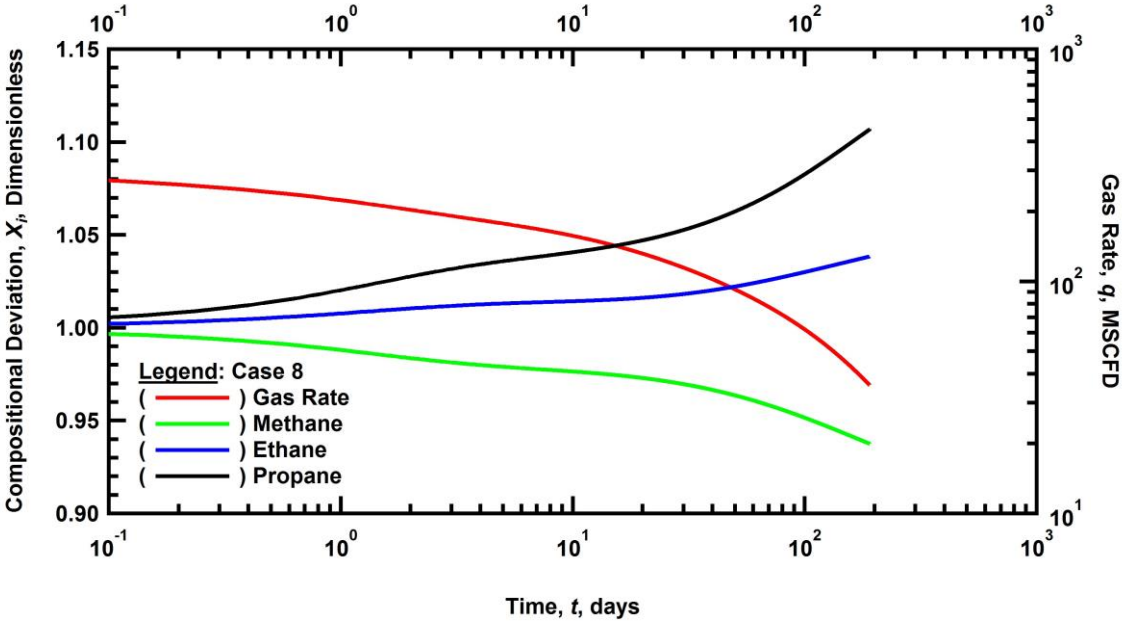

Figure 4.29 — Rate and compositional deviation versus time for simulation case 8.

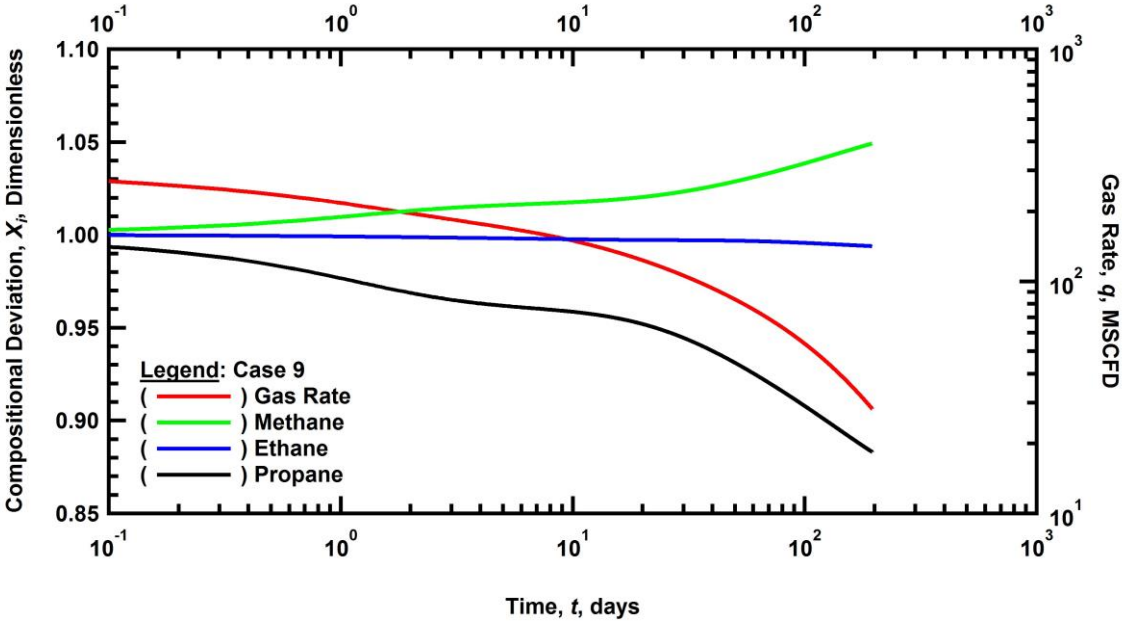

Figure 4.30 — Rate and compositional deviation versus time for simulation case 9.

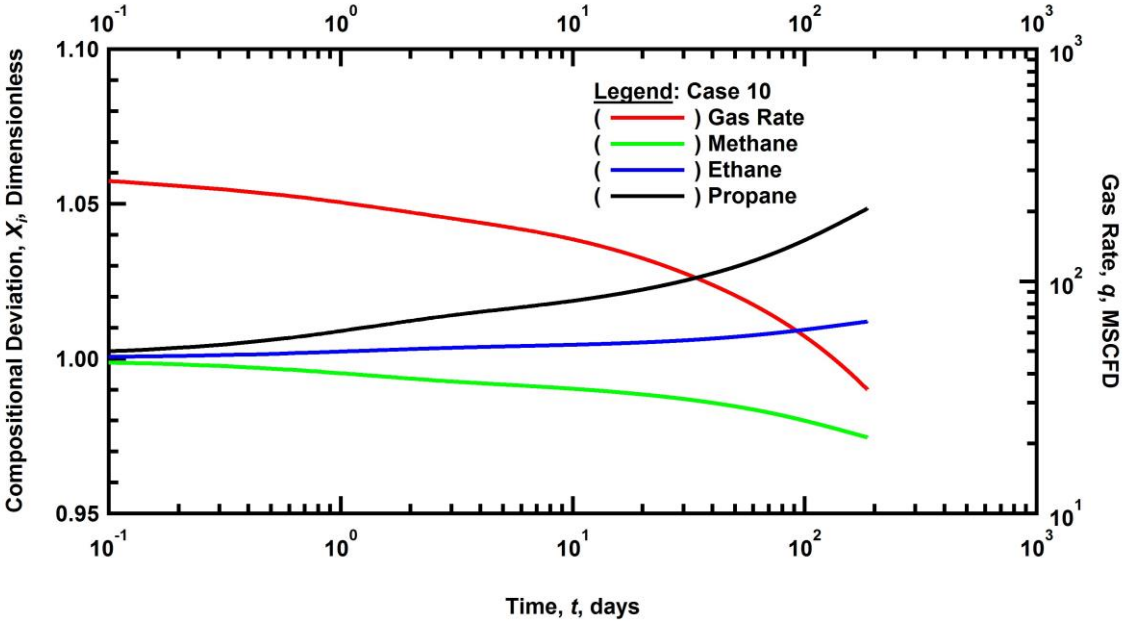

Figure 4.31 — Rate and compositional deviation versus time for simulation case 10.

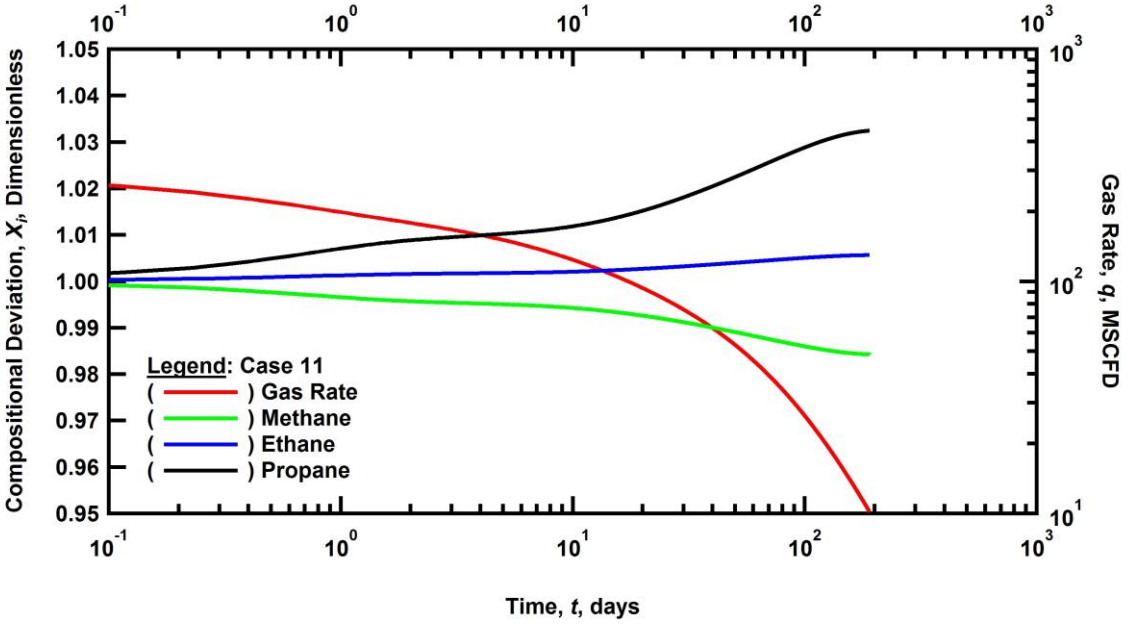

Figure 4.32 — Rate and compositional deviation versus time for simulation case 11.

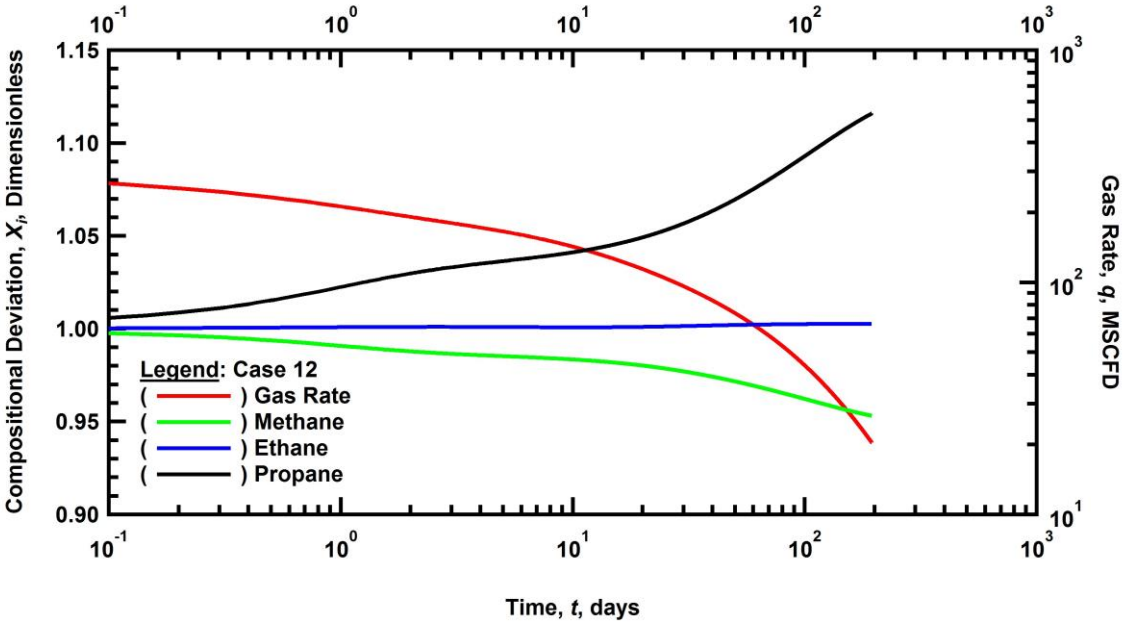

Figure 4.33 — Rate and compositional deviation versus time for simulation case 12.

4.5 Discussion of Compositional Change Results

We examine measured composition and isotopic data from producing wells in a North American shale gas play. We identify possible characteristic trends in this data and suggest interpretations of these trends. Through numerical modeling we offer support for these interpretations.

Local peaks and deviations from the general declining heavy component composition trend in these wells may indicate a transient effect such as the full pressure investigation of the hydraulic fracture, the fracture network, the near-well region, or even the extent of the producing flow unit. In the wells examined in this work, the transient compositional signatures appear to pass relatively rapidly, typically in less than fifty days. Interference between adjacent hydraulic fractures should take several years if the transient is passing through nanodarcy shale. Therefore, it is likely that the transient represented in these wells is a fracture-system transient, not a reservoir-scale transient.

Measuring both composition and isotopic ratio has proven useful. In the cases where either the composition data or the isotopic data does not provide a clear signature, generally the other source of data can be used alone. When both sources of data provide clear trends, the trends tend to possess coincident features such as simultaneous local minima, tending to reinforce a single interpretation. Broader collection of this type of data may yield more precise, quantitative reservoir performance diagnostics. Additionally, measurement of this type of data would need to be continued for years (or decades) to conclusively support an interpretation, because this is the amount of time that it will take for the pressure transient to interact with the productive reservoir volume.

Additionally, better measurement methodologies should be pursued. Ideally, measurements of composition and stable carbon isotope ratio would be made much more frequently, with more exhaustive compositional profiles, and the obtained fluid samples would not be vented down to 300 psi at the surface. A truly ideal situation would involve continuous downhole monitoring of fluid composition, but at this type of equipment needed to precisely measure fluid composition is too large, expensive, and fragile to be placed in the downhole environment.

There may also be cheaper, yet more robust measurement techniques which could provide further insight while still falling short of the ideal. For example, passive monitoring of stable carbon isotope ratio in the atmosphere near the wellhead should in principle detect the presence of the produced gas which continually leaks from the wellhead into the environment in minute quantities. These atmospheric measurements would be imprecise but might give a qualitative indication of the stable carbon isotope trend very cheaply and at very high measurement frequency.

NOMENCLATURE

Variables:

a = Empirical constant of Cooke (1973) model (dimensionless)
b = Empirical constant of Cooke (1973) model (dimensionless)
b = Constant of Extended Langmuir model, 1/Pa
b_R = Acentricity variable of Riazi and Whitson (1993) (dimensionless)
B = Formation volume factor, bbl/stb
B_i = Multicomponent Langmuir parameter, 1/Pa
b_K = Klinkenberg constant, Pa
c = Constant of Klinkenberg approximation, approximately 1 (dimensionless)
c_1 = Constant of rarefaction equation, 4.0 (dimensionless)
c_2 = Constant of rarefaction equation, 0.4 (dimensionless)
c_f = Formation compressibility, 1/psi
C_{fD} = Dimensionless fracture conductivity (dimensionless)
c_p = Pore compressibility, 1/psi
c_R = Acentricity variable of Riazi and Whitson (1993) (dimensionless)
c_t = Total compressibility, 1/psi
d_f = Fracture spacing, ft
$D_{G,i}$ = Diffusion coefficient of species i in the gas phase, m^2/s
D_V = Diffusion volume, cm^3
d_k = molecular kinetic diameter, m
E_1 = Error function (operator)
h = Reservoir thickness, ft
J = Diffusive molar flux, mol/m^2
k = Matrix permeability, md
k_0 = Initial matrix permeability, md
k_a = Apparent permeability to gas phase, md
k_B = Boltzmann's constant,$1.3806503 \times 10^{-23}$ m^2-kg/(s^2-K)
k_f = Fracture permeability, md
k_g = Permeability to gas phase, md
k_m = Matrix permeability, md
Kn = Knudsen number (dimensionless)
k_{rw} = Relative permeability to aqueous phase (dimensionless)
k_w = Intrinsic permeability to aqueous phase, md
k_∞ = Intrinsic permeability or permeability at infinite pressure, md
l_{char} = Characteristic feature length (pore or capillary radius), cm
L_w = Horizontal well length, ft
M = Molecular mass, g/mol

N_A = Avogadro's number, 6.02×10^{23} molecules

n_v = Moles of gas per unit volume, mol/m^3

p = Pressure, psi

p_c = Critical pressure, Pa

P_{cmax} = Maximum capillary pressure of van Genuchten, kPa

p_D = Dimensionless pressure (dimensionless)

p_0 = Pressure parameter of van Genuchten, kPa

p_i = Initial reservoir pressure, psi

p_r = Pressure at point r in reservoir, psi

p_{wf} = Wellbore flowing pressure, psi

p_L = Langmuir pressure, psi

q = Rate, bbl/day or mscf/day

q_{Dd} = Dimensionless rate derivative (dimensionless)

q_{Ddi} = Dimensionless rate integral (dimensionless)

q_{Ddid} = Dimensionless rate integral derivative (dimensionless)

r = Radius, ft

r_D = Dimensionless radius (dimensionless)

r_{pore} = Pore throat radius (cm)

r_w = Wellbore radius, ft

R = Ideal gas constant, 8.314 J/K-mol

S_w = Water phase saturation, fraction

S_G = Gas phase saturation, fraction

S_{airr} = Irreducible aqueous saturation of Corey et al.[8], fraction

S_{girr} = Gas phase saturation, fraction

S_{wi} = Initial water saturation, fraction

t = Time, days or seconds

T = Temperature, K

t_D = Dimensionless time (dimensionless)

t_{Dd} = Dimensionless time derivative (dimensionless)

v = Flow velocity, m/s

$\bar{v}$ = Average velocity, m/s

$\overline{v_{rel}}$ = Relative molecular velocity, m/s

$\vec{v}$ = Molecular velocity vector, m/s

$\vec{v}_{rel}$ = Relative molecular velocity vector, m/s

V_L = Langmuir volume, scf/ton

w = Fracture width, ft

x = Distance from production source, m

x_f = Fracture half-length, ft

$X_{G,i}$ = Mass fraction of species *i* in the gas phase, fraction

y = Mole fraction, fraction

Greek Symbols:

α = Rarefaction parameter (dimensionless)

α_0 = Constant of rarefaction equation, $64/15\pi$ (dimensionless)

β = Forchheimer nonlinear flow parameter, 1/ft, 1/cm or 1/m

ϕ = Porosity, fraction

τ = Variable of integration (dimensionless)

τ_G = Tortuosity (dimensionless)

ϕ_0 = Initial porosity, fraction

ρ = Density, kg/m^3

ρ_G = Gas phase density, kg/m^3

δ = Constrictivity (dimensionless)

$\bar{\lambda}$ = Mean free path, m

λ = Parameter of van Genuchten[7] (dimensionless)

μ = Viscosity, cP

θ = Langmuir storage, scf/ton

ω = Acentric factor of Riazi and Whitson (1993) (dimensionless)

Ω_{AB} = Collision integral of Chapman-Enskog (dimensionless)

Subscripts:

i = Index of the *i*-th component.

j = Index of the *j*-th component.

a = Component of interest in a binary mixture

b = Second component in a binary mixture

G = Gas phase

CH4 = Methane component.

CO2 = Carbon dioxide component.

H2O = Water component.

H = Property reflects desired high pressure conditions.

L = Property reflects low reference-point pressure conditions.

Superscripts:

HiP = Indicates high pressure.

LoP = Indicates low pressure.

REFERENCES

Akkutlu, I.Y., and Fathi, E. 2011. Gas Transport in Shales with Local Kerogen Heterogeneities. Paper SPE 146422 presented at the SPE Annual Technical Conference and Exhibition held in Denver, Colorado, 30 October-2 November.

Ambrose, R.J., Hartman, R.C., and Akkutlu, I.Y. 2011. Multi-component Sorbed Phase Considerations for Shale Gas-in-Place Calculations. Paper SPE 141416 presented at the SPE Production and Operations Symposium held in Oklahoma City, Oklahoma, 27-29 March.

Bartenhagen, K. Wireline Evaluation Techniques of Shale Gas Reservoirs: http://www.rpsea.org/forums/shale_bartenhagen.pdf. Downloaded 01 December 2007.

Bird, R.B., Stewart, W.E., and Lightfoot, E.N. 2007. *Transport Phenomena*. New York: John Wiley & Sons, Inc.

Brunauer, S., Emmett, P.H. and Teller, E. 1938. Adsorption of Gases in Multimolecular Layers. *J. Am. Chem. Soc.* **60** (2) 309-319. doi:10.1021/ja01269a023

Bustin, R.M., Bustin, A.M.M., Cui, X., and Ross, D.J.K. 2008. Impact of Shale Properties on Pore Structure and Storage Characteristics. Paper SPE 119892 presented at the SPE Shale Gas Production Conference held in Fort Worth, Texas, 16-18 November.

Chapman, S.J. 2008. *Fortran 95/2003 for Scientists and Engineers*. Boston. McGraw-Hill.

Chung, T.H., Ajlan, M., Lee, L.L., and Starling, K.E. 1988. Generalized Multiparameter Correlation for Nonpolar and Polar Fluid Transport-Properties. *Industrial & Engineering Chemistry Research* **27** (4): 671-679. DOI: 10.1021/ie00076a024.

Civan, F. 2008. Effective Correlation of Apparent Gas Permeability in Tight Porous Media. *Transp. in Porous Med.* DOI: 10.1007/s11242-009-9432-z

Clarkson, C.R. and Bustin, R.M. 1999. Binary gas adsorption/desorption isotherms: effect of moister and coal composition upon carbon dioxide selectivity over methane. *International Journal of Coal Geology*. **42** (2000): 241-271.

Clarkson, C.R., Jensen, J.L., and Blasingame, T.A. 2011. Reservoir Engineering for Unconventional Gas Reservoirs: What Do We Have to Consider? Paper SPE 145080 presented at SPE North American Unconventional Gas Conference and Exhibition held in The Woodlands, Texas, 14-16 June.

Corey, A.T. 1957. Measurement of water and air permeability in unsaturated soil. *Soil Sci. Soc. Am. Proc.* **21**:7-10.

Dake, L.P. 1978. *Fundamentals of Reservoir Engineering.* New York: Elsevier.

Do, D.D. 1998. *Adsorption Analysis: Equilibria and Kinetics*. London: Imperial College Press.

Doronin, G.G. and Larkin, N.A. 2004. On dusty gas model governed by the Kuramoto-Sivashinsky equation. *Computational and Applied Mathematics.* **23** (1): 67-80.

Evans, R., Marconi, U.M.B., and Tarazona, P. 1986. Capillary condensation and adsorption in cylindrical and slit-like pores. *J. Chem. Soc., Faraday Trans.* **2** 82 1763-1787.

Faraj, B., Williams, H., Addison, G., et al. 2004. Gas Potential of Selected Shale Formations in the Western Canadian Sedimentary Basin," *Gas TIPS* **10** (1): 21-25.

Fathi, E., and Akkutlu, I.Y. 2011. Mass Transport of Adsorbed-Phase in Stochastic Porous Medium with Fluctuating Porosity Field and Nonlinear Gas Adsorption Kinetics. *Transp. Porous Med.* DOI: 10.1007/s11242-011-9830-x

Forchheimer, P. 1901. Wasserbewewegung durch Boden. *ZVDI* **45**, 1781.

Forgotson, J. M. Distribution and Properties of Shale Gas in the Arkoma Basin. http://www.rpsea.org/forums/shale_forgotson.pdf. Downloaded 01 December 2007.

Frantz, J.H. and Jochen, V. Shale Gas. http://www.slb.com/media/services/stimulation/fracturing/shale_gas_white_paper.pdf. Downloaded 01 December 2007.

Frederick Jr., D.C. and Graves, R.M. 1994. New Correlations To Prediction Non-Darcy Flow Coefficients at Immobile and Mobile Water Saturation. Paper SPE 28451 presented at the 1994 SPE Annual Technical Conference and Exhibition, New Orleans, Sept. 25-28.

Freeman, C.M., Boyle, K.L., Reagan, M., Johnson, J., Rycroft, C., and Moridis, G.J. 2013. MeshVoro: A Three-Dimensional Voronoi Mesh Building Tool for the TOUGH Family of Codes. Computers and Geosciences (under review).

Freeman, C.M., Ilk, D., Moridis, G.J., and Blasingame, T.A. 2009. A Numerical Study of Tight Gas and Shale Gas Reservoir Systems. SPE paper 124961 presented at the SPE Annual Technical Conference and Exhibition held in New Orleans, Louisiana, 4-9 October.

Freeman, C.M. 2010. A Numerical Study of Microscale Flow Behavior in Tight Gas and Shale Gas Reservoir Systems. 2010. SPE International Student Paper Contest entry, paper 141125-STU presented at the SPE Annual Technical Conference and Exhibition held in Florence, Italy, September 19-22.

Freeman, C.M. 2010. Study of Flow Regimes in Multiply-Fractured Horizontal Wells in Tight Gas and Shale Gas Reservoir Systems, MS Thesis, Texas A&M U. College Station, TX.

Freeman, C.M., Moridis, G.J., and Blasingame, T.A. 2011. A Numerical Study of Microscale Flow Behavior in Tight Gas and Shale Gas Reservoir Systems. *Transp. in Porous Med.* **90** (1): 253-268. doi:10.1007/s11242-011-9761-6

Freeman, C.M., Moridis, G.J., Ilk, D., and Blasingame, T.A. 2010. A Numerical Study of Transport and Storage Effects for Tight Gas and Shale Gas Reservoir Systems. SPE paper 131583 presented at the SPE International Oil & Gas Conference and Exhibition held in Beijing, China, June 8-10.

Fuller, E.N., Ensley, K., and Giddings, J.C.: Diffusion of halogenated hydrocarbons in helium. The effect of structure on collision cross sections. J. Phys. Chem., 73: 3679 (1969).

Hill, D.G., and Nelson, C.R. 2000. Gas Productive Fractured Shales: An Overview and Update. *Gas TIPS* **6** (3): 4-13.

Ilk, D., Rushing, J.A., and Blasingame, T.A. 2011. Integration of Production Analysis and Rate-Time Analysis via Parametric Correlations - Theoretical Considerations and Practical Applications. Paper SPE 140556 presented at the SPE Hydraulic Fracturing Conference and Exhibition held in The Woodlands, Texas, 24-26 January.

Javadpour, F., Fisher, D., and Unsworth, M. 2007. Nanoscale Gas Flow in Shale Gas Sediments. *JCPT*. **46** (10): 55-61.

Klinkenberg, L.J. 1941. The Permeability of Porous Media to Liquid and Gases. 1941. Paper presented at the API 11th Mid Year Meeting, Tulsa, Oklahoma, May; in *API Drilling and Production Practice* (1941), 200-213

Kutasov, I.M. 1993. Equation Predicts Non-Darcy Flow Coefficient. *Oil & Gas Journal* (March 15, 1993) 66-67.

Langmuir, I. 1916. The constitution of fundamental properties of solids and liquids. *J. Am. Chem. Soc.* **38**, 2221-95.

Leahy-Dios, A., Das, M., Agarwal, A., and Kaminsky, R.D. 2011. Modeling of Transport Phenomena and Multicomponent Sorption for Shale Gas and Coalbed Methane in an Unstructured Grid Simulator. Paper SPE 149352 presented at the SPE Annual Technical Conference and Exhibition held in Denver, Colorado, 30 October-2 November.

Mattar, L., Gault, B., Morad, K., Clarkson, C.R., Freeman, C.M., Ilk, D., and Blasingame, T.A. 2008. Production Analysis and Forecasting of Shale Gas Reservoirs: Case History-Based Approach. SPE paper 119897 presented at the SPE Shale Gas Production Conference held in Fort Worth, Texas, 16-18 November.

Mayerhofer, M.J., Lolon, E.P., Warpinski, N.R., Cipolla, C.L., Walser, D., and Rightmire, C.M. 2008. What is Stimulated Reservoir Volume? Paper SPE 119890 presented at the SPE Shale Gas Production Conference held in Fort Worth, Texas, 16-18 November.

McCain, W.D. 1990. *The Properties of Petroleum Fluids*. Tulsa: PennWell Publishing Company, 83.

Moridis, G.J., Kuzma-Anderson, H., Reagan, M.T., Blasingame, T.A., Santos, R., Boyle, K.L., Freeman, C.M., Ilk, D., Yang, W., Cossio, M., Bhattacharya, S., Nikolaou, M. 2011. A Self-Teaching Expert System for the Analysis, Design and Prediction of Gas Production from Unconventional Gas Resources. Paper SPE 149485 presented at the Canadian Unconventional Resources Conference held in Alberta, Canada, 15-17 November.

Myers, A.L., and Prausnitz, J.M. 1965. Thermodynamics of mixed-gas adsorption. *AIChE J.* **11**: 121-7.

Nelson, R.A. 2001. *Geologic Analysis of Naturally Fractured Reservoirs*, 2nd Edition. Houston: Gulf Publishing Co. Book Division.

Passey, Q.R., Bohacs, K.M., Esch, W.L., Klimentidis, R., and Sinha, S. 2010. From Oil-Prone Source Rock to Gas-Producing Shale Reservoir - Geologic and Petrophysical Characterization of Unconventional Shale Gas Reservoirs. Paper SPE 131350 presented at the CPS/SPE International Oil & Gas Conference and Exhibition in China held in Beijing, China, 8-10 June.

Peng, DY, and Robinson, DB (1976). A New Two-Constant Equation of State. *Industrial and Engineering Chemistry: Fundamentals* **15**: 59–64. doi:10.1021/i160057a011

Powers, B. 2005. The Bright Future of Shale Gas. *US Energy Investor* (3): 1-7.

Pruess, K. and Narasimhan, T.N. 1985. A Practical Method for Modeling Fluid and Heat Flow in Fractured Porous Media. *SPEJ* (Feb.) 14-26.

Riazi, M.R., and Whitson, C.H.: Estimating diffusion coefficients of dense fluids. Ind. Eng. Chem. Res. 32, 3081 (1993).

Rycroft, C.H. 2009. Voro++: A three-dimensional Voronoi cell library in C++. *Chaos* **19** 041111.

Schettler, P.D., and Parmely, C.R. 1991. Contributions to Total Storage Capacity in Devonian Shales. SPE paper 23422 presented at the SPE Eastern Regional Meeting held in Lexington, Kentucky, 22-25 October.

Slattery, C.J. 1999. *Advanced Transport Phenomena.* Cambridge: Cambridge University Press, 1.

Sondergeld, C.H., Ambrose, R.J., Rai, C.S., and Moncrieff, J. 2010. Micro-Structural Studies of Gas Shales. Paper SPE 131771 presented at the SPE Unconventional Gas Conference held in Pittsburgh, Pennsylvania, 23-25 February.

Steinfeld, J.I., Francisco, J.S., and Hase, W.I. 1998. *Chemical Kinetics and Dynamics*. Prentice Hall, 228.

Strąpoć, D, Mastalerz, M., Schimmelmann, A., Drobniak, A., and Hedges, S. 2008. Variability of geochemical properties in a microbially dominated coalbed gas system from the eastern margin of the Illinois Basin, U.S.A. International Journal of Coal Geology 76 (1-2), 98-110.

TOUGH+ Numerical Simulator. 2008. Lawrence Berkeley National Laboratory, http://esd.lbl.gov/tough+/.

Tovbin, K.Y., Petukhov, A.G., and Eremich, D.V. 2005. Critical Temperature of Capillary Condensation in Narrow Cylindrical Pores. *Russian Journal of Physical Chemistry*. **80** (12): 2007-2015.

van Genuchten, M.T.A. 1980. A closed-form equation for predicting the hydraulic conductivity of unsaturated soils. *Soil Sci. Soc. Am. J*. **44**: 892-898.

van Kruysdijk, C.P.J.W. and Dullaert, G.M. 1989. A Boundary Element Solution of the Transient Pressure Response of Multiple Fractured Horizontal Wells. Paper presented at the 2nd European Conference on the Mathematics of Oil Recovery, Cambridge, England.

Veldsink, J.W., van Damme, R.M.J., Versteeg, G.F., and van Swaaij, W.P.M. 1995. The use of the dusty-gas model for the description of mass transport with chemical reaction in porous media. *Chem. Eng. J.* **57**: 115-125.

Voronoi, Georgy (1908). "Nouvelles applications des paramètres continus à la théorie des formes quadratiques". *Journal für die Reine und Angewandte Mathematik* **133**: 97–178. DOI:10.1515/crll.1908.133.97

Warren, J.E. and Root, P.J. 1963. The Behavior of Naturally Fractured Reservoirs. SPEJ. 228 245-55.

Watanabe, S., Sugiyama, H., and Miyahara, M. 2008. Molecular simulation of condensation process of Lennard-Jones fluids confined in nanospace with jungle-gym structure. *Adsorption*. **14**: 165-170. Doi: 10.1007/s10450-007-9087-4.

Webb, S.W. and Pruess, K. 2003. The Use of Fick's Law for Modeling Trace Gas Diffusion in Porous Media. *Transport in Porous Media.* **51**: 327-341.

Xiao, J. and Wei, J. 1990. Diffusion Mechanisms of Hydrocarbons in Zeolites - I. Theory. *Chem. Eng. Sci.* **47** (5): 1123-1141.

Zahid, S., Bhatti, A.A., Khan, H.A., and Ahmad, U. 2007. Development of Unconventional Gas Resources: Stimulation Perspective. Paper SPE 107053 presented at the Production and Operations Symposium, Oklahoma City, Oklahoma. 31 March-3 April.

APPENDIX

A. Appendix A - Summary of Validation for TOUGH+H2OGas against Multiple Analytical Solutions

A.1 Introduction

The TOUGH+H2OGas code was compared against the following analytical solutions: the pseudosteady-state radial flow of a slightly compressible liquid (Blasingame 1993; Dietz 1965); the transient radial flow of a gas using pseudopressure (Fraim and Wattenbarger 1987); the Warren and Root solution for dual-porosity flow in a fractured reservoir using the MINC mesh scheme (Warren and Root 1988; Pruess and Narasimhan 1982); the Wu analytical solution for Klinkenberg flow (Wu et al. 1988); and the Cinco-Meng solution for vertical-fractured flow (Cinco-Ley and Meng 1988).

A.2 Pseudosteady-State Conditions, Liquid Flow:

For the liquid (water) case under pseudosteady-state flow conditions, pressure as a function of radius and time is computed directly by

$$p_r = p_i - \frac{qB\mu}{2\pi kh}\left(\ln\left(\frac{r_e}{r}\right)+\left(\frac{1}{2}\right)\frac{\left(r^2-r_w^2\right)}{\left(r_e^2-r_w^2\right)}+0.75\right)-\frac{qBt}{V_p c_t} \quad \text{.....(A.1)}$$

as described by Blasingame (1993). We compare the solution of this equation against results from the TOUGH simulator using the input parameters given in Table A.1. Figure A.1 shows a comparison of the model results.

Table A.1 – Pseudosteady-state water flow model input parameters.

p_i	q	B	μ	k	h	r_e	r_w	c_t	ϕ	V_p
Pa	m^3/s		Pa-s	m^2	m	m	m	1/Pa		m^3
$1.00x10^7$	$1.00\ x10^{-3}$	1	$7.99\ x10^{-4}$	$3.00\ x10^{-14}$	10	100	0.059	$4.88\ x10^{-10}$	0.3	94247.78

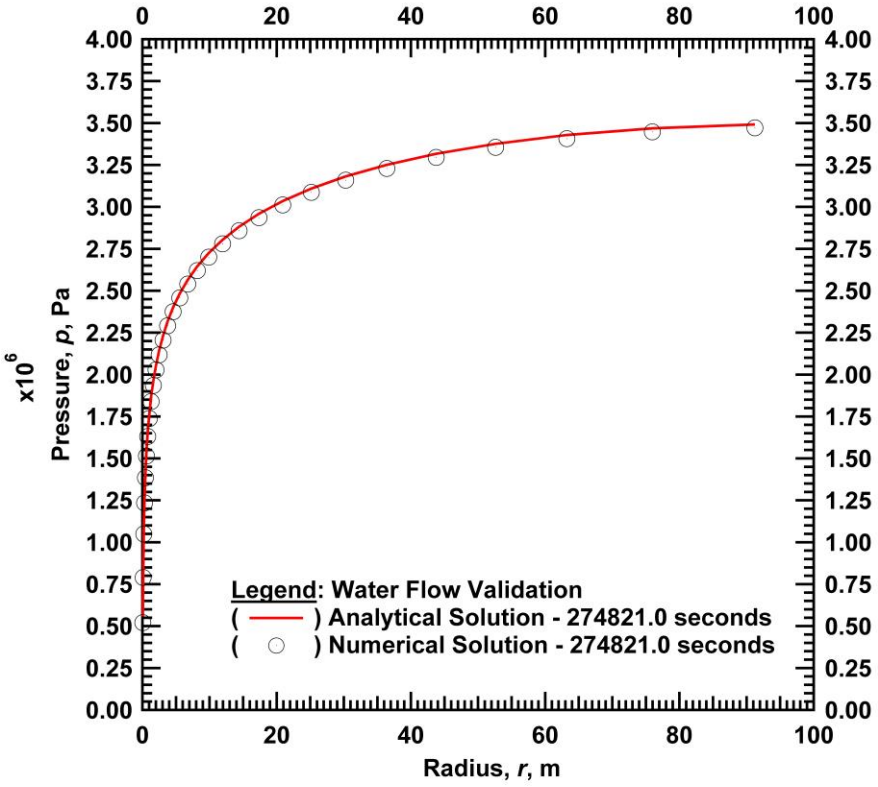

Figure A.1 – Pseudosteady-state water flow validation. Pressure versus radial distance at t = 274821 seconds using parameters described in Table A.1.

A.3 Transient Conditions, Gas Flow:

The gas case is solved in terms of pseudopressure and then the result is inverted for pressure. Dimensionless pressure under transient conditions is solved by the following equation, where E_1 represents the exponential integral:

$$p_d = \frac{1}{2} E_1\left(\frac{r_d^2}{4t_d}\right) \quad \text{.....(A.2)}$$

Pseudopressure is computed via:

$$p_p = \frac{\mu z}{p_b} \int_{p_b}^{p_r} \frac{p}{\mu z} dp \quad \text{.....(A.3)}$$

which assumes μ and z are constant, which is a reasonable assumption for the pressure range we are studying. The nondimensionalized equations for radius, pressure and time are:

$$r_D = \frac{r}{r_w} \quad \text{(A.4)}$$

$$p_D = p_{dc} \frac{kh}{qB\mu}(p_i - p_r) \quad \text{(A.5)}$$

$$t_D = t_{dc} \frac{k}{\phi\mu c_t r_w^2} t \quad \text{(A.6)}$$

Note that the rate must be expressed in m^3/s, not kg/s, in the analytical solution. We compare the solution of this equation against results from the TOUGH simulator using the input parameters given in Table A.2. Figure A.2 shows a comparison of the model results.

Table A.2 – Transient gas flow model input parameters.

Parameter	Unit	Value
p_i	Pa	1.00 x10^7
q	kg/s	1
q	m^3/s	1.54 x10^{-2}
B		1
μ	Pa-s	1.44 x10^{-5}
k	m^2	3.00 x10^{-14}
h	m	10
ϕ		0.3
r_w	m	0.059
r_e	m	100
c_t	1/Pa	1.07 x10^{-7}
p_{dc}		2π
t_{dc}		1

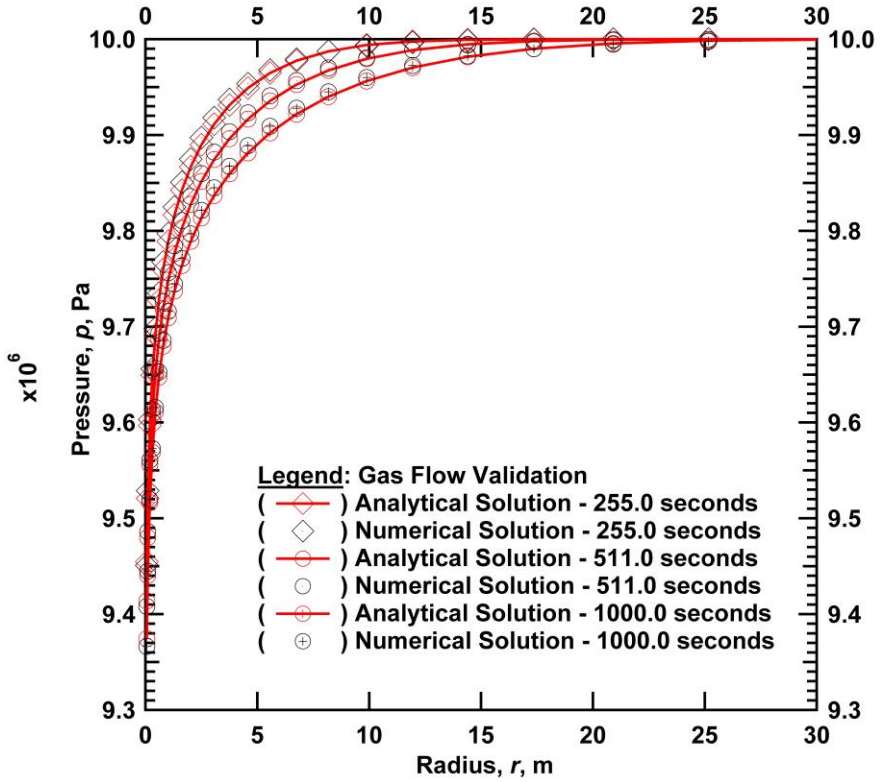

Figure A.2 – Transient gas flow validation. Pressure versus radial distance at several times (t = 255 s, 511 s, and 1000 s) using parameters from Table A.2.

A.4 Warren and Root Solution for Dual Porosity Flow

Warren and Root's line source solution for dual porosity flow:

$$p_D\left(t_D, r_D, \omega, \lambda, s\right) = \frac{1}{2}\ln\left[\frac{4}{e^{\gamma}}\frac{t_D}{r_D^2}\right] - \frac{1}{2}E_1\left(\frac{\lambda}{\omega(1-\omega)}t_D\right) + \frac{1}{2}E_1\left(\frac{\lambda}{1-\omega}t_D\right) + s \quad \text{.....(A.7)}$$

where λ, the interporosity flow parameter, is

$$\lambda = \alpha r_w^2 \frac{k_m}{k_f} \quad \text{.....(A.8)}$$

where α is the matrix block shape parameter, determined by

$$\alpha = \frac{4n(n+2)}{l^2} \quad \text{.....(A.9)}$$

where n is the number of normal sets of fractures (1,2 or 3) and l the fracture spacing.

We define a void fraction, V_f, corresponding to the fraction of the reservoir occupied by the fractures. Generally the porosity of the fractures, ϕ_f, is assumed to equal 1, meaning that the fractures are open and do not contain any internal grain structure. The total volume fraction occupied by the fractures as a fraction of bulk volume is thus

$$f_f = \phi_f V_f \quad \text{(A.10)}$$

ω, the storativity ratio, is

$$\omega = \frac{\phi_f V_f c_f}{\left[\phi_f V_f c_f + \phi_m V_m c_m\right]} \quad \text{(A.11)}$$

For the Warren and Root solution, different definitions are required for the dimensionless variables:

$$r_D = \frac{r}{r_w} \quad \text{(A.12)}$$

$$p_D = p_{dc} \frac{k_f h}{qB\mu}\left(p_i - p_r\right) \quad \text{(A.13)}$$

$$t_D = t_{dc} \frac{k_f}{\mu\left(\phi_f V_f c_f + \phi_m V_m c_m\right) r_w^2} t \quad \text{(A.14)}$$

A few extra parameters are defined for convenience, as the process of creating a MINC-based TOUGH mesh which reflects a given set of Warren and Root parameters involves some manipulation. We define an equivalent continuum fracture porosity (Pruess and Narasimhan 1982),

$$\phi_{f,cont} = \frac{3\delta}{l} \quad \text{(A.15)}$$

In our case it is more convenient to specify the fracture continuum porosity and establish the fracture aperture via

$$\delta = \frac{l\phi_{f,cont}}{3} \quad \text{(A.16)}$$

We assume the relation

$$k_{f,absolute} = \frac{\delta^3}{12} \quad \text{(A.17)}$$

can be used to estimate absolute fracture permeability, where δ is the fracture aperture. We deduce an adjusted fracture continuum permeability by

$$k_{f,cont} = \frac{2k_{f,abs}\delta}{l} \quad \text{(A.18)}$$

Table A.4 specifies the parameters which are used in the TOUGH MINC mesh generation and Table A.5 specifies which parameters are used in the corresponding Warren and Root analytical solution. We compare the solution of this equation against results from the TOUGH simulator using the input

parameters given in Table A.3, and derived Warren and Root parameters given in Table A.6. Figure A.3 and Figure A.4 show a comparison of the model results.

Table A.3 – Warren and Root dual porosity model input parameters, all cases.

p_i	T	q	B	μ	h	$k_{f,absolute}$	r_w	c_m	c_f
Pa	°C	m^3/s		Pa-s	m	m^2	m	1/Pa	1/Pa
6.08×10^{6}	90	2.5×10^{-5}	1	3.17×10^{-4}	10.0	9.26×10^{-11}	0.059	1.30×10^{-9}	1.00×10^{-7}

Table A.4 –TOUGH input parameters relating to permeability and porosity

			TOUGH	
Case	ϕ_m	ϕ_f	k_m	k_f
			m^2	m^2
1	5.00×10^{-2}	1.0	1.00×10^{-17}	6.17×10^{-15}
2	5.00×10^{-2}	1.0	1.00×10^{-17}	6.17×10^{-16}

Table A.5 – Warren and Root input parameters relating to permeability and porosity.

			Warren & Root	
Case	ϕ_m	ϕ_f	k_m	k_f
			m^2	m^2
1	5.00×10^{-2}	1.00×10^{-4}	1.00×10^{-17}	6.17×10^{-15}
2	5.00×10^{-2}	1.00×10^{-5}	1.00×10^{-17}	6.17×10^{-16}

Table A.6 – Warren and Root parameters, derived variables.

			Warren & Root Parameters				
Case	l_{const}	n	f	δ	α	ω	λ
	m			m	m^{-2}		
1	1	3	0.0001	3.33×10^{-5}	60	1.3334×10^{-1}	3.38353×10^{-4}
2	10	3	0.00001	3.33×10^{-5}	0.6	1.5152×10^{-2}	3.38353×10^{-5}

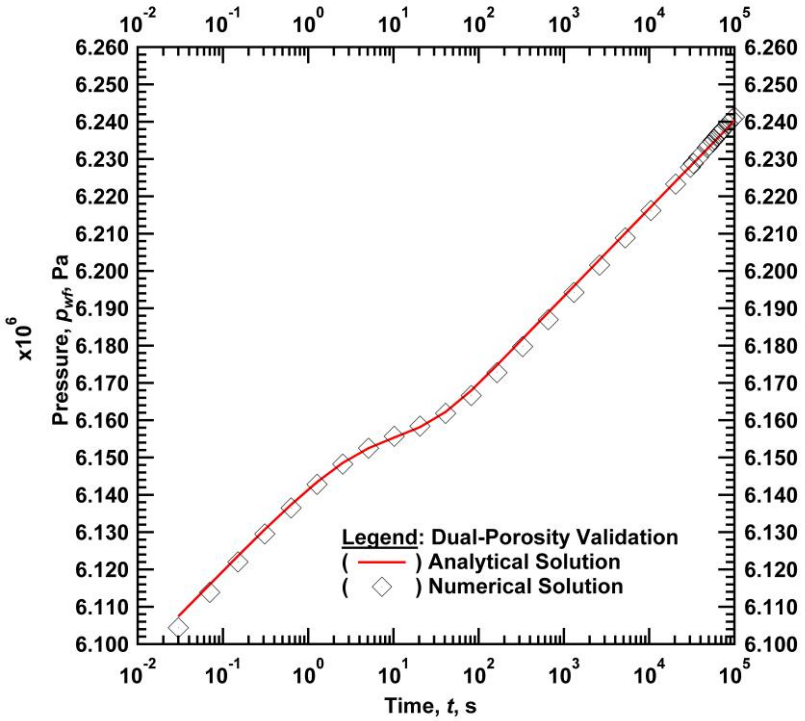

Figure A.3 – Warren and Root dual porosity flow validation, reflecting Case 1 properties. Pressure over atime at $r = r_w$.

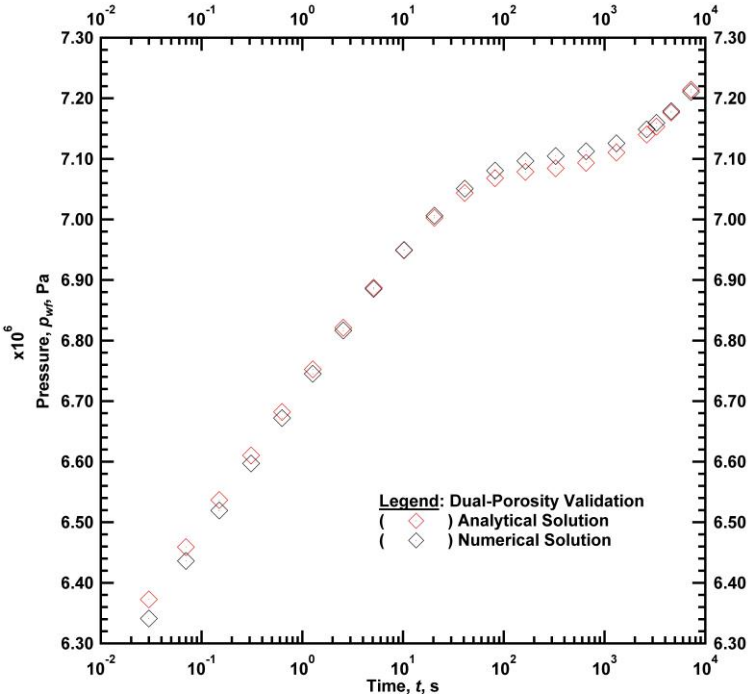

Figure A.4 – Warren and Root dual porosity flow validation, reflecting Case 2 properties. Pressure over time at $r = r_w$.

A.5 Klinkenberg flow

Klinkenberg (1941) flow assumes a pressure-dependent permeability, :

$$k_g = k_\infty \left(1 + \frac{b}{p}\right) \quad \text{(A.19)}$$

Jones (1972) found the b generally decreases with increasing permeability by approximately:

$$b \propto k_\infty^{-0.36} \quad \text{(A.20)}$$

Wu et al. (1988) derive their flow equations in terms of a pressure function, :

$$p_k = p + b \quad \text{(A.21)}$$

Among the solutions presented by Wu et al. (1988) is the line source solution for an infinite radial system at a constant rate:

$$p_k^2(r,t) = p_{ki}^2 - \frac{\mu q}{2\pi k_\infty h c_t} \mathrm{Ei}\left(-\frac{k_\infty p_k r^2}{4\phi\mu t}\right) \quad \text{(A.22)}$$

We find this is similar in form to the general solution for transient gas flow, although Wu et al. (1988) appear to have used the so-called "pressure-squared" approach. We compare the solution of this equation against results from the TOUGH simulator using the input parameters given in Table A.7. Figure A.5 shows a comparison of the model results.

Table A.7 – Klinkenberg flow model input parameters.

k_∞	b	p_i	μ	ϕ	H	q	c_t	z
m^2	1/Pa	Pa	Pa-s		m	m^3/s	1/Pa	
3.00×10^{-14}	73830.6	1.00×10^{-7}	1.44×10^{-5}	0.3	10.0	1.54×10^{-2}	1.07×10^{-7}	0.89

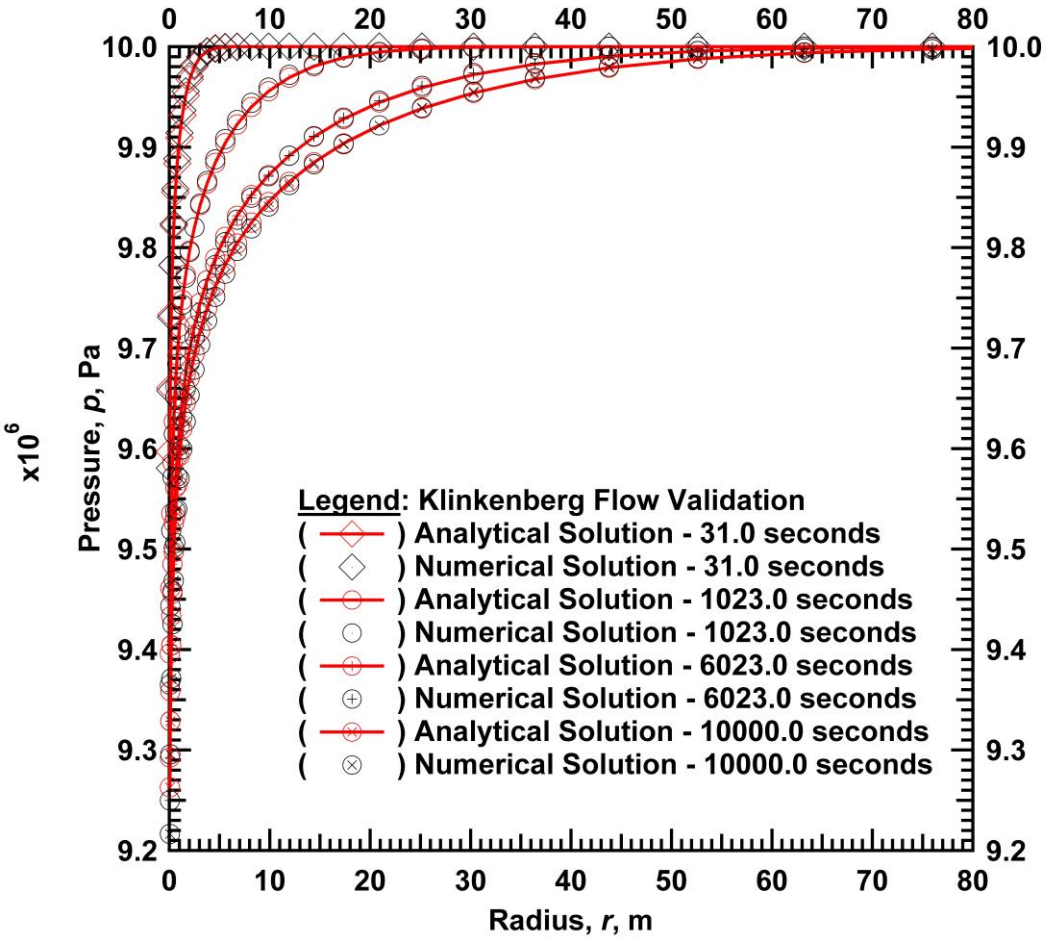

Figure A.5 – Klinkenberg flow validation. Pressure versus radial distance at several times (t = 31 s, 1023 s, 6023 s, and 10000 s).

A.6 Cinco-Meng Solution for Vertical-Fractured Flow

The Cinco-Meng (1988) solution models flow from a reservoir into a finite-conductivity vertical fracture. The dimensionless variables employed by the Cinco-Meng solution are

$$x_D = \frac{x}{x_f} \quad \text{(A.23)}$$

$$p_D = \frac{k_m h}{\alpha q B \mu}\left(p_i - p\right) \quad \text{(A.24)}$$

$$t_D = \frac{\beta k_m}{\phi_w \mu c_T x_f^2} t \quad \text{(A.25)}$$

where α = 1842 for liquids ("oil") and β = 3.6e-9 are dimensionless unit conversion constant in the units described blow.

For a fracture,

$$F_{CD} = \frac{k_f b_f}{k_m x_f} \quad \text{.....(A.26)}$$

The Cinco-Meng solution is expressed as

$$\bar{p}_{wD}(z) - \frac{1}{2}\sum_{i=1}^{n}\left\{\bar{q}_{fDi}(z)\int_{x_{Di}}^{x_{Di+1}}\left[K_0\left(x_{Dj}-x'\right)\sqrt{z}+K_0\left(x_{Dj}+x'\right)\sqrt{z}\right]\right\}+\ldots$$

$$\ldots+\frac{\pi}{\left(k_f b_f\right)_D}\left\{\sum_{i=1}^{j-1}\left[\left(\frac{(\Delta x)^2}{2}+\Delta x\left(x_{Dj}-i\Delta x\right)\right)\bar{q}_{fDj}(z)\right]+\frac{(\Delta x)^2}{8}\bar{q}_{fDj}(z)\right\}=\frac{\pi x_{Dj}}{\left(k_f b_f\right)_D z} \quad \text{.....(A.27)}$$

with the "flux condition"

$$\Delta x\sum_{i=1}^{n}\bar{q}_{fDi}(z)=\frac{1}{z} \quad \text{.....(A.28)}$$

These two equations imply the following system of equations,

$$\left[A_{ij}\right]\begin{bmatrix}\bar{q}_{fDj}(z)\\ \bar{p}_{wD}(z)\end{bmatrix}=\left[B_j\right] \quad \text{.....(A.29)}$$

The Cinco-Meng solution is then solved at a given fracture conductivity.

Water compressibility is estimated using the Osif (1984) model, where

$$c_w = 1/7.022p + 541.5c_s - 537T + 403300 \quad \text{.....(A.30)}$$

With p in psi, c_w in 1/psi, c_s in g NaCl/L, and T in F. We compare the solution of this equation against results from the TOUGH simulator using the input parameters given in Table A.8. Figure A.6 and Figure A.7 show a comparison of the model results.

Table A.8 – Cinco-Meng vertical fractured flow model input parameters.

Parameter	Unit	Case 1	Case 2
p_i	kPa	1.0×10^{5}	1.0×10^{5}
k_m	μm^2	3.3×10^{-3}	3.3×10^{-4}
k_f	μm^2	3.0×10^{3}	3.0×10^{3}
h	m	10	10
q	m^3/d	172.8	172.8
B		1	1
μ	Pa-s	4.91×10^{-4}	4.91×10^{-4}
ϕ_m		0.3	0.3
c_t	1/Pa	3.37×10^{-10}	3.37×10^{-10}
x_f	m	20	20
F_{cD}		1000	10000
b_f	m	0.022	0.022

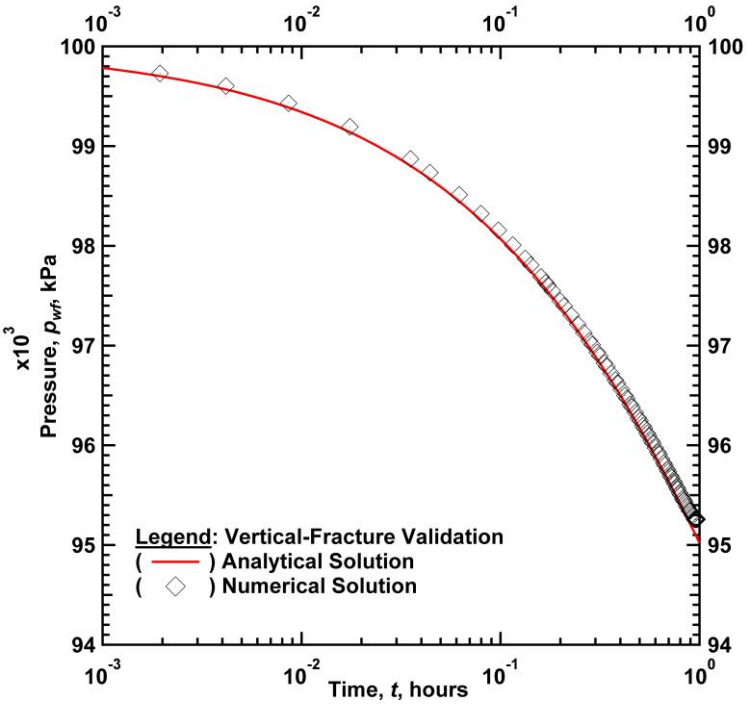

Figure A.6 – Cinco-Meng solution for vertical-fractured flow validation for Case 1 properties, F_{CD} = 1000.

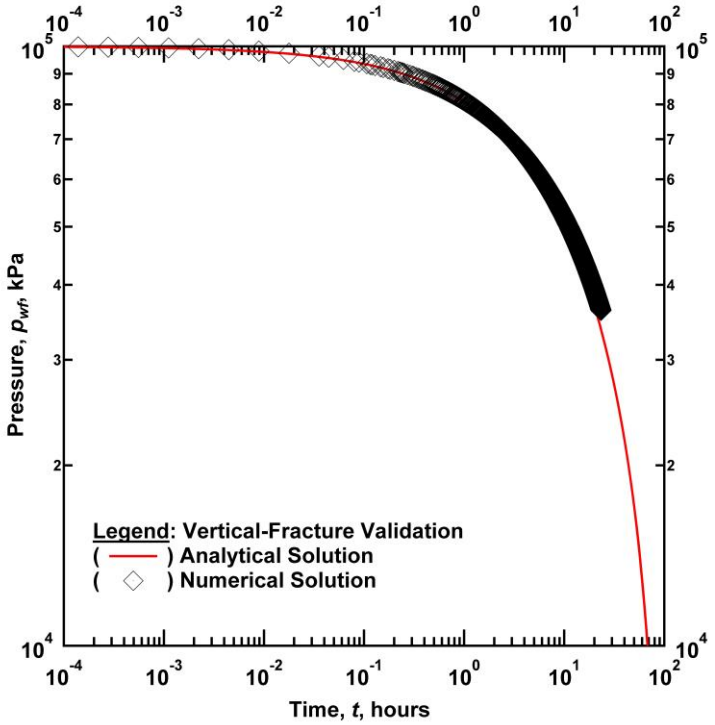

Figure A.7 – Cinco-Meng solution for vertical-fractured flow validation for Case 2 properties, F_{CD} = 10000.

Nomenclature

- b - Klinkenberg parameter, Pa
- B - formation volume factor, surface volume/reservoir volume
- b_f - fracture width, m
- c_t - total compressibility, 1/Pa
- c_w - water compressibility, 1/Pa
- E_1 - the Exponential Integral function
- E_i - the Exponential Integral function
- F_{CD} - fracture conductivity, dimensionless
- f_f - fracture void fraction, dimensionless
- h - reservoir thickness, m
- k - permeability, m^2 (μm^2 for Cinco-Meng solution)
- K_0 - Bessel function
- k_g - Klinkenberg-adjusted permeability, m^2
- k_∞ - absolute matrix permeability, m^2
- k_f - fracture permeability, m^2
- l - fracture spacing, m

n - number of normal sets of fractures, dimensionless

p - pressure, Pa

p_b - base pressure reference point for pseudopressure computation, Pa

p_D - dimensionless pressure

p_{dc} - conversion factor, 2π for SI units

p_i - initial pressure, Pa

p_k - Klinkenberg-adjusted pressure, Pa

p_r - pressure at radius r, Pa

q - rate, m^3/s (m^3/day for Cinco-Meng solution)

r - radius, m

r_D - dimensionless radius

r_e - outer boundary radius, m

r_w - wellbore radius, m

t - time, s (hours for Cinco-Meng solution)

t_D - dimensionless time

t_{dc} - conversion factor, 1.0 for SI units

V_p - pore volume, m^3

x_f - fracture half-length, m

z - gas compressibility factor, dimensionless

Greek Symbols

α - block shape factor, $1/m^2$; elsewhere, constant employed in Cinco-Meng solution, dimensionless

β - constant employed in Cinco-Meng solution, dimensionless

δ - fracture aperture, m

λ - Warren and Root interporosity flow parameter, dimensionless

μ - viscosity, Pa-s

ϕ - porosity, dimensionless

ω - Warren and Root storativity ratio, dimensionless

Subscript

abs - implies that the property reflects an absolute media value

cont - implies that the property reflects an equivalent continuum-adjusted value

f - fracture

m - matrix

References:

Cinco-Ley, H. and Meng, H.-Z. 1988. Pressure Transient Analysis of Wells With Finite Conductivity Vertical Fractures in Double Porosity Reservoirs. Paper SPE 18172-MS presented at the SPE Annual Technical Conference and Exhibition, Houston, Texas, 2-5 October 1988. http://dx.doi.org/10.2118/18172-MS.

Dietz, D.N. 1965. Determination of Average Reservoir Pressure From Build-Up Surveys. *JPT*, 955-959.

Blasingame, T.A. 1993. Semi-Analytical Solutions for a Bounded Circular Reservoir – No Flow and Constant Pressure Outer Boundary Conditions: Unfractured Well Case. Paper SPE 25479 presented at the SPE Production Operations Symposium held in Oklahoma City, Oklahoma, 21-23 March.

Fraim, M.L. and Wattenbarger, R.A. 1987. Gas Reservoir Decline Curve Analysis Using Type Curves with Real Gas Pseudopressure and Pseudotime. *SPEFE* 671-682.

Jones, S. C. 1972. A rapid accurate unsteady-state Klinkenberg parameter, *SPEJ* 383-397.

Klinkenberg, L.J. 1941. The permeability of porous media to liquids and gases. Drilling and Production Practice, American Petroleum Inst., pp. 200-213.

Osif, T.L.: "The Effects of Salt, Gas, Temperature, and Pressure on the Compressibility of Water," paper SPE 13174 presented at the 1984 SPE Annual Technical Conference and Exhibition, Houston, Sept. 16-19.

Pruess, K. and Karasaki, K., 1982. A Practical Method for Modeling Fluid and Heat Flow in Fractured Porous Media. Paper SPE 10509, presented at the Sixth SPE Symposium on Reservoir Simulation, New Orleans, LA, Feb. 1-3.

Warren, J.E. and Root, P.J.: "The Behavior of Naturally Fractured Reservoirs," *SPEJ* (Sept. 1963) 245-55; *Trans*. AIME, **228**.

Wu, Y., Pruess, K., Persof, P. 1988. Gas Flow in Porous Media with Klinkenberg Effects. Transport in Porous Media. 32: 117-137.